
Investigation of the fast-ion confinement in Wendelstein 7-X based on FIDA spectroscopy

Péter Zs. Pölöskei



München 2022

Investigation of the fast-ion confinement in Wendelstein 7-X based on FIDA spectroscopy

Péter Zs. Pölöskei

Dissertation
an der Fakultät für Physik
der Ludwig–Maximilians–Universität
München

vorgelegt von
Péter Zs. Pölöskei
aus Budapest, Hungary

München, den 04.02.2022

Erstgutachter: Prof. Dr. Hartmut Zohm
Zweitgutachter: Prof. Dr. Benedikt Geiger
Tag der mündlichen Prüfung: 13.04.2022

Abstract

Excellent confinement of fast alpha particles is one of the fundamental requirements for the successful operation of future fusion power plants since these particles heat the background plasma by collisions and, if lost, might damage the reactor walls. Wendelstein 7-X (W7-X) is an optimised stellarator experiment, which confines high-temperature plasmas by 3D magnetic fields. Here, we present the first results of dedicated fast-ion transport studies at the W7-X experiment, which was recently equipped with two neutral beam injectors (NBI) to generate fast ions.

In order to gain insight into the distribution of fast-ions, a multi-view spectroscopy system was utilized, which enables observation of Doppler-shifted line radiation of fast ions, neutralized along their path by charge-exchange reactions. To interpret the observed emission, also called FIDA radiation, the FIDASIM synthetic spectra predicting code was used. The code was adapted to the stellarator geometry of W7-X, incorporating its NBI injection and observation line of sight geometry. For the validation of the extended code, the measured absolute calibrated spectra, which include direct radiation from the active neutral source (beam- and halo emission) in addition to the FIDA emission, was compared to FIDASIM predictions, showing less than 25% deviations from the measured intensity. Then for the FIDA emission prediction, the fast-ion distribution function from the ASCOT simulation code was employed. Comparison of resulting synthetic FIDA spectra with measurements from the plasma center shows good agreement for fast ions propagating against the injection direction. However, a growing discrepancy in both intensity and spectral shape is observed towards the plasma edge. This discrepancy could be attributed to passive FIDA radiation caused by the charge exchange reaction between fast ions and cold neutrals. Using realistic background neutral density profiles and additionally modelling of a 3D localised distribution function of fast ions, deposited in the edge region, it became possible to explain the measured spectral shape and intensity.

By selecting lines of sight that avoid complications caused by the complex 3D edge localised fast ion cloud, it was possible to show that ASCOT predictions are valid within a factor of four, considering upper and lower boundaries of the background neutral density.

This shows that the FIDA spectroscopy method can be successfully applied to W7-X and that the specific choice of lines of sight allows quantitative studies of fast particle confinement in future experimental campaigns.

Zusammenfassung

Eine der Grundvoraussetzungen für den erfolgreichen Betrieb zukünftiger Fusionskraftwerke ist der hervorragende Einschluss von schnelle Alphateilchen, da diese das Hintergrund Plasma durch Kollisionen heizen und bei Verlust die Reaktorwände beschädigen können. Die Untersuchung des schnelle Teilchen Einschlusses ist daher ein Hauptziel des Wendelstein 7-X (W7-X) Stellarator Experiments, welches Hoch-Temperatur Plasmen durch 3D Magnetfelder einschließt. Daher wurde W7-X kürzlich mit zwei Neutralstrahl-Injektoren ausgestattet, welche eine Population von schnellen Ionen mit einer kinetischen Energie von maximal 60 keV erzeugen.

Um einen Einblick in die Verteilungs-Funktion dieser Ionen zu erhalten, wurde ein Mehrfachspektroskopie System verwendet, welches erlaubt Doppler-Verschobene Linien - Strahlung von schnellen Ionen zu beobachten, welche entlang des Neutral Strahls durch Ladungsaustausch Reaktionen neutralisiert werden. Zur Interpretation dieser auch FIDA-Strahlung genannten Emission, wurde der sog. FIDASIM code verwendet welcher synthetische FIDA Spektren erzeugt. Der Code wurde an die Stellarator Geometrie von W7-X angepasst, wobei unter anderem die Neutral-Injektion und die Sichtlinien Geometrie berücksichtigt wurden. Da die gemessenen, absolut kalibrierten Spektren zusätzlich zur FIDA Emission auch direkte Strahlung des Neutral Strahls enthalten (Beam-Emission and Halo), konnte der FIDASIM Code mit Abweichungen von weniger als 25% validiert werden. Für die Vorhersage der FIDA-Emission wurden theoretische Verteilungsfunktionen von schnellen Ionen verwendet. Der Vergleich von resultierenden synthetischen Spektren mit den Messungen aus dem Plasma Zentrum zeigt gute Übereinstimmung für schnellen Ionen die sich entgegen der Injektions Richtung ausbreiten. Jedoch wird zum Plasma Rand hin eine wachsende Diskrepanz sowohl in Intensität als auch in spektraler Form beobachtet. Diese Diskrepanz kann auf passive FIDA-Strahlung zurückgeführt werden, welche durch Ladungs Austauschreaktionen zwischen schnellen Ionen und Hintergrund-Neutralteilchen verursacht wird. Mit Hilfe eines realistischen Hintergrund-Neutralteilchen Dichteprofiles und der Berücksichtigung von im Randbereich deponierten schnellen Ionen, konnte die gemessene Spektrale Form und Intensität erklärt werden.

Somit konnten Sichtlinien ausgewählt werden, welche nicht durch die komplexe, 3D-lokalisierte Verteilung von Rand-deponierten schnellen Ionen beeinträchtigt werden. Es konnte daher gezeigt werden, dass die theoretisch vorhergesagten schnelle Teilchen Verteilungsfunktionen innerhalb eines Faktors von vier gültig sind.

Dies zeigt dass die FIDA Spektroskopie Methode an W7-X erfolgreich angewendet wer-

den kann und dass die gezielte Wahl von Sichtlinien quantitative Studien des schnelle Teilchen Einschlusses in zukünftigen Experimentier Kampagnen ermöglicht.

Contents

1	Introduction	1
1.1	Fusion for a clean energy source	1
1.2	Magnetic plasma confinement	3
1.3	Stellarators	5
1.4	Basics of FIDA measurements	6
1.5	Thesis outline	7
2	Theoretical background	9
2.1	Stellarator optimization	9
2.1.1	Classes of collisionless particles orbits	11
2.1.2	Plasma β effects on collisionless particles	13
2.2	Sources of fast-ions	15
2.2.1	Fast-ion slowing down	16
2.2.2	Fast-ion slowing down simulations with ASCOT	18
2.3	Recycling neutrals	20
2.3.1	KN1D	20
3	The Wendelstein 7-X stellarator	23
3.1	Parameters and design criteria	23
3.2	VMEC equilibrium calculations	24
3.3	Heating systems	27
3.3.1	Electron cyclotron resonance heating	27
3.3.2	Neutral beam injection	28
3.4	Main core diagnostics	29
3.4.1	Thomson scattering	29
3.4.2	Dispersion interferometry	32
3.5	Active neutral beam spectroscopy	33
3.5.1	ILS-Green – Carbon-impurity spectroscopy	35
3.5.2	ILS-Red – Balmer-alpha spectroscopy	36
3.5.3	Calibration of the ILS-Red spectrometer	38

4	FIDASIM modelling for W7-X	47
4.1	Collisional radiative model	47
4.2	Spectral predictions	49
4.3	Simulation grid	50
4.4	Neutral density- and spectral predictions	51
4.4.1	Neutral beam injection parameters	51
4.4.2	Beam- attenuation and emission	55
4.4.3	Halo- neutrals and emission	55
4.4.4	FIDA emission predictions	56
4.5	FIDA weight function calculations	59
5	Validation of active beam-, halo- and FIDA emission modeling	63
5.1	Prediction of active neutral populations	63
5.1.1	Beam modelling validation	64
5.1.2	Halo modeling validation	67
5.1.3	FIDA emission modeling	69
6	Investigation of passive FIDA emission	73
6.1	Modeling of the passive emission with confined fast-ions	73
6.1.1	Cold neutrals simulation with KN1D	74
6.1.2	Passive FIDA emission prediction using ASCOT4	75
6.1.3	Extended VMEC boundaries	77
6.1.4	Prompt-fast-ion passive FIDA prediction	82
6.2	Characterisation of the passive emission with weight functions	85
7	Boundaries of the fast-ion confinement in W7-X	89
7.1	Boundaries of the neutral density	89
7.2	Estimation of fast-ion density	91
8	Summary and Outlook	95
8.1	Summary	95
8.2	Outlook	97
	Acknowledgement	108

Chapter 1

Introduction

1.1 Fusion for a clean energy source

Present day's society is reliant on the availability of electricity. As the demand increases year to year, it is important to provide sustainable energy sources that can replace fossil fuels, which cover around 80% of Earth's current energy-mix [1]. Fossil fuels are contributing to the global greenhouse effect through CO₂ production, their availability is regional, making countries without it reliant upon others. On top of it their reserves are foreseen to be depleted in about 100 years [1].

A possible solution could be fusion energy production, an idea which has been around since the early 20th century [2]. The basic principle is to fuse light and abundant hydrogen isotopes together to form more tightly bound helium nuclei. The fusion reaction with the largest cross-section is the fusion of deuterium ($D \equiv {}^2_1\text{H}$) and tritium ($T \equiv {}^3_1\text{H}$):



Here, a single reaction produces an energy of 17.6 MeV which is significantly larger than the energy released when burning fossil fuels, around $\mathcal{O}(10)$ eV per reaction. The D-T reaction generates two particles. First, an energetic neutron (14.1 MeV) is produced, which could be slowed down in solid materials, would be used to generate heat and subsequently electricity. Second, a charged, energetic (3.5 MeV) α particle ($\alpha \equiv {}^4_2\text{He}$) is born, which would slow down via Coulomb-collision with other reactants and could therefore heat-up the fuel, counterbalancing possible power losses.

For fusion reactions to happen, the Coulomb-repulsion of the charged particles needs to be overcome which requires large collision energies. Figure 1.1 shows the cross-section for different fusion reactions as a function of the collision energy. As it can be seen, collision energies in the order of $\mathcal{O}(10)$ keV are needed. Efficient fusion energy production would

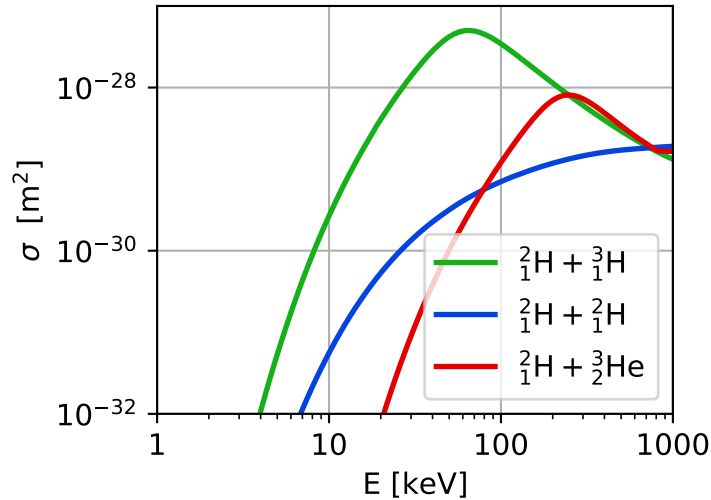


Figure 1.1: Cross-section for different fusion reactions as function of the collision energy in the center of mass reference system, marked with different colors. Deuterium, and tritium fusion happens at the lowest energies with the highest probability [3, 4].

be possible in a media, where the Coulomb-scattering does not lead to net energy losses, but just redistributes the macroscopic energy of the system. Such system could be a media in thermodynamic equilibrium with high temperatures ($\mathcal{O}(10)$ keV¹) and preferably high densities in order to provide as much fusion reactions as possible. At such high temperatures the media exists in a plasma state, a highly ionized gas [5] where an ensemble of electrons and ions can coexist. By additionally considering the energy confinement time of this media, the triple product [6, 3] of density (n), temperature (T) and energy confinement time (τ_E) was introduced, providing a practical lower boundary for self sustained fusion in a reactor:

$$nT\tau_E \geq 3 \cdot 10^{21} \text{keVs/m}^3. \quad (1.2)$$

This formula is valid in the proximity of the optimal temperature of DT fusion of 15

¹In fusion plasma physics eV is conveniently used to describe temperatures despite it is being a unit of energy. $1 \text{ eV} \approx 11650 \text{ K}$, the ratio of elementary charge and Boltzmann constant.

keV and shows that one needs to either maximize the confinement time or the product of plasma density and temperature (plasma kinetic pressure). For example inertial confinement fusion research tries to reach very high kinetic pressures using lasers while having short confinement times [7]. Another possibility is magnetic confinement fusion which aims at moderate pressures with long energy confinement times of several seconds [3].

1.2 Magnetic plasma confinement

High temperature plasmas can be confined using strong magnetic fields, \vec{B} , that act on charged particles via the Lorentz-force:

$$\vec{F} = q \left(\vec{E} + \vec{v} \times \vec{B} \right), \quad (1.3)$$

Here, q is the charge of a particle, \vec{E} is an electric field, \vec{v} is the particle velocity, which is often decomposed into v_{\parallel} and v_{\perp} with respect to the local magnetic field. Due to the Lorentz force, particles are forced into helical orbits. This motion is composed of a quick gyration around a magnetic field line with a Larmor radius of $r_L = (mv_{\perp})/(q|B|)$ for a particle with a mass of m , a parallel translation along the field line and a slow cross-field drift. This implies that trajectories can be spatially well localised in the Larmor-radius magnitude. As particles are still free to move along field lines to avoid possible end-losses in an open configuration, a set of toroidally arranged magnetic field coils is typically used to bend the magnetic field into a self-closing toroid shape.

Here, it is convenient to introduce toroidal coordinates, as depicted in figure 1.2, which will be used later in this thesis. Two angular coordinates are used, which are the toroidal angle φ , and the poloidal angle θ . Moreover, the major radius R is used which is the distance from the center axis of the device, as well as the minor radius r , describing the distance from the centerpoint of the toroid to a given position at fixed toroidal angle.

In such magnetically confined plasma the force balance equation describes the equilibrium state, neglecting flows:

$$\vec{j} \times \vec{B} = \vec{\nabla} p \quad (1.4)$$

where \vec{j} is the plasma current, \vec{B} is the external magnetic field, and $\vec{\nabla} p$ is gradient of the plasma kinetic pressure. Following this and the Maxwell equations, one can derive that in the equilibrium state nested flux surfaces form, which are characterised as their normal

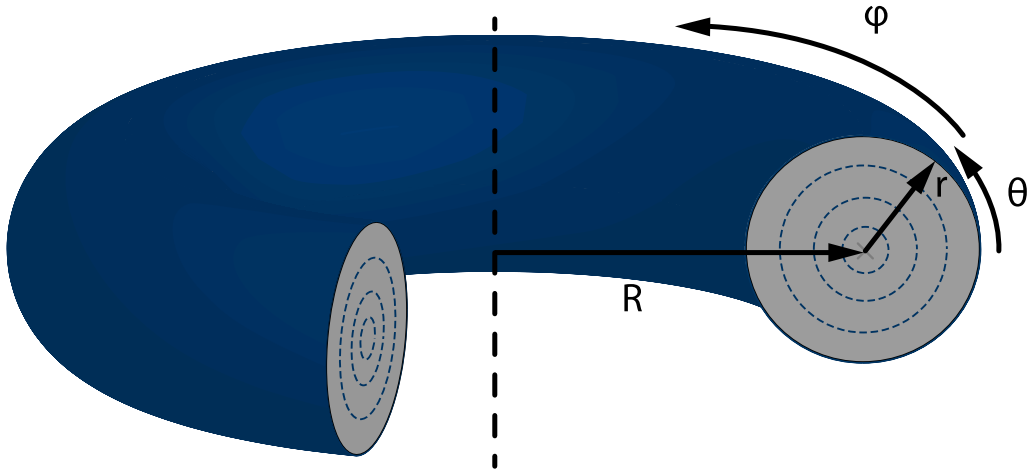


Figure 1.2: Schematics of coordinates used in a toroidal systems. Two angles, φ toroidal- and θ poloidal angle, \mathbf{r} minor radius and \mathbf{R} major radius.

vector is perpendicular to the magnetic field vector everywhere [8]. From equation 1.4 we can derive that the pressure is constant on flux surfaces as $\vec{B} \cdot \vec{\nabla} p = 0$, thus the pressure gradient is perpendicular to the magnetic field lines and the plasma currents \vec{j} [3]. In figure 1.2, flux surfaces (surfaces of constant magnetic flux) are indicated as dashed closed contours. As transport along field lines, at flux surfaces, is much faster than perpendicular to it, kinetic parameters like temperature and density equilibrate on these fast and are often expressed as the function of flux coordinates. Thus these profiles are often depicted as a function of the flux surface's position.

To provide coordinates of these surfaces that is also valid in non-circular plasmas (or 3D geometries), the normalized toroidal magnetic flux, s , is used:

$$s = \frac{\Phi}{\Phi_{max}} \quad (1.5)$$

where Φ is the toroidal flux:

$$\Phi = \iint_{S_t} \vec{B} \cdot \vec{n} dS \quad (1.6)$$

with \vec{n} is the normal vector of S_t surface, which contour is marked in figure 1.2 and Φ_{max} is the toroidal flux at the plasma boundary (the last closed flux surface). Note that the resulting s coordinate ranges from 0 in the core, to 1 in the edge. Another often used choice

of flux labeling is the effective minor radius, r_{eff} , which is proportional to the square root of s ($r_{eff} = a\sqrt{s}$), where a is the average minor radius of the last closed flux surface (often the ratio, r_{eff}/a is referred to as ρ).

Due to the curved magnetic field lines in such toroidal arrangement, the so-called curvature and gradient-B drifts arise which would lead to charge separation and, in turn, provoke a detrimental plasma displacement due to a radial drift caused by the corresponding electrical field [3]. Thus an additional poloidal magnetic field is required which helically twists the magnetic field lines and stops the above mentioned charge separation. The poloidal magnetic field can be generated for example by an internal plasma current, which is realized within the so-called tokamak concept. Alternatively and technologically more challenging, the twisted magnetic field can be produced by using 3D shaped coils, which is realized with the so-called stellarator concept.

1.3 Stellarators

Stellarators confine the plasma with the above mentioned helically twisted magnetic field produced by 3D shaped coils. A typical stellarator device is depicted in figure 1.3 with its 3D shaped complex coils, and the plasma volume within.

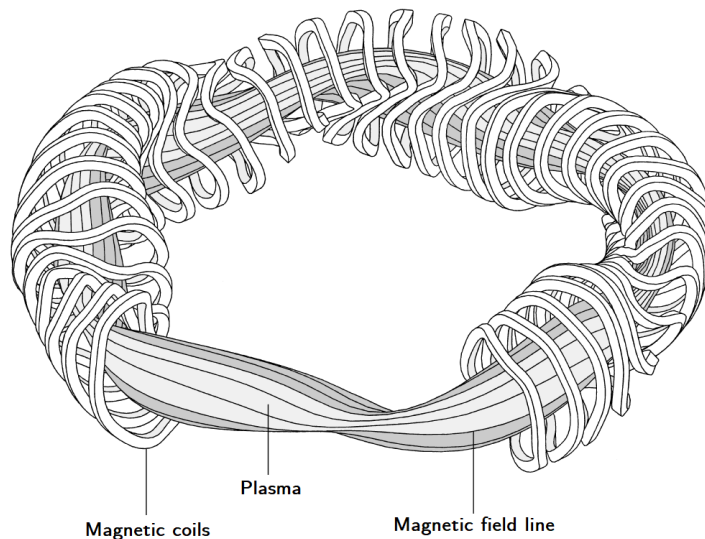


Figure 1.3: Sketch of a stellarator fusion device with 3D shaped magnetic coils, and the plasma volume in it. Picture taken from IPP photo gallery.

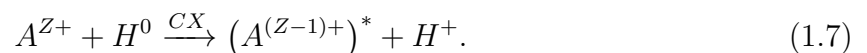
One of the challenges when designing the magnetic field structure of stellarators is to

provide good confinement of fast α particles in order to achieve efficient heating of the background plasma and safe operation of the device. Fast particles are almost collisionless as their relative velocities compared to the background electrons and ions are much larger, fusion born α particles have energies in the MeV range while the background plasma temperature is in the keV range. This means that their possible interaction time is short and, hence, the momentum exchange through the Coulomb collisions is generally small, they must be well confined if we want to have them slowed down in the plasma. Because of this, fast particles on orbits that exhibit strong radial drifts due to imperfections of the magnetic field structure will be easily lost if they are not displaced by collisions. They will eventually collide with plasma-facing components causing strong heat loads and might even damage the device's integrity. This is why excellent confinement of fast particles is indispensable for an operational fusion reactor.

Amongst the most important goals of the Wendelstein 7-X (W7-X) stellarator experiment [9], where this thesis was carried out, is the need to demonstrate good fast particle confinement as this was one of the criteria for optimizing the devices' magnetic field structure. The experiment has been equipped with a powerful neutral beam injection system, which generates fast-ions with energies of up to 60 keV. The choice of acceleration voltage is such, that the resulting minor radius normalized fast-ion Larmor-radius (r_L/a) is comparable to fusion reactor born α particles', thus their confinement is comparable and can be studied.

1.4 Basics of FIDA measurements

In order to study the behaviour and confinement of fast-ions at W7-X, a diagnostic method called charge exchange recombination spectroscopy (CXRS) was used. Charge-exchange recombination spectroscopy observes the light emitted following a charge exchange reaction (CX) of an ion species A and a donor neutral H^0 :



In the case of active spectroscopy, donor neutrals are injected using heating- or diagnostic neutral beams, as well as gas puffs [10, 11]. After the charge exchange reaction, species A is typically in a highly excited state [12] such that localized and characteristic line radiation

will be emitted following the spontaneous deexcitation of it. As the charge exchange process has little impact on the momentum of the reactants, the observed light will carry information on the local ion species' parameters.

Fast-ions in the plasma have thermalization times in the order of 50 ms in W7-X [13] and might undergo the above-described charge exchange reaction during this relatively long time. Thus they can play the role of the fully ionized reaction partner and we can observe their characteristic Balmer-alpha line emission, later referred to as Fast-Ion D-Alpha (FIDA)² [14, 15]. This radiation, which is observed with large Doppler-shift and broadening due to the higher energies of emitting particles, allows detailed studies of the fast-ion confinement as demonstrated in other fusion experiments [16, 17, 18, 19, 20].

1.5 Thesis outline

This thesis focuses on the study of the fast-ion confinement and the understanding of the Balmer-alpha spectrum in W7-X using FIDA spectroscopy. It presents the current understanding of the novel experimental measurements using detailed modelling of the spectra with FIDASIM. Several complicating effects and issues were identified and mitigated, leading to a thorough understanding of the observed Balmer-alpha spectrum and the first experimental estimate of the fast ion population inside W7-X plasmas.

Chapter 2 presents an introduction of the theoretical background relevant for this work, focusing on the properties of fast-ions and donor neutrals for CX reactions. Orbits of collisionless particles will be described and the general problem of trapped particle confinement in stellarators will be discussed. Furthermore, methods generating fast particles in fusion experiments, and their slowing down process due to collisions with the background plasma are presented. Moreover, the various sources of neutral particles in present-day experimental devices are described, and finally, chapter 2 provides an introduction to recycling cold neutrals as donors for charge-exchange reactions.

Chapter 3 gives a detailed description of the Wendelstein 7-X device and its diagnostic capabilities utilized in this work including the main diagnostic tool of this thesis, the active CXRS system.

²As W7-X did only operate with hydrogen so far, the D in the FIDA expression can be misleading as it refers to the deuterium plasmas, in which it was first observed. Due to this historic reason, we keep this notation.

Chapter 4 then introduces the Balmer-alpha spectra modelling tool FIDASIM, and its adaptation to stellarators, specifically to Wendelstein 7-X. Moreover, chapter 4 presents the investigation of the weight functions for the spectroscopy system, the capabilities of the available lines of sight for investigating the fast-ion phase space.

Chapter 5 shows the validation process of FIDASIM which comprises the intensity and wavelength calibration of measurements, binning of the measurements on the spectrometer and then directly comparing the measured Balmer-alpha spectra to the FIDASIM predicted active spectral features.

In chapter 6 the study of the edge localised passive FIDA emission is presented with the discussion of its current understanding, similarities and discrepancies in both the spectral shape and intensity.

Building on the previous observations of strong passive FIDA contribution in chapter 7 we utilize estimates of the background neutral density to derive boundaries of the fast-ion density of W7-X compared to theoretical expectations.

Finally, chapter 8 summarizes this work, presents possibilities of future improvements both in modelling and measurements and investigates opportunities for applying the knowledge we obtained.

Chapter 2

Theoretical background

2.1 Stellarator optimization

While axisymmetric magnetic configurations, like tokamaks, have theoretically perfect fast-ion confinement, stellarators' equilibrium needs to be highly optimized to reach similarly good confinement properties [21]. In tokamaks, the magnetic field is invariant with respect to the toroidal rotation $\partial \vec{B} / \partial \varphi = 0$, thus there exists a constant of motion which ensures the closing of particle drift orbits [22] for a single particle. This means, that collisionless particles would not leave their corresponding flux surface. In the case of stellarators with complex 3D magnetic field structures, they do not have such symmetries generally, which means that particles can easily drift radially. Despite this complication of stellarators, it can be shown that good confinement of collisionless particles can be achieved by imposing restrictions on the magnetic field strength, $B = |\vec{B}(s, \theta, \varphi)|$, if it has one of the following quasi-symmetries:

- $B = B(s, \theta)$, quasi-axisymmetry (QA),
- $B = B(s, \varphi)$, quasi-poloidal symmetry (QP),
- $B = B(s, M\theta - N\varphi)$, quasi-helical symmetry (QH),

where (s, θ, φ) are the so-called Boozer-coordinates [23] often used in plasma physics, in which magnetic field lines are straight, s is the flux label, θ is a poloidal while φ is a toroidal angle similarly as introduced in figure 1.2. M and N are integers. For example in the case

of W7-X [9], $N = 5$, the device has 5 fold symmetry, while the M can be chosen between $M = 4, 5, 6$ by varying the currents of the magnetic field coils.

The quasi-symmetries provide a corresponding invariant quantity which ensures the confinement of the collisionless orbits. Figure 2.1 shows the magnetic field strength as a function of the toroidal and poloidal straight field line angles for a general, not optimised stellarator as well as for the three quasi-symmetries introduced earlier.

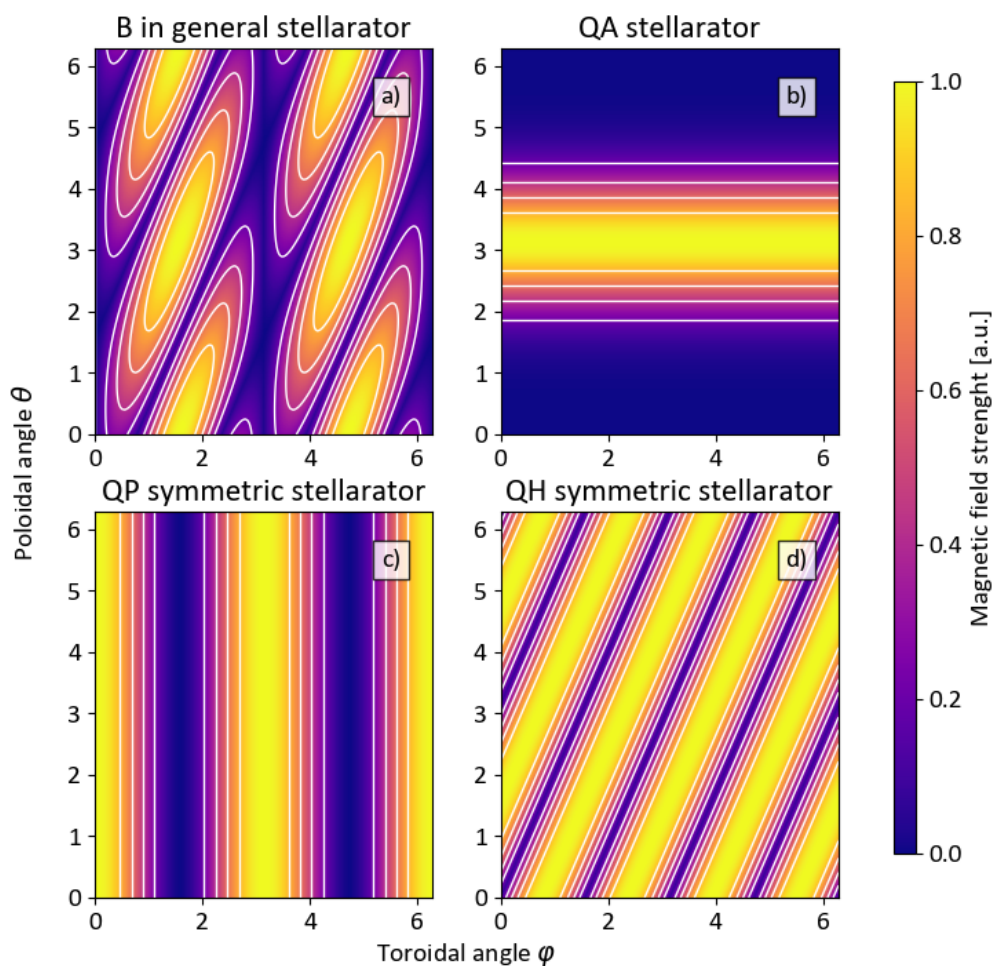


Figure 2.1: Magnetic field strength on a flux surface as a function of toroidal and poloidal angle. b), c) and d) show different types of quasi-symmetric stellarators that can ensure good confinement of drift orbits. Contours of constant magnetic field strength are shown in white.

It was found that good collisionless particle confinement can be achieved by a more

general, so-called quasi-isodynamic field configuration which is characterized by poloidally closing contours of the magnetic field strength. W7-X is such a quasi-isodynamic stellarator that can be categorized, together with other quasi-symmetric devices, as omnigenous. Omnigenity means that there are no net drifts away from a given flux surface [21, 24]. Its magnetic field strength around $s \approx 0.25$ is depicted in figure 3.1 for the symmetry period of the device. We can observe poloidally closing magnetic field contours and the magnetic field valley between.

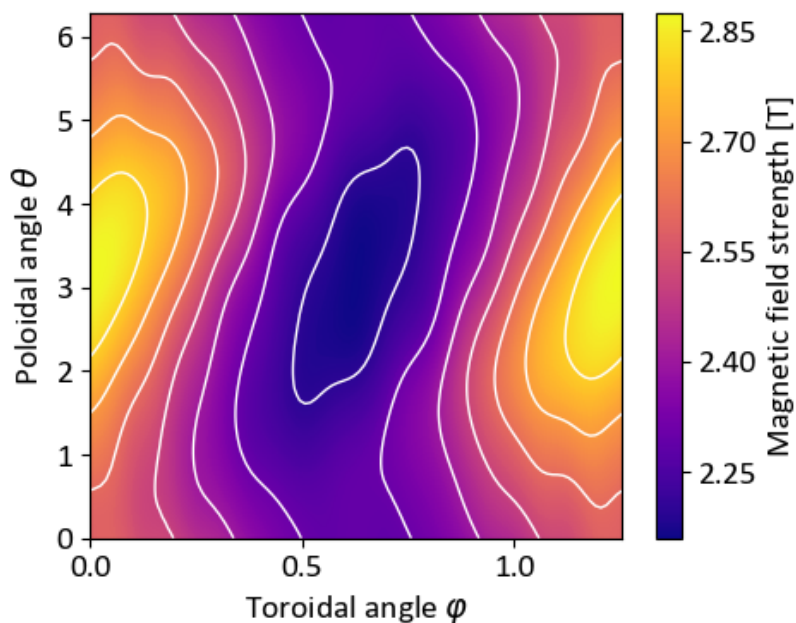


Figure 2.2: Magnetic field strength on a flux surface around $s \approx 0.25$ as a function of toroidal and poloidal angle for W7-X. Contours of constant magnetic field strength are shown in white.

2.1.1 Classes of collisionless particles orbits

In a toroidal system, in which we want to realize thermonuclear fusion, the static magnetic field provides confinement of particles. Although radial drifts might arise due to the curved magnetic field topology, which left uncontrolled would lead to degradation of this confinement. To understand the properties of particles exhibiting strong radial drifts first we characterise classes of possible particle orbits by investigating invariant quantities of motion.

A single particle's magnetic momentum, the ratio of its energy in its perpendicular motion to the magnetic field ($W_{\perp} = 1/2mv_{\perp}^2$) and the magnetic field strength, $\mu = W_{\perp}/B$ is a conserved quantity in case of a slowly evolving magnetic field [25]. As the strength of the magnetic field can vary along the path of the charged particle (see figure 2.3) the perpendicular velocity must change accordingly. Since the total particle energy is conserved as

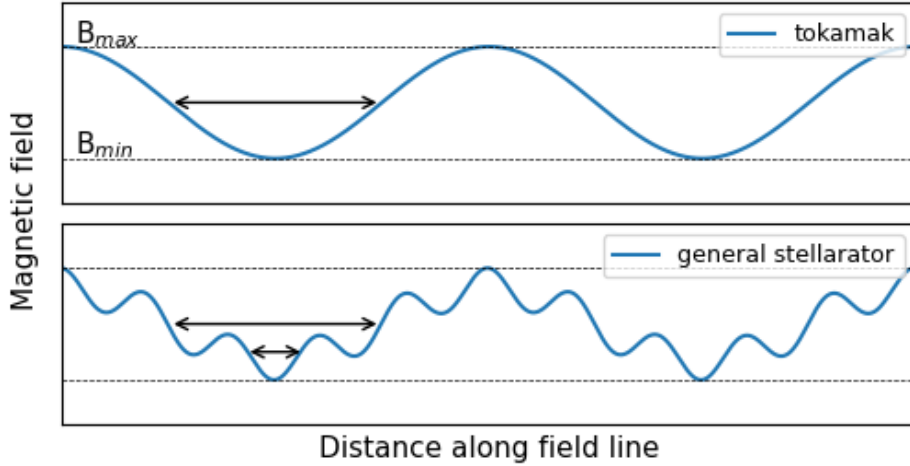


Figure 2.3: Magnetic field strength along a field line for different types of toroidal magnetic configurations.

well, a particle can only enter a higher magnetic field region by reducing its parallel velocity and increasing the perpendicular one. However, if a particle does not have sufficient initial parallel velocity, it will get trapped in the low magnetic field region. The corresponding condition for particle trapping can be expressed with the following equation:

$$\Lambda = \frac{v_{\parallel}}{v} < \left(1 - \frac{B_{min}}{B_{max}}\right)^{1/2}. \quad (2.1)$$

Particles with low initial pitch, Λ , will be trapped along their path in a magnetic well. Based on this we distinguish trapped- and passing particle orbits, which are depicted in figure 2.4 for a realistic tokamak magnetic field for simplicity. While passing particle orbits follow flux surfaces, trapped particle orbits exhibit strong radial drifts as depicted in figure 2.4. In the case of tokamaks, the magnetic field decays with $1/R$ such that a field line, being helically wound around a flux surface will experience high and low field regions in the inboard and outboard sides respectively. This means that trapped particles will be located

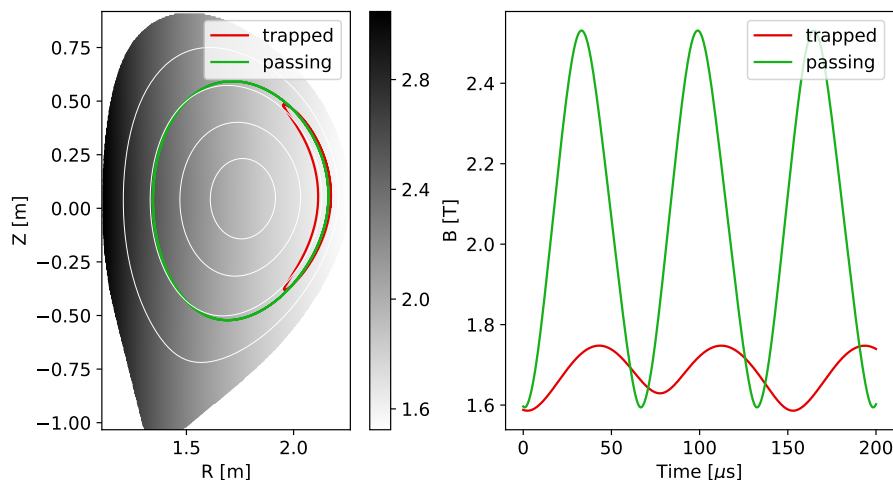


Figure 2.4: Projection of different particle orbits in a tokamak. With red trapped and with green passing particle orbits in a poloidal cross-section of a tokamak plasma are depicted. Magnetic field strength experienced by charged particles through their path.

at the low-field side, at the outboard side of the device. The particles form so-called banana orbits, which can be seen in figure 2.4, with motion into opposite toroidal directions on the inner and outer sides of the banana. Since the particle will spend slightly more time on the outboard side, a toroidal precession motion will appear. This precession motion is parallel to the contour lines of the magnetic field, the banana bounce point will always be at the same magnetic field strength such that banana orbits are closed in a poloidal projection.

In stellarators with complex magnetic field topology, trapping occurs in so-called helical wells in which the precession motion is not necessarily parallel to the contours of the magnetic field anymore. Thus, the bounce points will be located in different magnetic field strength regions such that drifts between the two bounce points are not balanced. This in turn leads to a net displacement of the banana orbit and, hence, to unconfined drift orbits. Because of this W7-X was optimized for a quasi-isodynamic magnetic field structure where the precession motion of trapped particles is aligned with contours of the magnetic field [26].

2.1.2 Plasma β effects on collisionless particles

Optimization of a stellarator's magnetic field for good plasma performance is particularly challenging as the equilibrium configuration depends on the plasma pressure itself. Plas-

plasmas with high normalized pressures, usually expressed as the ratio of kinetic and magnetic pressure $\beta = p/(B^2/2\mu_0)$, experience an outwards directed force which results in a compression of flux surfaces on the low-field side (also called Shafranov-shift) [27, 28]. This modifies the plasma equilibrium such that optimization of W7-X could only be achieved for a given domain of plasma pressure. Since W7-X was designed for demonstrating good confinement in high-performance plasmas [9], this working point was chosen at a volume-averaged beta value of 4%.

This dependence of the collisionless fast-ion confinement quality on plasma β in W7-X is discussed in [29] in details. Here we present a short overview of it. Figure 2.5 shows

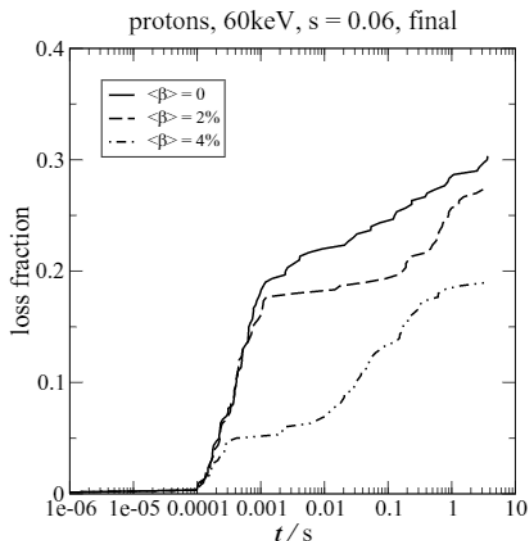


Figure 2.5: Evolution of the loss fraction of 60 keV hydrogen markers, initialized on the flux surface $s = 0.06$ (in the plasma core) at the final coil realization of Wendelstein 7-X. Adapted from [29].

how the loss fraction of core-born fast-ions with 60 keV energy evolve as a function of time, in the case of different volume averaged pressures. Since fast-ions initially have an isotropic velocity distribution, there exists a part of the population with high perpendicular velocities representing deeply trapped particles. These are poorly confined and lost quickly, in the time range of $10^{-4} \text{ s} < t < 10^{-3} \text{ s}$, and are called prompt losses. We can see that as $\langle\beta\rangle$ increases, the plateau value after the prompt losses decreases, at $\langle\beta\rangle = 4\%$, it goes below 5%. The remaining particle population then further evolves in time, slowly drifting outwards from the plasma, and finally, we can examine the long term collisionless particle confinement. When considering a time-point at 100 ms after the injection, one can see

that the loss fraction of core-initialized 60 keV fast ions decrease from 25% at $\langle\beta\rangle = 0\%$ to 15% at $\langle\beta\rangle = 4\%$, thus the confinement of fast particles increases. The behaviour of the curves after 100 ms can be neglected as typically fast-ions slow down on this timescale in collisional plasmas.

As W7-X is the first stellarator designed considering plasma β effects on the fast particle confinement, diagnosing the fast ion population and demonstrating the improvement with beta experimentally is a crucial cornerstone of its objectives.

2.2 Sources of fast-ions

In future reactors, the main fast-ion population will be fusion-born alpha particles as a result of DT reactions, with Larmor-radii around 10 cm (considering their energy of 3.5 MeV, and typical magnetic field strength of 2.5 T). As present-day devices usually do not operate with a mixture of deuterium and tritium, therefore other means of fast ion production is required. One of the commonly used methods of generating fast-ions is the use of a neutral beam injection (NBI) system, which injects fast neutrals into the plasma which get ionized there. The injection of neutral particles is required to avoid charged particle deflection in the strong magnetic field, and provide deeper penetration of the beam into the plasma column. The schematics of a typical NBI system can be seen in figure 2.6. At the ion source, positively charged hydrogen ions are produced which are then accelerated through an acceleration grid at high voltages ranging from 20 to 150 kV in present-day devices. This range of energies is covering the space to mimic fusion born alpha particle orbits at the various magnetic fields in the plasma and it can be tuned to provide good penetration of the neutrals. After this, accelerated ions are driven through a neutralizer gas, where they return to a neutral state via charge exchange reactions. The remaining non-neutralized ion fraction is deflected with strong magnets and thus a beam of neutralized hydrogen species is injected into the plasma. It should be noted that H_2^+ and H_3^+ molecules are also formed in positive ion sources in addition to H^+ ions, which dissociate in the neutraliser after acceleration, giving rise to populations with half and third energy arriving at the plasma.

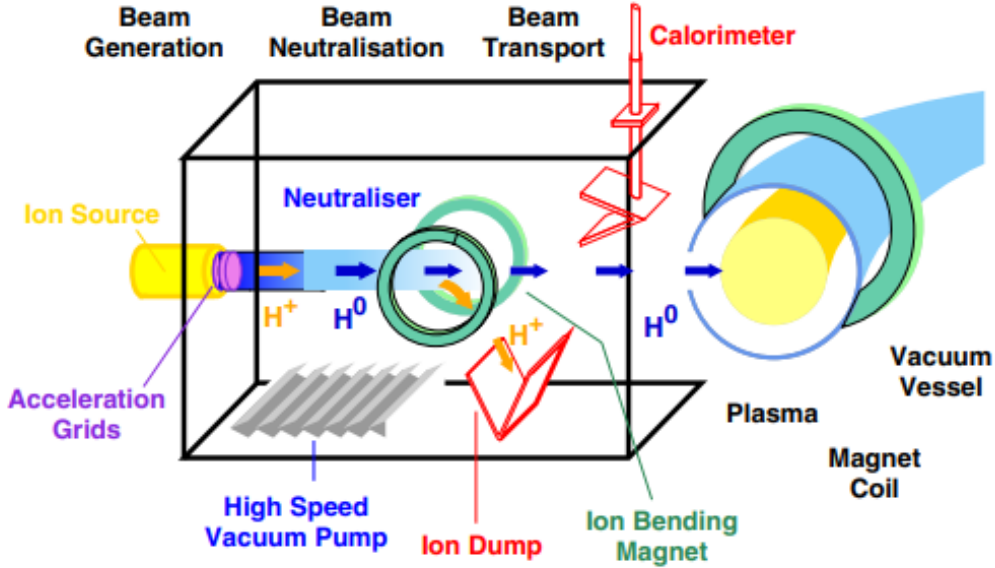


Figure 2.6: Schematic of an NBI injection system. Ions are generated at the yellow ion source, accelerated and focused with high voltage. Then they are neutralized, and the rest of the charged particles are diverted with strong external coils ('ion bending magnet') depicted with green. The rest of the neutral beam then arrives at the plasma.

2.2.1 Fast-ion slowing down

So far we discussed the collisionless behaviour of charged particles in stellarators, but in order to understand the experimental relevant time scales as well, investigation of their collisional transport is required. Using kinetic plasma theory the evolution of the fast-ion distribution function $f_\alpha(\vec{r}, \vec{v}, t)$ can be described with the following partial differential equation [30]:

$$\frac{\partial f_\alpha}{\partial t} + \vec{v} \cdot \nabla f_\alpha + \frac{q}{m} (\vec{E} + \vec{v} \times \vec{B}) \cdot \frac{\partial f_\alpha}{\partial \vec{v}} = C(f_\alpha) \quad (2.2)$$

where \vec{E} and \vec{B} mark the macroscopic equilibrium electric and magnetic fields and \vec{v} is the flow velocity. Interaction of the investigated population, in our case the fast-ions, with the collective background particles is described with the collision operator $C(f_\alpha) = (\partial f_\alpha / \partial t)_{coll}$. The collision operator describes the effect of the Coulomb collisions of charged particles on the fast ion distribution, which includes pitch angle scattering and thermalization process of it. The form of the collision operator can be expressed analytically assuming Maxwellian background electrons and ions [31].

To connect measurable parameters (fast ion energy, fast ion density etc), and their

change in time, with the kinetic equation 2.2, moments of it (i.e. integrals over the velocity space of f_α) is generated and analyzed. Thus first we investigate the rate fast-ions are losing their energy E_α [32] in order to obtain characteristics of their interaction with the background plasma:

$$\frac{dE_\alpha}{dt} = \left(\frac{dE_\alpha}{dt} \right)_{coll,e} + \left(\frac{dE_\alpha}{dt} \right)_{coll,i} \propto -\frac{E_\alpha}{T_e^{3/2}} - \frac{C}{E_\alpha^{1/2}}, \quad (2.3)$$

where T_e is the electron temperature and C is a constant ($C \approx 57$). Here, the change of fast-ion energy is separated into collisions with electrons and ions. Investigating the first term we see, that with increasing fast-ion energies the energy loss rate due to electron collisions increases, as their interaction time increases as well. Note here that usually the $v_e > v_\alpha > v_i$ holds in typical plasmas. As for the second term, with increasing fast-ion energies the fast-ion energy loss rate decreases as the interaction time decreases. These observations imply the existence of a so called critical energy level of the fast-ions above which slowing down and energy loss on collisions with electrons is larger and below which interaction with ions will be larger. For a pure hydrogen plasma this critical energy E_c can be approximated:

$$E_c \approx 15T_e \quad (2.4)$$

For example in W7-X, the core electron temperature is typically 4 keV, thus the critical beam energy is at 60 keV. As the NBI injection energy is slightly lower than that at W7-X, 55 keV in hydrogen, this implies that initially fast-ions will lose energy in a similar order to electrons and ions both and as they further slow down interaction with ions will become dominant in the plasma core. While in the plasma edge with lower temperatures (0.5 keV) the interaction with electrons can be initially dominant as the fast-ion energy is larger than the critical energy. Then finally the slowing down time of fast-ions, τ_0 is described by [33], the time required for them to thermalize:

$$\tau_0 = \frac{\tau_s}{3} \ln \left(1 + \left(\frac{E_0}{E_c} \right)^{3/2} \right), \quad (2.5)$$

where τ_s is the Spitzer time of fast particles assuming $v_e \gg v_\alpha \gg v_i$:

$$\tau_s = \frac{3(2\pi)^{3/2} \epsilon_0^2 m_\alpha T_e^{3/2}}{Z_\alpha e^4 m_e^{1/2} n_e \ln \Lambda} \propto \frac{T_e^{3/2}}{n_e} \quad (2.6)$$

Here, T_e and n_e are the electron temperature and density, m is the mass of electrons and fast-ions, Z_α is the charge of the fast ion, $\ln \Lambda$ is the Coulomb logarithm [3] and other physics constants such that the elementary charge e and the dielectric constant ϵ_0 .

Slowing down times for the parameter space W7-X can explore are shown in figure 2.7. With increasing density the slowing down time decreases and with increasing electron

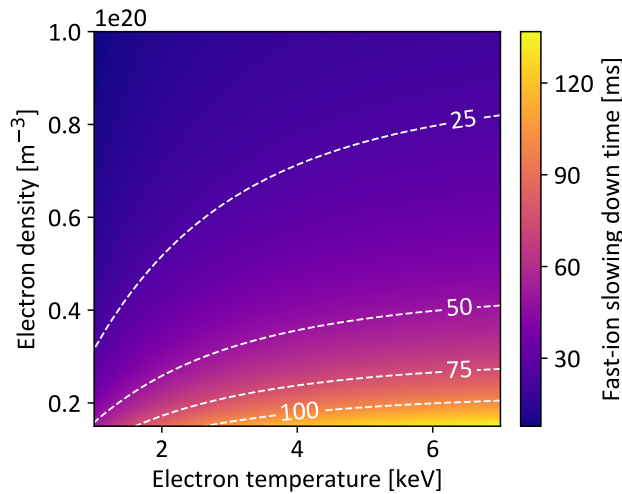


Figure 2.7: Slowing down time of fast ions with 55 keV initial energy for different W7-X relevant electron temperatures and densities

temperatures the slowing down time increases. In the core of W7-X at $n_e = 5 \cdot 10^{19} \text{ m}^{-3}$ and $T_e = 4 \text{ keV}$, the fast-ion slowing down time is 36 ms assuming 55 keV hydrogen fast particles.

Although characteristic time scales can be estimated, as shown before, to predict the total fast-ion distribution f_α , detailed modelling required considering the collisions of fast-ions with the background plasma.

2.2.2 Fast-ion slowing down simulations with ASCOT

Several modelling tools exist to predict fast-ion distribution functions, $f_\alpha(\vec{r}, \vec{v}, t)$, following neutral beam injection such as TRANSP [34], VENUS [35], or RABBIT [36]. For the work presented here, the ASCOT4 code [37] was used.

ASCOT4 is a full 3D, Monte Carlo test species orbit following code for fusion plasmas, developed and maintained by the Aalto University. Its goal is to follow minority plasma

species like fast-ions or impurities in an external magnetic field and simulate their interaction with the background plasma in order to predict the spatial- and temporal evolution of the minority species distribution function. First ASCOT produces the initial distribution of fast-ions in the investigated plasma. For this, it uses a realistic NBI system model which launches multiple, $\mathcal{O}(10^6)$ test neutral markers towards the plasma volume and predicts where they are ionized based on beam stopping coefficients [38]. The test markers now represent fast ions that gyrate and travel spatially until they collide with electrons or ions, changing their pitch (pitch angle scattering) and losing their energy. Figure 2.8 shows an example equilibrium fast-ion distribution function predicted with ASCOT4, where the neutral beam injection energy was at 48 keV. Peaks in the distribution function can be

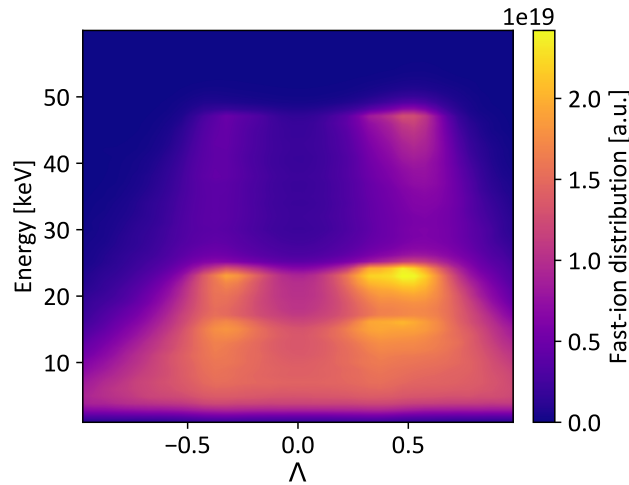


Figure 2.8: Plasma volume integrated fast-ion distribution function predicted by ASCOT4 for a W7-X plasma at injection energy of 48 keV.

seen where fast-ions are born at 48, 24 and 16 keV, matching the full, half and third energies of the neutral beam injection heating system. The initial pitch of the distribution is determined by the alignment of the injection system compared to the magnetic field structure, which is $|\Lambda| \approx 0.5$ in this case. It can be seen that the distribution function apart from the injection peaks is symmetric in Λ as trapped particles are bouncing back and forth in the magnetic well, changing their parallel velocity's sign. As fast particles interact with the background plasma, they initially lose their energy but their pitch angle won't change significantly since electron-ion collisions do not lead to significant scattering. After particles reach the critical energy around 30 keV, ion-ion collisions become relevant

too and pitch angle scattering becomes more efficient, changing the pitch and providing a wide variety of particle orbits and scattering some particles into trapped orbits.

2.3 Recycling neutrals

The confined and highly ionized plasma is surrounded by a neutral gas cloud, which forms due to out-gassing of the plasma vessel walls, recycling of ions from the different plasma-facing components and dedicated gas fuelling of e.g. H_2 . The neutral density in the plasma is set by the balance of influx of neutral particles and ionization. Its penetration depth, λ_n of neutrals into the plasma can be estimated by calculating the effective distance a neutral can travel assuming electron impact ionization:

$$\lambda_n = \frac{v_e}{n_e \langle \sigma_{ion} v_e \rangle}. \quad (2.7)$$

Inserting relevant numbers for W7-X, we arrive that neutrals can penetrate roughly 5 cm before getting ionized. This penetration length is further increased as neutrals can penetrate into the main plasma volume through consecutive charge-exchange process.

2.3.1 KN1D

In order to estimate the background neutral density (which is needed to estimate passive CX reaction contributions), the kinetic neutral transport code KN1D can be used [39]. KN1D calculates the H^0 atom and H_2 molecule density in a 1D slab geometry with specified plasma profiles (temperature, density) and assumed a given H_2 pressure at the vessel wall. The code considers the interaction of neutrals with plasma charged particles, which consist of impact excitation, ionization and dissociation by electrons and by ions, as well as charge-exchange reactions. Moreover, it considers the neutral-neutral interactions and elastic collisions. Schematics of the simulation regions is shown in figure 2.9.

The code solves the following equation for both H^0 and H_2 species (marked with α) in order to get the spatial distribution f of given species:

$$v_\alpha \frac{\partial f_\alpha}{\partial x} = \left(\frac{\partial f_\alpha}{\partial t} \right)_{coll} + S_\alpha \quad (2.8)$$

where v_α is the velocity and S_α is the source term of α species. The simulation domain

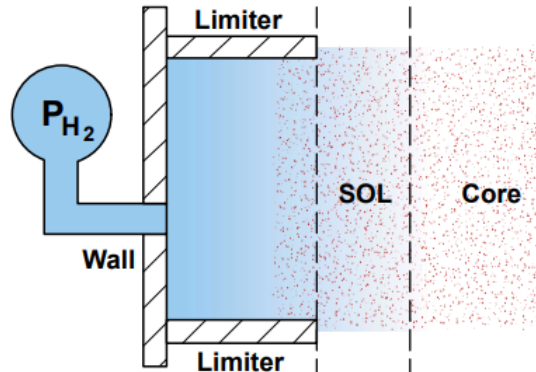


Figure 2.9: Simulation geometry of KN1D, adapted from [39]. The rightmost dashed line marks the boundary between the core plasma and scrape off layer (SOL) with open field lines. The leftmost dashed line marks the boundary of the SOL and limiter shadow region of the plasma.

extends from the boundary wall, through the limiter shadow and scrape off layer region to the main plasma volume. The scrape off layer (SOL) is the interface between open and closed field lines. Open field lines are characterised as field lines ending on the wall element, thus providing an efficient particle and heat transport through parallel streaming along it. Using the set boundary condition of wall H_2 pressure, the H_2 density can be calculated by iterating over elastic collisions, which then provides the source term through dissociation for the H^0 species and H^0 calculations. 2.9 Example KN1D input temperature and density

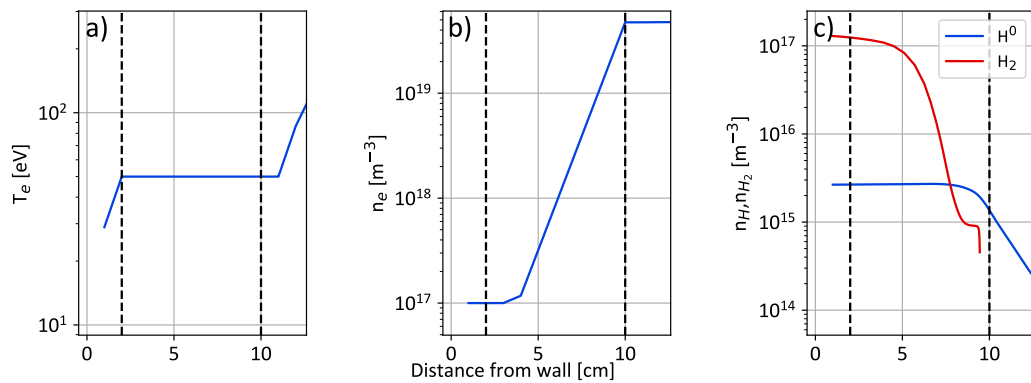


Figure 2.10: a), b) assumed kinetic profiles in the plasma edge and c) calculated H_2 (red) and H^0 (blue) by KN1D.

profiles in the edge region can be seen in figure 2.10 a) and b), and the output of the code, H_2 (red) and H^0 (blue) densities are shown in c). The limiter and SOL positions are marked with black dashed lines as depicted in figure 2.9. If figure 2.10 c) it can be seen

that close to the wall the H_2 dominates the neutral density but it quickly falls off in higher density regions due to dissociation. The H^0 density stays constant in the edge and has an exponential decay towards the core plasma (away from the wall). In the present the H_2 and H^0 densities are poorly diagnosed at W7-X, 3D information about their distribution is not routinely available. Because of this, we rely on modelling of the neutral hydrogen density. Although there exist more sophisticated models for predicting the SOL hydrogen density, such as EMC3-EIRINE [40], we refrain from using due to its complexity. As the results of KN1D are dependent on assumptions we made, profile shape, wall and limiter shadow region boundary positions, wall pressure etc., the resulting neutral density profiles are only used tentatively.

Chapter 3

The Wendelstein 7-X stellarator

3.1 Parameters and design criteria

Wendelstein 7-X (W7-X) is a neoclassically optimized modular, superconducting stellarator in Greifswald, which started its operation in 2015 with the overarching goal of demonstrating fusion reactor relevant performance.

It was designed using the numerous optimization criteria [41] which included good quality magnetic surfaces with minimal magnetic field imperfections, small outwards shift of magnetic surfaces at high plasma pressures, stability against magneto-hydrodynamic instabilities, good fast particle confinement in the reactor relevant low-collisionality regime (high temperature), low plasma currents and reasonable feasibility of the magnetic field producing coils [42].

With the careful design of this precision fusion plasma device, it aims to achieve reactor relevant high ion densities and temperatures ($n > 10^{20} \text{ m}^{-3}$, $T > 5 \text{ keV}$) at long plasma operation with active density and impurity control, to prove the stability of plasma equilibrium at high plasma pressures and to operate the superconducting coils in a steady-state [42]. One other high-level design goal is to prove good confinement of fast particles at reactor relevant parameter space [41, 42, 43] which we intend to address.

W7-X is a device with 5 fold symmetry, major radius of 5.5 m and an effective minor radius of 0.5 m ($a = \sqrt{V/(2\pi^2 R)}$), giving a total plasma volume of about 30 m^3 . Its structure is depicted in figure 3.1. The 50 non-planar and the 20 planar coils are colored red and orange respectively. Additional support structures, cryostat and diagnostic port openings are colored grey. The plasma-volume is illustrated with light blue. The superconducting

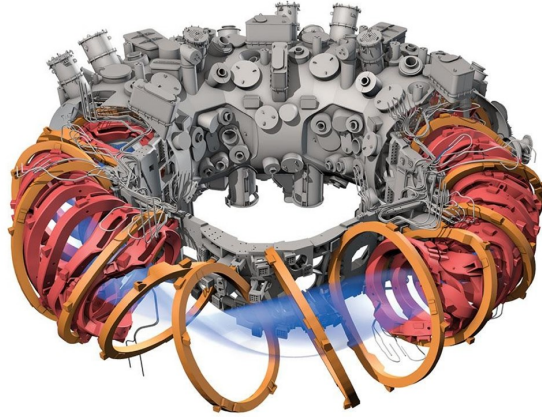


Figure 3.1: Adapted from [9]. Structure of W7-X stellarator. Cryostat, support structure and the numerous ports are depicted with grey where. Planar and non-planar coils are depicted with orange and red colors. The plasma volume is shown in light blue color.

coils typically provide an on axis magnetic field strength of 2.5 T, but it can be varied between 1.7 T and 3 T.

3.2 VMEC equilibrium calculations

The structure of the equilibrium flux surfaces (flux surface position, magnetic field structure) is used to map profiles of different plasma parameters and later to track particle orbits. To account for the impact of the plasma itself on the magnetic field (deviations from the vacuum field), the VMEC code [44] is used at W7-X which solves the force balance equation described in 1.4. VMEC establishes the position of flux surfaces in real space coordinates for a given pressure and current profile by minimizing the system's energy functional:

$$W = \int \left(\frac{B^2}{\mu_0} + p \right) dV \quad (3.1)$$

which is the sum of its magnetic- (B^2/μ_0) and thermal energy. By calculating the energy functional for various conditions, one can obtain the flux surface shape and position which provides the minimum energy. The flux surfaces are described by R_{mn} and Z_{mn} Fourier

coefficients for each flux coordinate s :

$$R = \sum R_{mn}(s) \cos(m\theta - N_p n\varphi) \quad (3.2)$$

$$Z = \sum Z_{mn}(s) \sin(m\theta - N_p n\varphi) \quad (3.3)$$

where m and n are integers describing the periodicity of the field and θ and φ are the poloidal and toroidal angles, respectively. N_p is the number of field periods, which in the case of W7-X is 5. Figure 3.2 shows a 3D view on the VMEC-predicted last closed flux surface, as well as poloidal cross-sections at two different toroidal positions. The shapes of these two poloidal cross-sections are commonly referred to as bean- and triangle shape. In

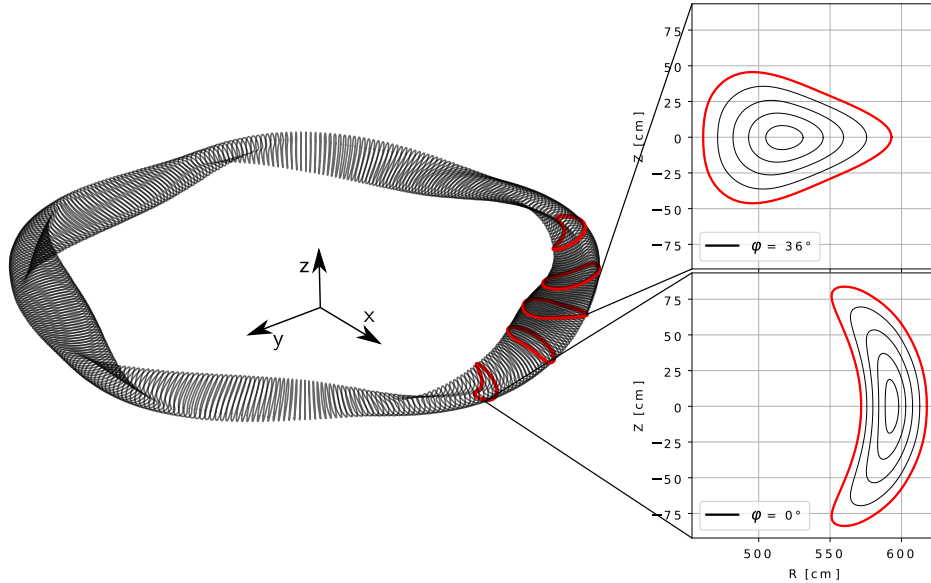


Figure 3.2: Flux surfaces calculated by VMEC for W7-X. On the left hand side the last closed flux surface is depicted from a side view which shows the device's 5 fold symmetry. At $\varphi = 0$ and 36° , the 'triangular' and 'bean' shaped poloidal cross sections are plotted on the right hand side.

addition to the 5 fold rotational symmetry of the flux surfaces, the equilibrium has another mirror symmetry [45], which can be expressed in cylindrical coordinates as the following:

$$s(R, -z, -\varphi) = s(R, z, \varphi) \quad (3.4)$$

where s is the flux surface label introduced in equation 1.5. This implies that within a module (5th of the device) the flux surfaces are smoothly transforming from the 'bean' shape to the 'triangular' shape then from there the same transition happens while having

the flux surfaces mirrored to the horizontal plane.

The rate at which a magnetic field line rotates about the magnetic axis is defined by a quantity called the rotational transform:

$$t = \lim_{\varphi \rightarrow \infty} \frac{1}{\varphi} \int_0^\varphi \frac{d\theta}{d\varphi'} d\varphi' \quad (3.5)$$

The integral counts how many times on average a field line progresses around poloidally for each toroidal turn. In W7-X the iota profile can be varied, driving different ratios of currents in the magnetic field coils. The standard magnetic field configuration of W7-X, the high mirror and the low-iota configuration have an iota profile that is slightly below one, while the high-iota configuration has an iota-profile above one. As can be seen in

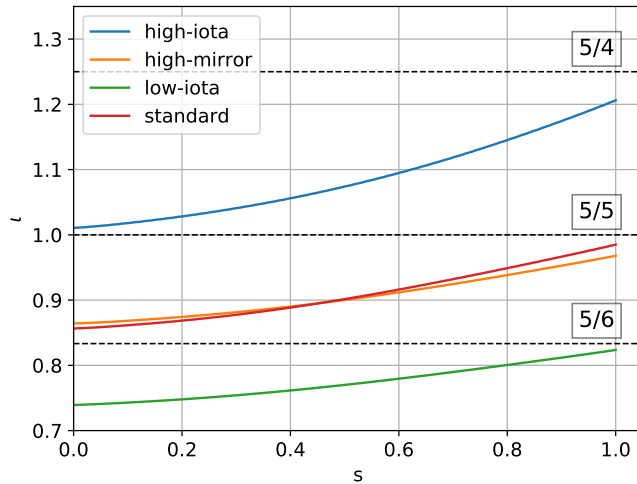


Figure 3.3: Different colors mark iota profiles in different magnetic configurations. These are produced by varying the ratio of currents in coils in W7-X.

figure 3.3, the iota profiles of the various configurations are considered low shear. It avoids crossing flux surfaces with low-rational iota value in the main plasma volume, as it would lead to the formation of magnetic islands and degradation of plasma performance [46]. Low-order rational flux surfaces are only crossed in the edge of the confined region (5/5, 5/4, 5/6, marked with dashed lines) leading to island formation depicted with different colors in figure 3.4. These islands are used to build a so-called divertor structure around which allows dissipation of heat and particles in designated regions far away from the main confined plasma volume [47]. In figure 3.4 the 5/5 islands of the standard configuration

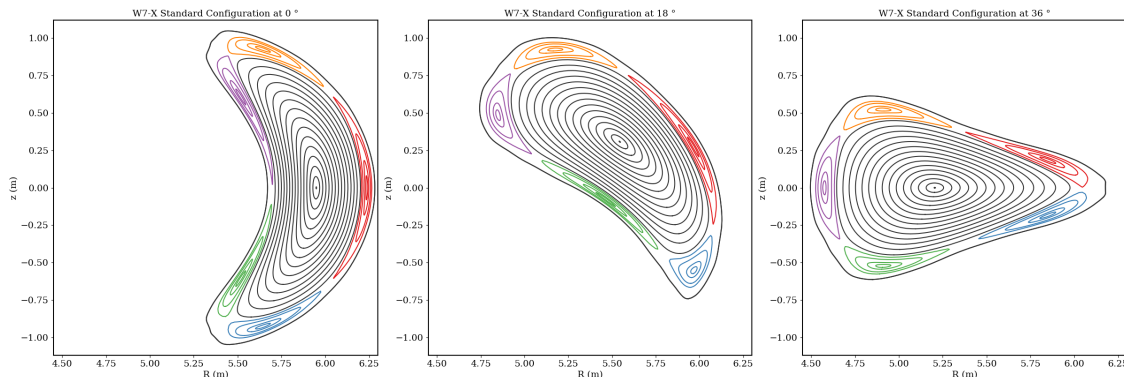


Figure 3.4: As the iota profile crosses a rational surface ($5/5$ in case of the standard configuration) islands form in the W7-X edge. These are being depicted with colored nested tubes at different poloidal cross sections of the device. By courtesy of Carsten Killer.

are depicted with different colors in different poloidal cross section of W7-X. Each color corresponds to a separate island. VMEC calculations do not support the prediction of the position of these islands, thus additional modelling is required in this region in order to incorporate its presence and effect on simulations.

3.3 Heating systems

For plasma startup of future fusion devices, but also for the operation of present-day fusion experiments, auxiliary heating methods are needed [3]. W7-X is equipped with electron cyclotron resonance heating (ECRH) and neutral beam injection (NBI) heating which will be discussed in the following.

3.3.1 Electron cyclotron resonance heating

Electron cyclotron resonance heating (ECRH) systems generate microwaves with wavelengths of few mm, which are then guided to the plasma. By matching the microwave frequency f , with harmonics of the electron cyclotron frequency $f_c = q|B|/(2\pi m_e)$, $f = n f_c$, where n is an integer at a given position in the plasma, the perpendicular velocity of the electrons can be increased. Due to the high collision frequencies of electrons inside of fusion plasmas, the accelerated electrons will slow down and heat the bulk plasma. Microwave injections with a polarization perpendicular and parallel to the experiment's magnetic field

are both used, and are called X- or O mode heating respectively [48]. While X-mode heating is needed to start plasmas, as it has better coupling to low temperature plasmas, O-mode heating allows reaching higher densities thanks to its higher cut-off density, above which the launched waves cannot penetrate the plasma anymore. W7-X is equipped with 10 long-pulse capable 140 GHz gyrotrons (2^{nd} harmonic heating at 2.5 T), providing on average 0.8 MW per source, both in X- and O-mode [49]. The location of absorption can be varied using steerable mirrors providing on- and off-axis heating.

3.3.2 Neutral beam injection

Wendelstein 7-X is currently equipped with two beam boxes (later referred to as NI20 and NI21) [50, 51] with 4 NBI sources per each. The positioning of the 2 beam boxes was chosen such that they inject neutrals into a stellarator symmetric cross section of the plasma. Out of the possible 8 sources, 2 has been commissioned and operated in the previous experimental campaign. The injection geometry of the two beam boxes is depicted in figure 3.5 in 3D with respect to the flux surfaces of W7-X and in a poloidal cross section. The operational sources are colored green, while the rest is colored red. The width of the beams is indicated with opaque color around the line of sight of the beams. The two operational sources are referred to as S7 and S8. 4 beams from the same beam-box share the same transition line from the sources to the plasma, including the beam-duct, a long entrance port through which NBI injected particles enter the plasma vessel. As the beams have a significant width, around 20 cm, the port entrance scrapes a part of the beam, modifying its shape before it enters the plasma. S7 has a more radial injection direction, having a 91% beam duct transmission efficiency while S8 injects more tangentially, with 84% nominal transmission efficiency. The beam path in the plasma is approximately 1 m for each NBI source. The injection sources are operated with a positive hydrogen source with typically 50-55 kV acceleration voltage, which provides a nominal of 1.35-1.55 MW power to the torus per source. The beam particle flux fraction was measured with spectrometers looking into the beam neutraliser region, with common fractions found to be $E_1/E_2/E_3$ (full/half/third) of 0.3/0.6/0.1. To avoid damaging the plasma vessel or limiting operation duration, minimization of the not-ionized power, the shine-through losses is preferred. Figure 3.6 shows the calculated shine-through power fraction considering 1 m long beam path, in a slab geometry, with constant profiles, T_e

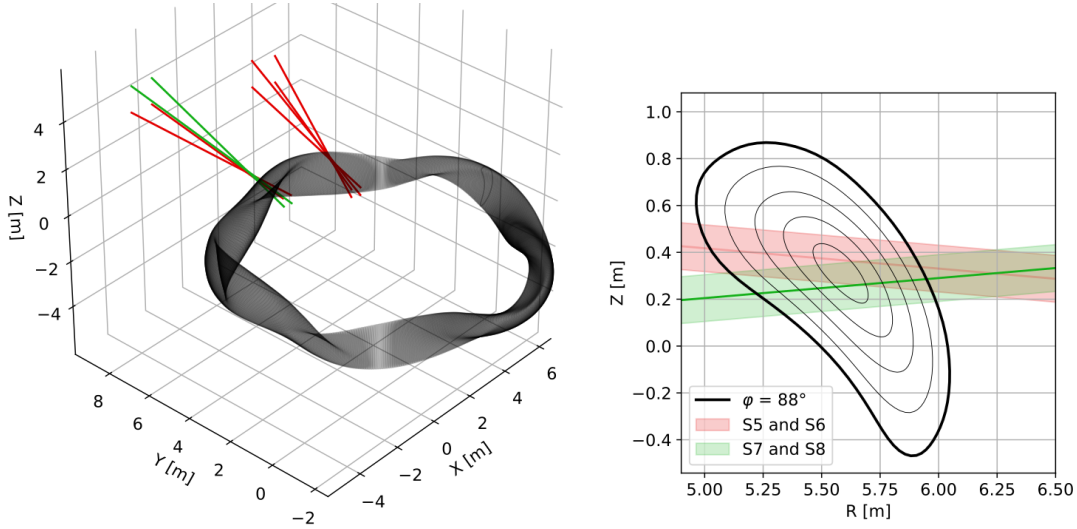


Figure 3.5: W7-X NBI system from an a) side view. In the 2018 campaign, S7 and S8 were operational in beam box NI21, marked with green, providing a total of 2.7-3.1 MW power to the torus [52]. Possible future beamlines are marked with red. b) beam injection in the poloidal cross-section at injection toroidal angle 88° .

$= T_i = 2 \text{ keV}$, $E_{inj} = 50 \text{ keV}$, beam particle flux fractions of $E_1/E_2/E_3 = (0.3/0.6/0.1)$ and different electron densities. Shine-through losses are monotonically decreasing with increasing density and it drops below 10% above electron density of $5 \cdot 10^{13} \text{ cm}^{-3}$. Based on this simple calculation shine-through power losses in regular plasma operation, where the plasma density ranges from $2 \cdot 10^{13} \text{ cm}^{-3}$ to $1.5 \cdot 10^{14} \text{ cm}^{-3}$, is in the range of 10-25%.

3.4 Main core diagnostics

This section introduces the main diagnostics used for this thesis, consisting of measurements of the electron density, the electron and ion temperature and the plasma rotation.

3.4.1 Thomson scattering

Electron density n_e and temperature T_e profiles are measured simultaneously at W7-X with a Thomson scattering diagnostic [53, 54].

This diagnostic consists of three parallel Nd:YAG lasers (1064 nm), with tuneable energies between 0.7 and 1.5 J operated at 10 Hz repetition rate. The laser beams are guided through the plasma where the electromagnetic wave is scattered on electrons. The corre-

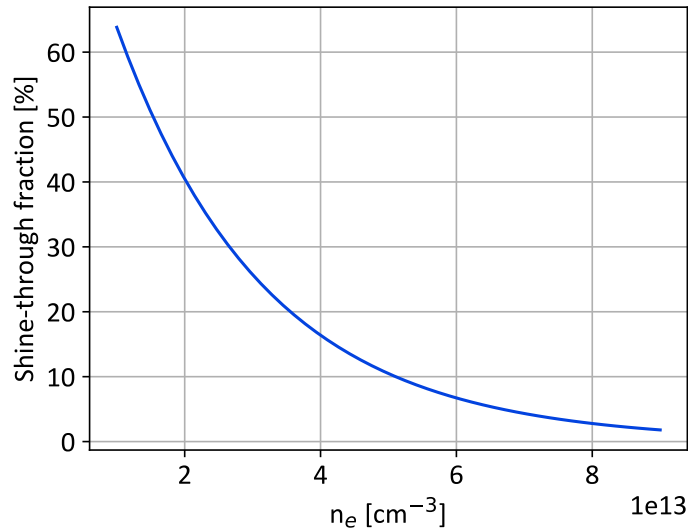


Figure 3.6: Shine-through power loss fraction calculated for a 1 m long $T_e = T_i = 2$ keV plasma slab at different densities, with realistic beam parameters, $E_{inj} = 50$ keV, $E_1/E_2/E_3 = (0.3/0.6/0.1)$

sponding scattered light intensity and spectral broadening, measured at the intersection between a given laser and line of sight, provides spatially resolved information on the electron density and temperature, respectively. The range of the lines of sight and the laser geometry of the W7-X Thomson scattering system are depicted in figure 3.7. As can be seen, two optical systems are used to collect light, allowing measurements both at the in- and outboard sides of the plasma. Representative profiles inferred by the Thomson-scattering system can be seen in figure 3.8 for discharge 20180823.037 at 4.6 s. The profiles are expressed as function of effective radius ($r_{eff} = a\sqrt{s}$). The dashed lines mark the location of the last closed flux surface. While the electron temperature profile is steeply decreasing, with core values of 3 keV, the density profile is considered flat, with peak values of $6 \cdot 10^{19} \text{ m}^{-3}$. Outside of the last closed flux surface, the temperature is low, but the density stays comparably high.

As the intensity of the 3 lasers varies between laser pulses there is significant uncertainty in the measured profile magnitude. Hence, the line integrated density measurements from a second diagnostic are used to cross-calibrate the density profiles from Thomson scattering. This diagnostic is discussed in the following.

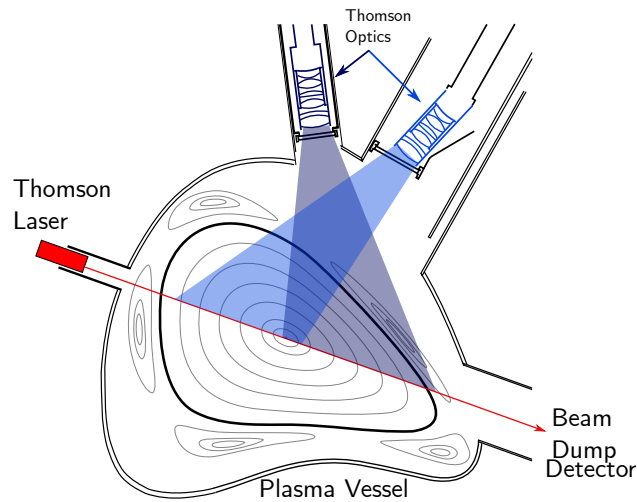


Figure 3.7: Diagram of the W7-X Thomson scattering system, consisting of two observation ports, and a high power pulsed laser. It measures density and temperature profiles in an almost triangular cross section of the plasma.

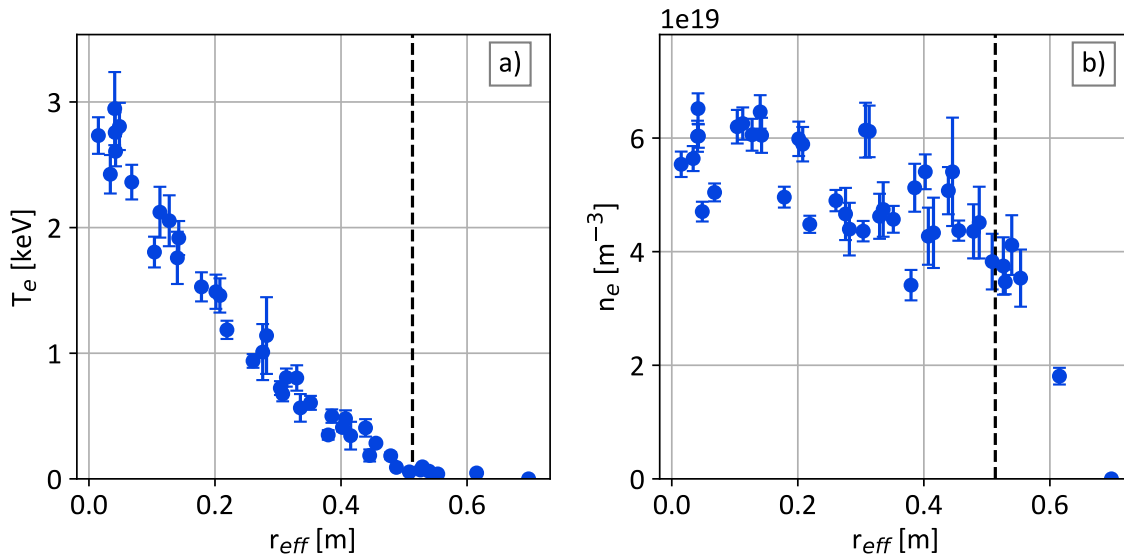


Figure 3.8: Typical Thomson scattering a) electron temperature and b) electron density profile in discharge 20180823.037 at 4.6 s.

3.4.2 Dispersion interferometry

The dispersion interferometer measures the line integrated plasma density with a sampling frequency of 50 kHz. The diagnostic makes use of the density-dependent phase shift experienced by electromagnetic radiation as it will be proportional to the line integrated electron density [55]. The phase shift can be observed by superimposing radiation that has experienced a phase shift with un-perturbed radiation, which results in an interference pattern. At W7-X a 20 W CO₂ laser source with a wavelength of 10.6 μm and its second harmonic, generated by a frequency doubling crystal, is used for interferometry [55]. It was designed to measure resilient phase difference against vibrations of different optical components. The laser beam path is almost identical to that of the Thomson scattering system which allows for the aforementioned cross-calibration. A typical interferometry measured

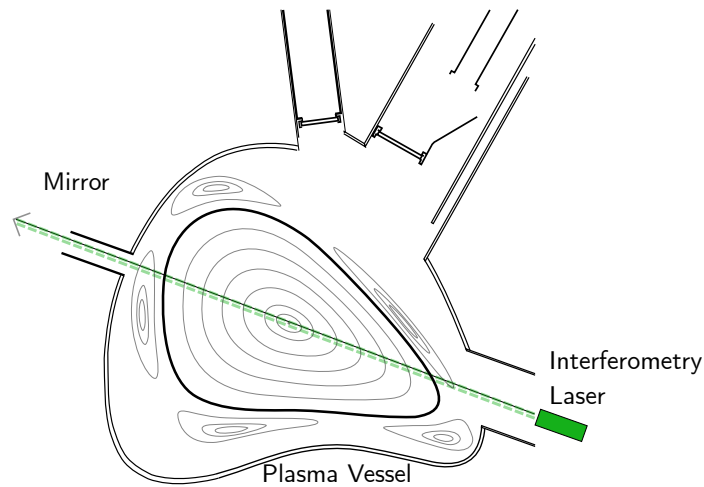


Figure 3.9: Drawing of the W7-X dispersion interferometry system, consisting of a strong laser and optical elements.

time-trace can be seen in figure 3.10 for the representative W7-X discharge for which the Thomson scattering data was shown previously. The plasma discharge lasted for 6 seconds and different fueling steps can be seen. At 1 s the plasma density is increased by increased gas injection, while between 4.5 and 5.5 s the NBI system is operational providing fueling, increasing the line integrated plasma density.

Compared to figure 3.8 Thomson scattering profile the measured line-integrated density

(with a line length around 1.3 m) is higher at 4.6 s ($7 \cdot 10^{19} \text{ m}^{-2}$) than one would expect based on the 1D Thomson profiles (maximum at $6 \cdot 10^{19} \text{ m}^{-3} \times 1.3 \text{ m}$). The discrepancy is around 20%, which demonstrates the importance of the cross-calibration.

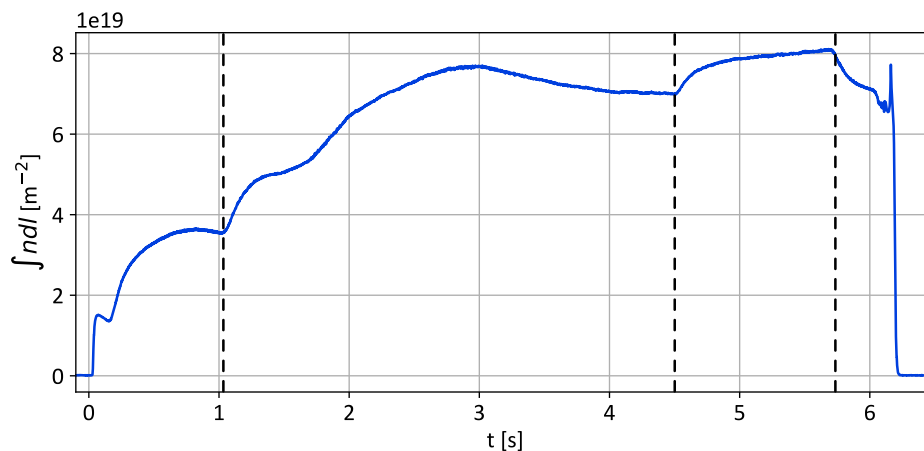


Figure 3.10: Typical time-trace of the interferometry measured line integrated electron density. Measured in discharge 20180823.037.

3.5 Active neutral beam spectroscopy

The application of neutral beams in fusion plasmas provides numerous measurement capabilities such as the measurement main ion temperature and rotation, impurity ion temperature and rotation, the effective charge and the fast-ion content [12, 17, 56]. In W7-X a multi purpose beam spectroscopy system has therefore been installed [57].

The system is built around the two operational NBI sources (S7 and S8) in module 2, introduced in chapter 3.3.2 and consists of three optical heads, which provide a toroidal observation geometry (A21 port) and two geometries that view NBI with an angle of roughly 45° (labelled M21 and T21). The geometry of NBI and three observation optics is depicted in figure 3.11. The three optical heads collimate the light from the plasma and feed it into about 100 m long relay optical fibers with an inner diameter of $400 \mu\text{m}$, which guide the radiation into a spectroscopy lab. In the laboratory, several spectrometers are used to study the radiation. For this work, a high light collection capable, single grating instrument, called the ITER-Like-Spectrometer (ILS) [58] is used which allows connecting 54 fibers (one fiber corresponds to one line of sight observation) at its entrance.

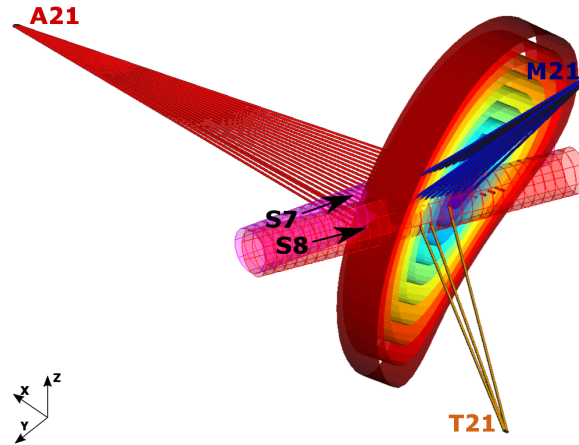


Figure 3.11: Lines of sight 3D geometry of the three different observation systems, looking at two NBI sources S7 and S8: red **A21** toroidal- and the orange **T21** and blue **M21** 45°.

The schematics of this spectrometer system can be seen in figure 3.12. The light enters the

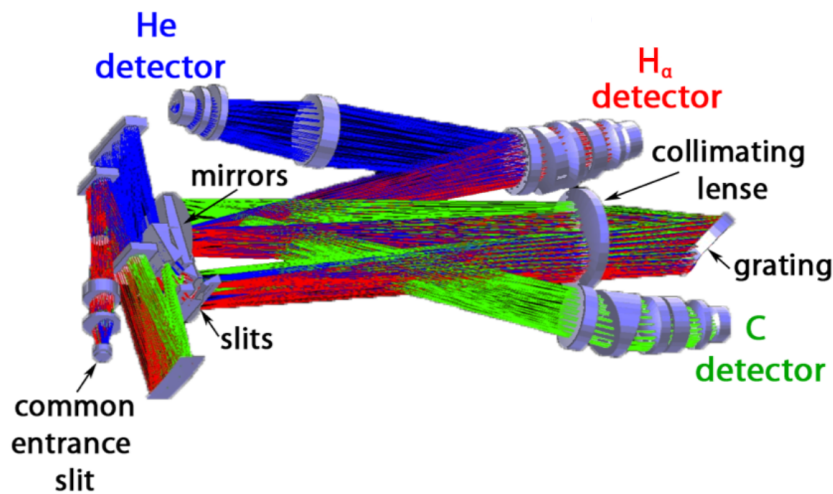


Figure 3.12: Drawing of the ILS spectrometer design, with the 3 different spectrometers inbuilt marked with different colors, adapted from [59].

spectrometer at the entrance slit and is then split into 3 disjoint wavelength ranges in the visible spectrum (blue for helium, green for carbon, and red for hydrogen line radiation measurements), providing spectroscopic information on different impurity species and the main ions [58, 57]. The light in the red and green wavelength ranges are observed with two sCMOS cameras (marked as H_α and C detector in figure 3.12) and will be further discussed in the following. The helium observation (He detector-blue) is measured with a

CCD camera and has no relevance for the thesis, but could be used to study fusion reaction born He content and their transport in the future [60, 61].

3.5.1 ILS-Green – Carbon-impurity spectroscopy

For the observation of the carbon radiation (C detector in figure 3.12), the sCMOS camera can achieve short integration times around 7.5 ms due to its fast readout speed. Not fully ionized and excited carbon can be found in the low-temperature edge of the plasma, and the plasma core due to CX reactions between fully ionized carbon atoms and the active NBI injection. Because of it, the observed light is a combination of the low temperature edge contribution (characterised with low Doppler broadening) and a warmer (and thus wider) confined plasma contribution. These two contributions are often referred to as passive and active spectra. A typical C^{VI} line measurement is shown in figure 3.13, with the fitted passive (narrow) radiation in blue and active (broader) component in red. As the

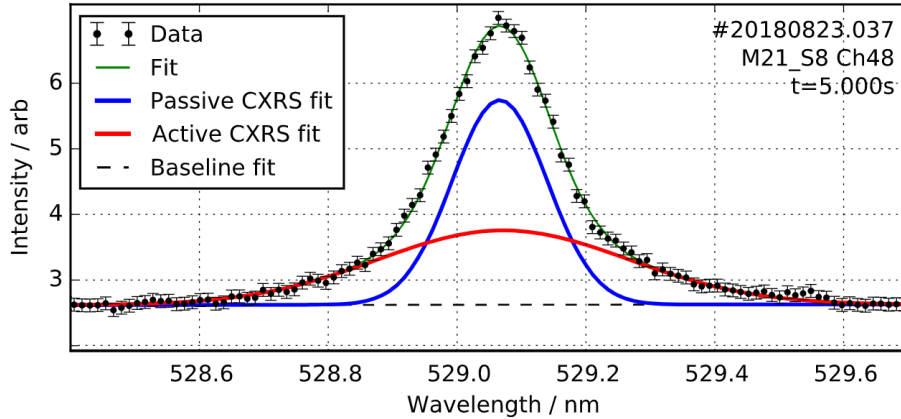


Figure 3.13: Typical C^{VI} line measurement during NBI operation with the ILS-Green spectrometer in discharge 20180923.037 from [57].

beam-carbon interaction provides a localised light source, from the Doppler-broadening of the active line emission, the local temperature T can be obtained:

$$T_A = E_A \frac{\sigma^2}{\lambda_0} \quad (3.6)$$

Here E_A is the rest energy of impurity A, σ is the spectral width expressed as a standard deviation and λ_0 is the unperturbed wavelength of the line emission. In addition, the plasma velocity parallel to a given observation line of sight, \vec{e} , can be inferred from the

Doppler-shift:

$$\vec{v}_n \cdot \vec{e} = c \frac{\Delta\lambda}{\lambda_0} \quad (3.7)$$

$\Delta\lambda$ is the Doppler shift of the observed line, relative to its unperturbed wavelength, λ_0 , and c is the speed of light. A typical carbon temperature profile derived from the observed line emission broadening is shown in figure 3.14.

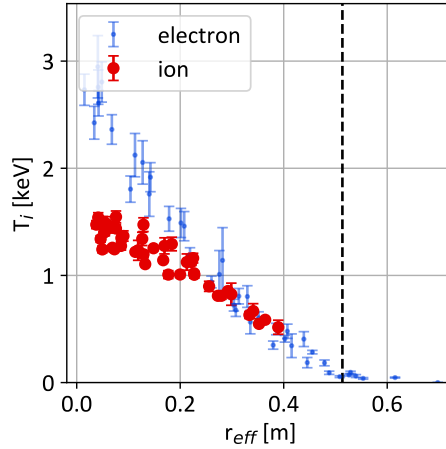


Figure 3.14: Carbon ion temperature profile marked with red, and the previously introduced Thomson scattering measured electron temperature profile with blue measurement for reference during NBI operation with the ILS-Green spectrometer in discharge 20180923.037.

Reconstruction of the net parallel and perpendicular flows in W7-X is not routinely available yet. In the few discharges investigated in detail, it was found that the plasma flow velocity is lower than 10 km/s with Doppler-shifts $\Delta\lambda < 15$ pm, which corresponds to less than 1 pixel on the camera change in the peak location of the carbon emission [62]. Because of it in the following, we will neglect the possible effects of the plasma flow.

In a typical discharge of the W7-X stellarator, the electron temperature is significantly higher in the plasma core than the ion temperature due to exclusive heating of the electrons by ECRH. Ion temperature profiles are observed to be clamped at 1.5 keV due to turbulence and insufficient ion heating [63].

3.5.2 ILS-Red – Balmer-alpha spectroscopy

One spectrometer of the ILS system measures the wavelength range between 648 nm and 666 nm with 0.0125 nm spectral and 16 ms typical time resolution on a sCMOS camera.

It resolves the H_α ($n = 3 \rightarrow 2$) transition at $\lambda_0 = 656.281$ nm of hydrogen species (marked as H_α in figure 3.12 with red). It provides information on the main ion species and made possible the analysis described in this thesis.

A measured spectrum is shown in figure 3.15 before beam operation and during NBI operation (in red and green), naming the different contributions of it. Assumed, FIDA emission shape is depicted with blue dashed curve for clarification purposes. Before NBI

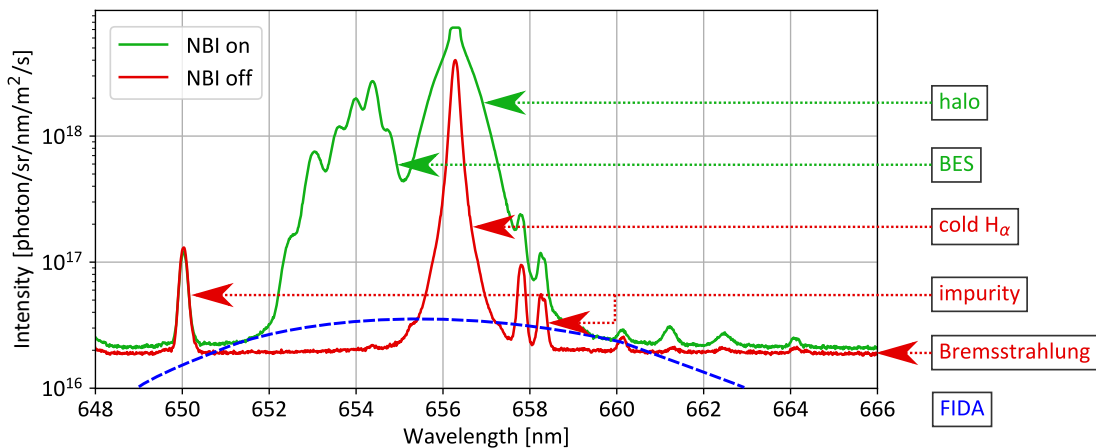


Figure 3.15: Example Balmer-alpha spectrum measured by the ILS Red spectrometer at W7-X. The observed spectrum consists of spectral components produced by different neutral hydrogen populations as well as not fully ionized impurity populations.

operation we can see a narrow, high intensity peak around λ_0 , 656.28 nm. This emission is Balmer alpha radiation from cold neutrals in the plasma edge region, getting excited by electron impact excitation or charge exchange reactions. Multiple other narrow line radiation peaks can be observed as well identified as intrinsic impurities such as oxygen and carbon lines which are present in the low temperature edge of the plasma. The whole emission sits on a continuous background, produced by the charged particles' Bremsstrahlung emission. The measured Bremsstrahlung emission can be expressed in the units of photons/(sr nm m² s) using local plasma parameters and the observed emission can be obtained

by integrating it along the observation direction:

$$I(\lambda) = 7.57 \times 10^{-30} \frac{1}{\lambda} \int g \frac{n_e^2 Z_{eff}}{T_e^{1/2}} e^{-hc/\lambda T_e} dl \quad (3.8)$$

where λ is the wavelength in m, n_e is the electron density in m^{-3} , and T_e is the local electron temperature in eV, Z_{eff} is the effective charge of the plasma:

$$Z_{eff} = \frac{\sum_i Z_i^2 n_i}{\sum_i Z_i n_i} \quad (3.9)$$

summing over all the different ions with charge Z_i and density n_i in the plasma. h is the Planck constant in eV/s and c is the speed of light in m/s. The g Gaunt factor depends weakly on T_e and Z_{eff} , and in the order of unity:

$$g = 5.542 - (3.108 - \ln(T_e/1000)) (0.6905 - 0.1323/Z_{eff}) \quad (3.10)$$

Compared to the red curve, when the NBI turns on, multiple other peaks appear, shown in green. A well localised spectral feature produced by excitation of the NBI neutrals called the beam emission spectrum (BES), is produced at high Doppler shifts (in the range of 652-655 nm). This group of numerous peaks correspond to the 2 different operated beams, each having full, half and third energy components producing different characteristic Doppler shifts. On top of it, the otherwise degenerate $n = 3 \rightarrow 2$ transition is further split as particles experience strong electric fields due to the Lorentz transform $\vec{v} \times \vec{B}$ of the magnetic field. Details of the splitting will be further discussed in the next chapter. A broader feature appears around λ_0 due to excitation of the beam halo neutrals, a population created by thermal ions being neutralized by the beam neutrals via the CX reaction. Besides these dominant features, the fast-ion Balmer-alpha emission (FIDA) is 4 orders of magnitude lower in peak intensity than any other spectra contribution we discussed so far and has the broadest spectral feature. As mentioned in the introduction, this thesis work focuses on the interpretation of this emission.

3.5.3 Calibration of the ILS-Red spectrometer

For the proposed FIDA measurements, detailed intensity and wavelength calibrations are of particular importance. The spectral shape of the FIDA emission, i.e. the Doppler-shift

and Doppler broadening, contains information on fast-ion energies and their pitches and the measured intensities can be related to the fast-ion density.

Wavelength calibration and instrument function of ILS-Red

For the wavelength calibration of the ILS spectrometer, a neon lamp was used which emits three characteristic NeI spectral lines in the observed wavelength range: 650.65 nm, 653.29 nm and 659.90 nm. During the calibration measurement, first all odd and later all even channels (every second channel) were illuminated for 15 minutes, providing excellent signal to noise ratio. A typical averaged spectrum is depicted in figure 3.16 a). The three neon line

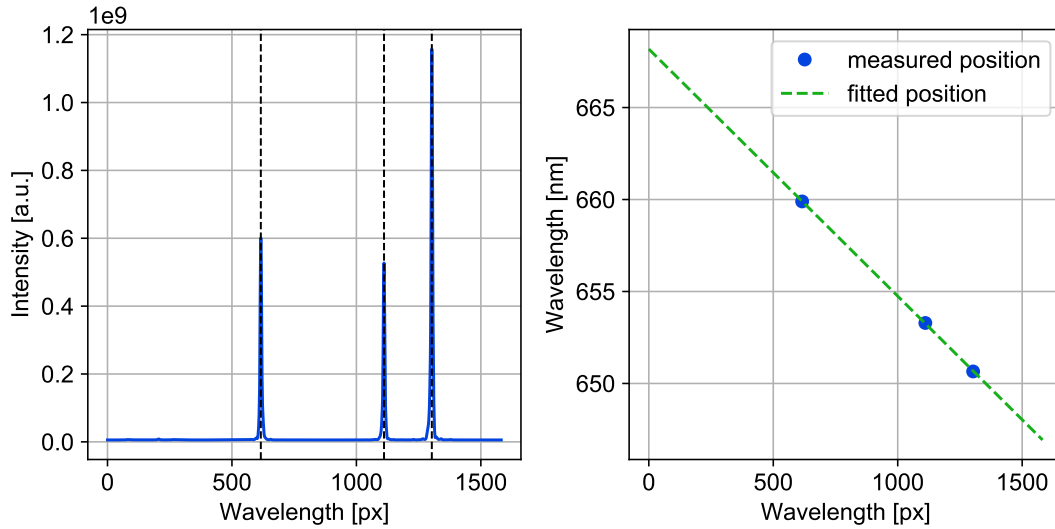


Figure 3.16: Wavelength calibration measured spectrum of the first spatial channel on the camera sensor.

radiation peaks are clearly visible and their peak positions are marked with black dashed lines. Using their pixel position and known emission wavelength, the pixel-wavelength connection can be made.

Moreover, the instrumental function of the spectrometer system can be inferred from the neon calibration measurements. As the neon lamp measurement was carried out at room temperature and in the absence of any strong magnetic fields, it does not suffer any significant broadening and a Dirac-delta line emission might be expected. However, the finite width of the entrance slit and the different optical elements in the spectrometer cause a finite spectral broadening, as shown in figure 3.17 b). The FWHM of the instrumental

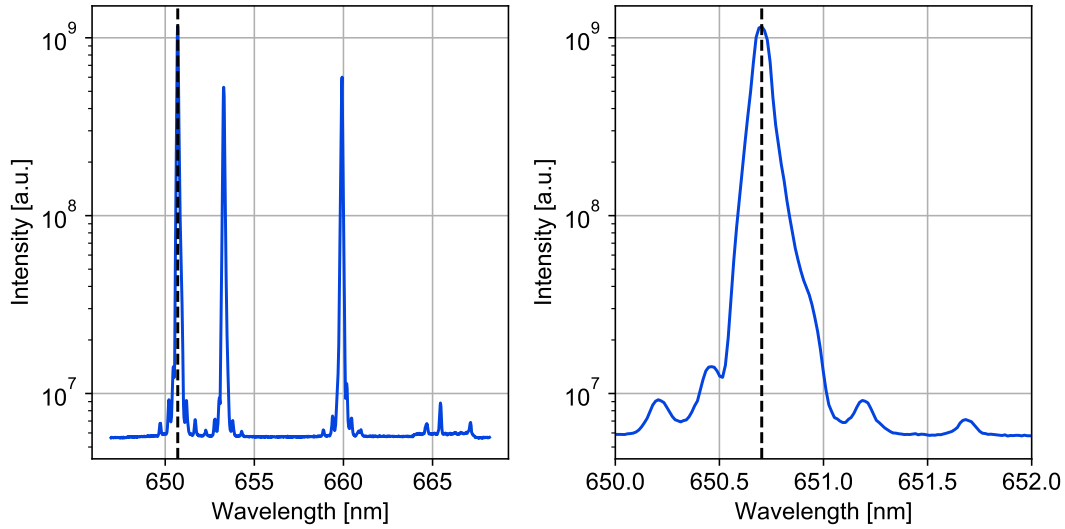


Figure 3.17: Natural spectral shape and broadening of the neon lines. Interference patterns due to the complex optical setup of the spectrometer can be observed.

function is around 0.1 nm and relatively wide spectral wings of up to 1 nm can be identified. Outside this range, however, only readout noise is observed. This well defined instrumental function is essential for FIDA measurements because otherwise, the edge Balmer-alpha radiation, which is approximately two orders of magnitude more intense, might contribute to the spectral range at which FIDA radiation is studied. This could contaminate the measurement and would be unacceptable. It is therefore important to have confirmed that the instrumental function of the ILS-Red spectrometer is well defined such that FIDA measurements are feasible.

Binning on the spectrometer

As introduced in section 3.5, all the collected light from the plasma is being guided to an area of 1952×1584 pixels on the sCMOS sensor. Figure 3.18 shows measured data for single time frame before and during NBI operation. Before NBI (figure 3.18 a), we can see that the brightest line is the cold Balmer-alpha emission, being aligned for all of the lines of sight in the center of the chip (around 900 pixels [px] along the horizontal axis). Note that the 52 fibers (channels) connected to the spectrometer are stacked vertically. Hence, 52 channels can be identified in the vertical direction on the CMOS detector. The peak intensities change as a function of channel number, as different lines of sight measure

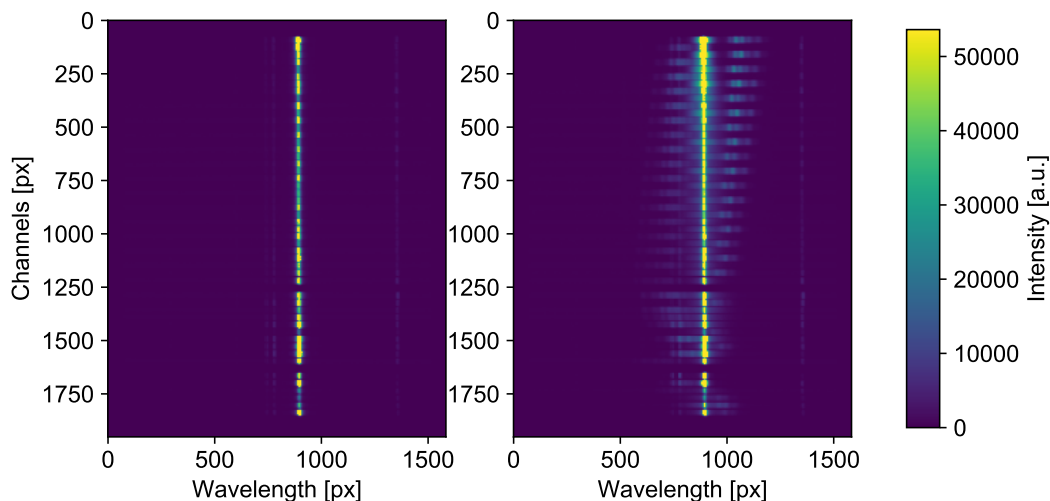


Figure 3.18: Raw image on the ILS-red spectrometer a) before and b) during NBI operation.

different light intensities. In figure 3.18 b) additional emission arises next to the cold Balmer alpha line when the NBI turns on. This additional light corresponds to the BES emission and appears red- and blue shifted on consecutive channels as the M21 and T21 have been interlaced with the A21 channels.

Straight binning

In the original analysis mode of the camera data, straight stripes were selected to represent individual channels. Their measured intensity was integrated along the y direction. It was found in this work that this led to significant cross-talk between the different channel due to slight rotational misalignment of the chip. While this cross-talk was negligible for analysis of the other, far stronger spectral components, it is critical for FIDA analysis. This observation can be made more visible by illuminating fibers of the channels one-by-one which is depicted in figure 3.19 a), where the dashed white lines mark the assumed boundary of a single channel. The cross-talk happens at the edges of the detector which corresponds to high Doppler shifts at which we would anticipate significant FIDA emission. As the BES typically has high Doppler shifts too, the interlacing arrangement of it leads to contamination of neighbouring channels FIDA emission.

In order to correct for the above introduced low level cross-talk between neighbouring channels, tilted bins were selected. To set it up, the single fiber illumination data was

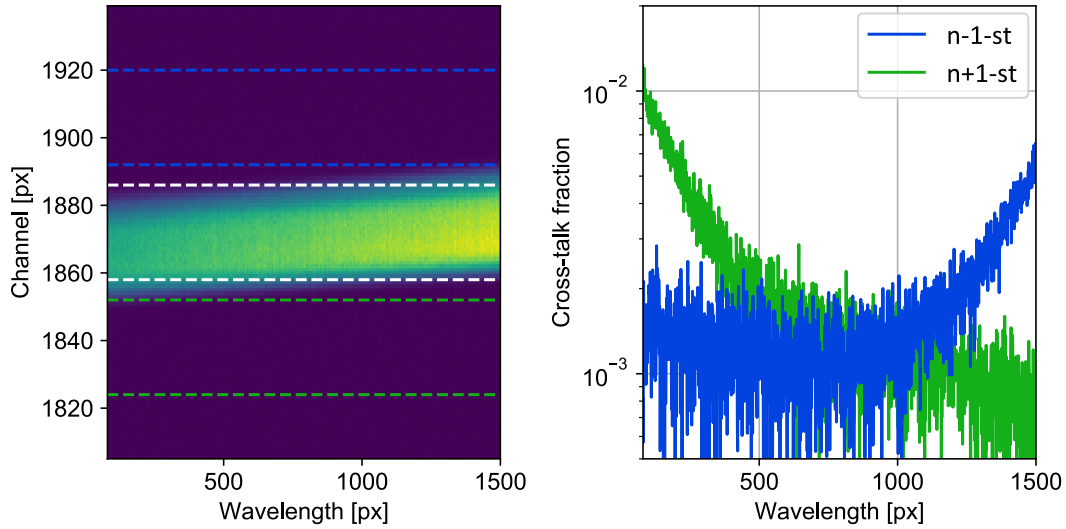


Figure 3.19: a) Channel allocation with straight binning, the selected channel's boundary is marked with white dashed line, neighbouring ones with blue and green. b) cross-talk of the central channel's signal into neighbouring ones.

used again. For each and every channel at 100 and 1500 px (along the wavelength x axis) the intensities of the illuminated channel were investigated, as depicted in figure 3.20 a), marked with red and blue dashed lines. Channel pixels (y axis) where the intensity was higher than 40% of the maximum were selected and are marked as the region between dashed lines in figure 3.20 b). Out of the multiple points, the middle one was selected to represent the center of the channel as depicted in figure 3.20 a) with white dashed line. The same calculation was carried out for all the channels where the illumination was available, selecting the middle of the channels. The channel-width was chosen ± 10 px from the central line, which provided sufficient light, and low cross-talk levels. With this setup channels were assigned, and the neighbouring cross talk levels could be calculated again, as depicted in figure 3.21. The cross talk of given channel could be reduced below 0.1%, which is an order of magnitude better than with the straight binning. Given that the beam-emission is typically about a factor of 100 larger than the FIDA emission, this level of cross-talk will impact the FIDA measurement by maximum 10% which appears to be acceptable.

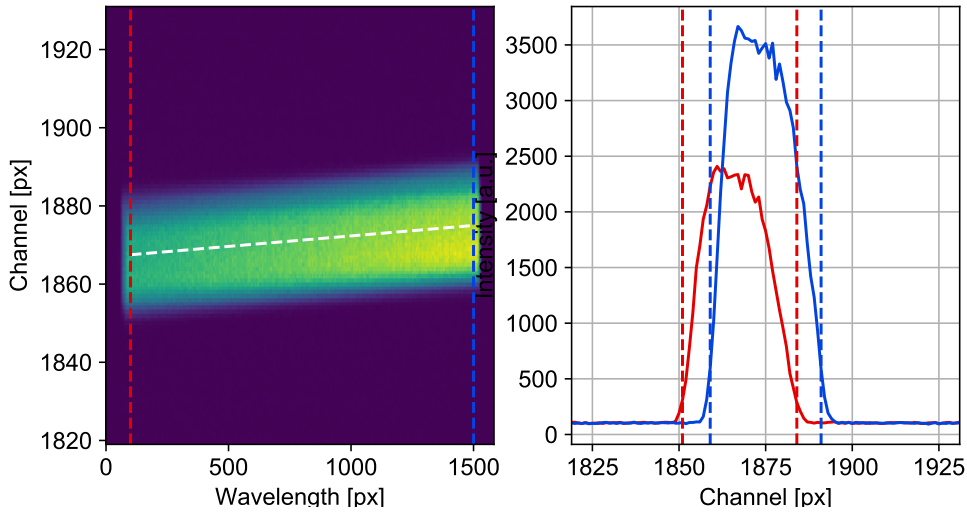


Figure 3.20: a) Central line of a single channel, marked with white dashed line. b) Intensity profile at $x=100$ px colored red and at $x=1500$ px colored blue.

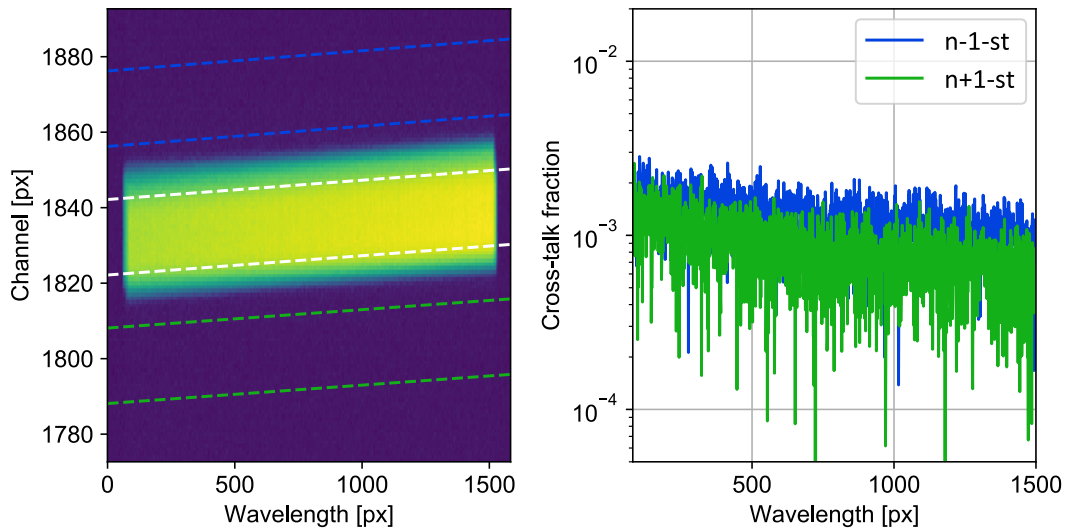


Figure 3.21: a) Channel allocation with tilted binning, the selected channel's boundary is marked with white dashed line, neighbouring ones with blue and green. b) cross-talk of the central channel's signal into neighbouring ones.

Intensity calibration

An Ulbricht calibration sphere was positioned and moved in front of the light collection optics inside of the W7-X vacuum chamber. Due to the movement, each line of sight ob-

tained the full light flux for a couple of seconds while the sCMOS camera was continuously recording the spectrum, which is shown in figure 3.22 a). Then the time points corresponding to the full illumination of a given channel were selected (defined as at least 80% of the measured maximal intensity), as depicted in figure 3.22 b). Then in figure 3.22 c) it is

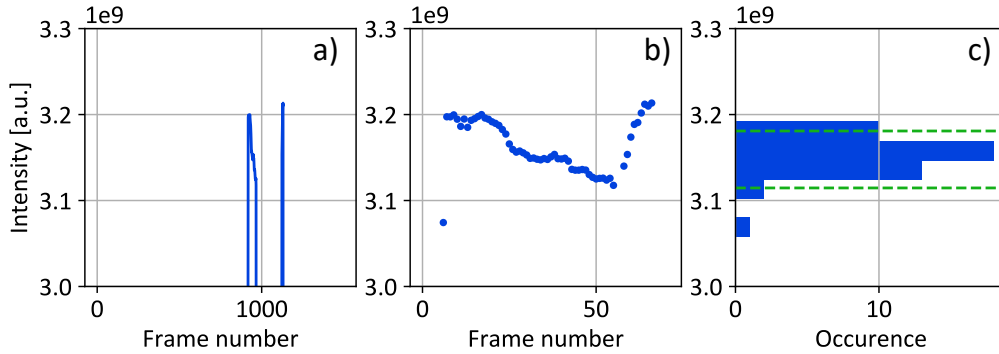


Figure 3.22: a) measured integrated intensity for channel 2 during calibration. b) Selected time-points where the intensity exceeded 80% of the maximum. c) Distribution of the measured intensities, where the selection range is drawn with green dashed line.

shown that the measured intensity varies but the distribution of it is unimodal. To the histogram a Gaussian curve was fitted, and time points were selected, where the measured intensity fell in the 2σ range around its expected value (marked with green dashed line in figure 3.22 c)). Using these time-points an average measured spectrum was calculated. As the spectral intensity of the calibration sphere is known, as it was produced by the Professional Standards Institute, (it is depicted in figure 3.23 b) as the function of wavelength) dividing it by the measured spectrum results in the intensity calibration factor. This pixel dependent factor can then be multiplied with the experimental data obtained during plasma experiments in order to obtain absolutely calibrated measurements.

With the above described calibrations and corrections, a sufficient quality of the measured spectra is achieved to be compared to simulations.

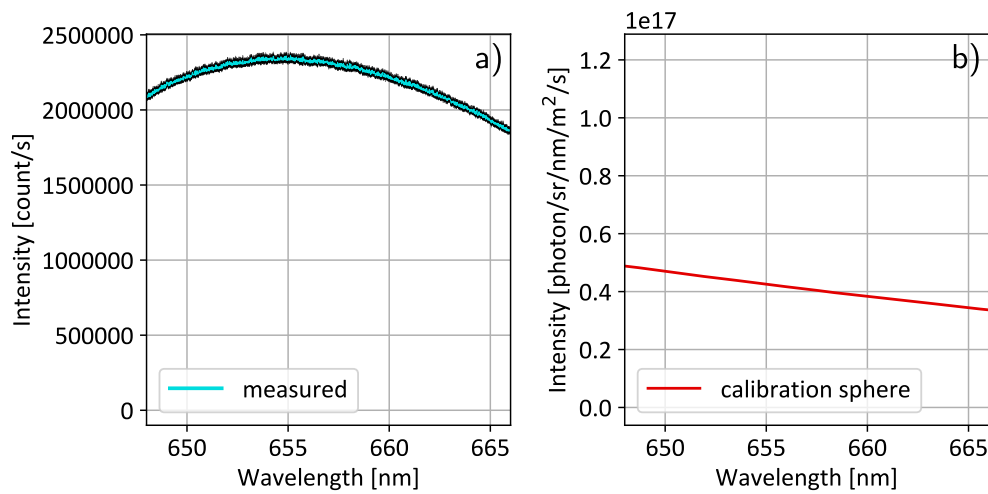


Figure 3.23: a) measured spectrum during calibration by the ILS-Red spectrometer. The selected spectra are plotted with black, their average is depicted with light blue color. b) Calibration sphere intensity curve as provided by the manufacturer.

Chapter 4

FIDASIM modelling for W7-X

FIDASIM calculates the local, excited state-resolved densities of different neutral hydrogen populations, and predicts their spectral emissions. In the following, the inputs and numerical approach of FIDASIM will be discussed.

4.1 Collisional radiative model

The main core routine of FIDASIM solves the collisional radiative (CR) model of the local, state resolved neutral density for a given set of plasma parameters which can be formalised with the following equation:

$$\frac{d\vec{\rho}}{dt} = \underline{\underline{M}}\vec{\rho} \quad \vec{\rho}(0) = \vec{\rho}_0 \quad (4.1)$$

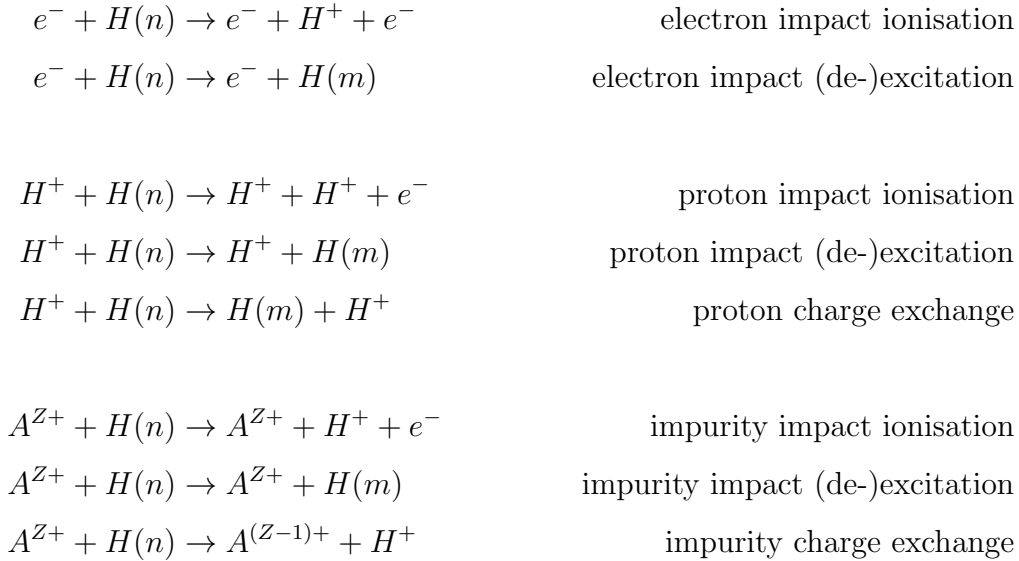
where $\vec{\rho}$ is the charge state resolved particle flux, containing various excited states (typically from the ground state to 6th excited state) and $\underline{\underline{M}}$ is the transition matrix, containing the atomic physics considered responsible for the change of this excited state. The transition matrix contains the collision-induced excitation, deexcitation and ionisation cross sections, as well as the spontaneous deexcitation process described by the Einstein coefficients. A specific matrix element M_{ij} can be constructed in the following way:

$$M_{ij} = n_e \langle \sigma v \rangle_{ij}^e + n_i \langle \sigma v \rangle_{ij}^i + n_Z \langle \sigma v \rangle_{ij}^Z + \epsilon_{ij} \quad (4.2)$$

where n marks the electron, ion and impurity density from left to right $\langle \sigma v \rangle_{ij}$ is the rate coefficient calculated assuming local thermal equilibrium of charged particles and ϵ_{ij} is the Einstein coefficient of the i - j transition. This constant coefficient linear differential equation system can be integrated and has an exact solution which can be expressed using the eigenvalues ($\{a_i\}_{i=0}^n$) and eigenvectors ($\{\vec{v}_i\}_{i=0}^n$) of $\underline{\underline{M}}$:

$$\vec{\rho}(t) = \sum_{i=1}^n c_i e^{a_i t} \vec{v}_i \quad (4.3)$$

In case of FIDASIM the first 6 excited states are followed ($n=6$). Any excitation-reaction leading to higher excited states is considered as an ionization event. The different atomic physics cross section are gathered from ADAS database and a publication from Janev [64], the following pair reactions are considered:



Since the main plasma wetted surface at W7-X is carbon, it is assumed to be the main impurity in the device and therefore it is the only impurity species considered in the simulation. By integrating the particle flux in time, the time spent in a simulation grid cell, and dividing by a given volume, local particle densities can be obtained. From these particle densities, the Balmer-alpha photon emission can be calculated by multiplying the density of the $n=3$ state with the Einstein coefficients for spontaneous deexcitation of the $n = 3 \rightarrow 2$ transition.

4.2 Spectral predictions

The above discussed CR model estimates a local state-resolved hydrogen density, and consecutively a local photon emission of a specific neutral population in the simulation volume, which FIDASIM then can integrate using a diagnostic line of sight description in order to produce a synthetic Balmer-alpha spectrum. The Doppler shift of the photon emitted with wavelength λ_0 can be calculated by taking the projection of the emitter's velocity \vec{v}_n to the specific line of sight direction vector \vec{e} :

$$\Delta\lambda = \lambda_0 \frac{\vec{v}_n \cdot \vec{e}}{c} \quad (4.4)$$

Stark splitting appears in addition to the Doppler shift as the emitting particle experiences an electric field ($\vec{E} = \vec{v}_n \times \vec{B}$) in its reference frame. The $\vec{v}_n \times \vec{B}$ electric field causes the, otherwise degenerate, $n = 3 \rightarrow 2$ transition to split into 15 non-degenerate ones. The individual transitions can be grouped into emission lines with a linear polarization direction parallel to the local electric field and into emission lines with perpendicular or circular polarization. These lines are called π and σ - lines, respectively. The additional splitting can be expressed as follows:

$$\Delta\lambda_i^{SE} = A_i \lambda_0^2 |\vec{E}| \quad (4.5)$$

where A_i marks the energy difference, and thus wavelength shift, of the i -th non-degenerate transition. The observed relative intensity of the non-degenerate transitions can be expressed as follows:

$$I_{rel} = B_i \left(1 \pm \left(\frac{\vec{e} \cdot \vec{E}}{|\vec{E}|} \right)^2 \right) \quad (4.6)$$

where plus applies for σ lines and minus for π lines. The different coefficients are obtained from [65]. Illustration of the Stark splitting for the hydrogen $n = 3 \rightarrow 2$ transition is depicted in figure 4.1.

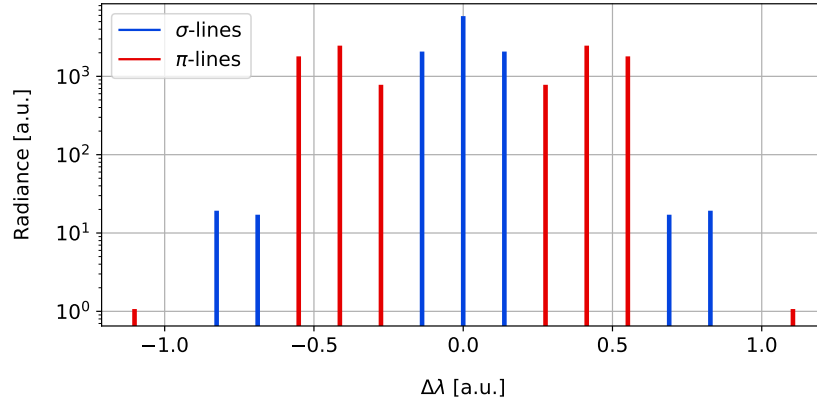


Figure 4.1: Illustration of the Stark splitting, and the split lines relative intensities in the presence of electric field. σ and π lines are marked blue and red respectively.

4.3 Simulation grid

FIDASIM works on a 3D Cartesian grid, aligned to the machine coordinate system, in which the CR model is applied, i.e. where the attenuation and light emission of excited neutrals is calculated. The boundaries of the simulation grid are typically set up to encapsulate not the whole machine, but at least the NBI injection path and the lines of sight within the confined region. Note here that the latter is necessary to give an appropriate estimation on the line integrated Bremsstrahlung radiation and passive FIDA emission. A typical grid setup for the simulation at W7-X is depicted in figure 4.2 from a top-down view of the device. The green rectangle marks the simulation domain, for reference, the two NBI sources are depicted with dashed lines. The three observation directions, A21, M21 and T21 are depicted with red, blue and orange solid lines. Flux surface contours in the midplane are plotted with black solid lines. While the grid size for simulations of the A21 toroidal observation needs to be substantial (the line of sight length in the plasma can reach up to 5-6 m), the necessary simulation grid for the M21 and T21 observation ports can be smaller: their path in the plasma is only around 1 m since the lines of sight do not cover a significant toroidal extent.

For each grid cell, the flux surface label (r_{eff}) is stored (see section 3.2). This is important since FIDASIM needs to consider the local plasma parameters when calculating the state resolved beam attenuation and excitation along the path of Monte Carlo (MC) markers. Since plasma profiles are input to the code on 1D flux coordinates (r_{eff}), mapping

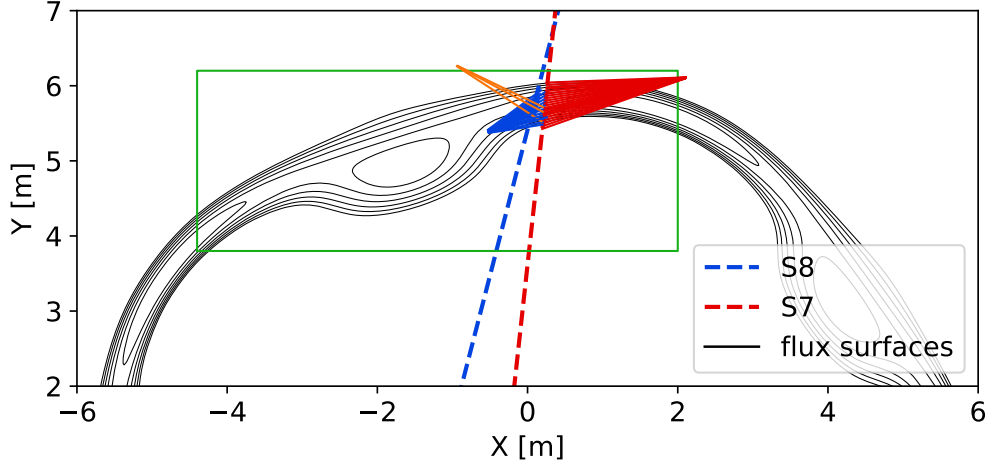


Figure 4.2: Setup of the simulation boundary marked with green in the top-down view of W7-X. The NBI sources are plotted with dashed lines, while the different observation directions with solid lines.

from the 3D real space coordinates to flux coordinates is required. The flux-surface label of a given (x,y,z) position inside the simulation grid is obtained by 3D trilinear interpolation and the local plasma parameters can then be determined by a 1D interpolation:

$$(x, y, z) \rightarrow (R, Z, \varphi) \xrightarrow[\text{VMEC}]{r_{eff}(R,Z,\varphi)} r_{eff}(x, y, z) \xrightarrow{n_e(r_{eff})} n_e(x, y, z)$$

4.4 Neutral density- and spectral predictions

In this section we discuss the simulation of specific spectral components in detail, including their characteristic spatial distribution and emission patterns .

4.4.1 Neutral beam injection parameters

In order to provide an accurate estimate of the local beam density assessment of the different parameters possibly influencing it must be done. The first stage of the simulations is the prediction of the active beam emission spectra by FIDASIM which involves the simulation of neutrals from NBI. Neutral markers, representing multiple real particles, are launched at the ion sources whose (x, y, z) coordinates are listed in table 4.1.

	x	y	z	u_x	u_y	u_z
S7	104.27	1317.11	90.67	-0.1085	-0.990	-0.085
S8	195.96	1300.37	90.67	-0.2486	-0.9648	-0.085

Table 4.1: Real space position (x, y, z) in cm and direction vectors (u_x, u_y, u_z) of sources S7 and S8 in Cartesian coordinates, as determined from its CAD design drawing and as used in FIDASIM.

To define the NBI vectors, a beam center-line aligned Cartesian coordinate system, (u, v, w) is used. Here u marks the NBI forward direction towards the plasma and is equal to the beam center line-vectors, as given in table 4.1. Moreover, v and w are the horizontal and vertical directions. Later in the simulation this system is rotated back to the real (x, y, z) Cartesian grid of the device.

Given the physical description of the ion source, (width, height) simulation particles are initialized at its rectangular surface uniformly distributed, which we denote as $(0, v_0, w_0)$. Then, a direction vector \vec{U} is being assigned, pointing towards the vertical and horizontal focal point but altered by the finite divergence δ of the beam. Schematics of this approach

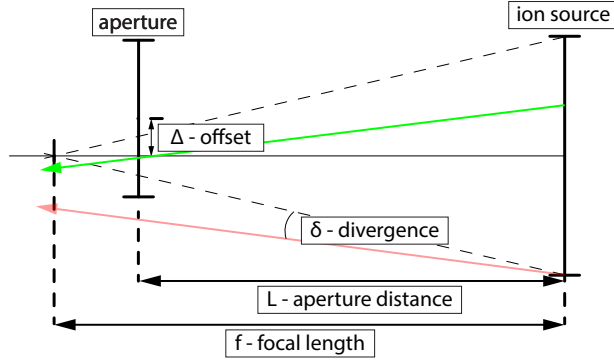


Figure 4.3: Schematics of the neutral beam injection in a vertical cross-section used in FIDASIM. Markers are initialized at the ion-source position, and assigned a propagation direction.

are depicted in figure 4.3 and can be expressed in the following form:

$$\vec{U} = \begin{bmatrix} u \\ v \\ w \end{bmatrix} = \begin{bmatrix} -1 \\ v_0/f_h \\ w_0/f_v \end{bmatrix} + \begin{bmatrix} 0 \\ \tan(\delta_h r_1) \\ \tan(\delta_v r_2) \end{bmatrix} \quad (4.7)$$

Here r_1 and r_2 are random numbers from a $\mathcal{N}(0, 1)$ normal distribution.

With the velocity vectors and start positions defined, the NBI apertures (beam blocking

elements) are considered, which in the case of W7-X are the front and rear cross sections of the beam duct. In FIDASIM, these apertures are approximated by rectangles. Their position and shape relative to the beams is depicted in figure 4.4 which shows a) a top-down and side view of the beam and duct and b) the aperture cross sections, together with the simplified rectangular shape as implemented in FIDASIM.

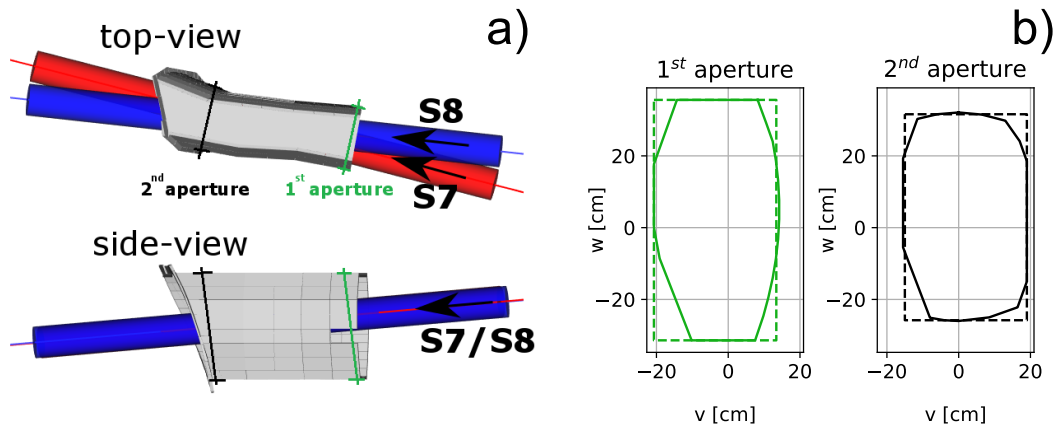


Figure 4.4: a) CAD drawing of the NBI beam ducts from a top and side view. The red and blue tubes are representing S7 and S8 respectively. The positions of the apertures are marked with light green and black. For both sources the same cross section is assumed to be the limiting element. b) the real cross sections of the apertures with solid line and as assumed in FIDASIM with dashed lines.

In case a given NBI ray is outside at least one of the two apertures, the ray is discarded in FIDASIM and a new ray is initialized, keeping the number of markers constant arriving to the plasma vessel. This procedure is depicted in figure 4.5 for S7 in the beam aligned coordinate system. Figure 4.5 a) provides a 3D view and figure 4.5 b) provides a top-down and a side view of the NBI rays. The apertures are colored in light green and black. Markers passing through both apertures are colored dark green, other ones are colored red.

The simulated beam density footprint on the v - w plane is plotted in figure 4.6 a) at $u = 710$ cm, near the entry to the plasma, from the ion source (along the beam center line) for source S7. For reference, the beam density contours without apertures are plotted with white at the same location. In figure 4.6 b) and c) the horizontal and vertical projections of the beam density are depicted, with black line for the case without apertures and with blue for the case with apertures. We can see that the apertures modify the shape of the

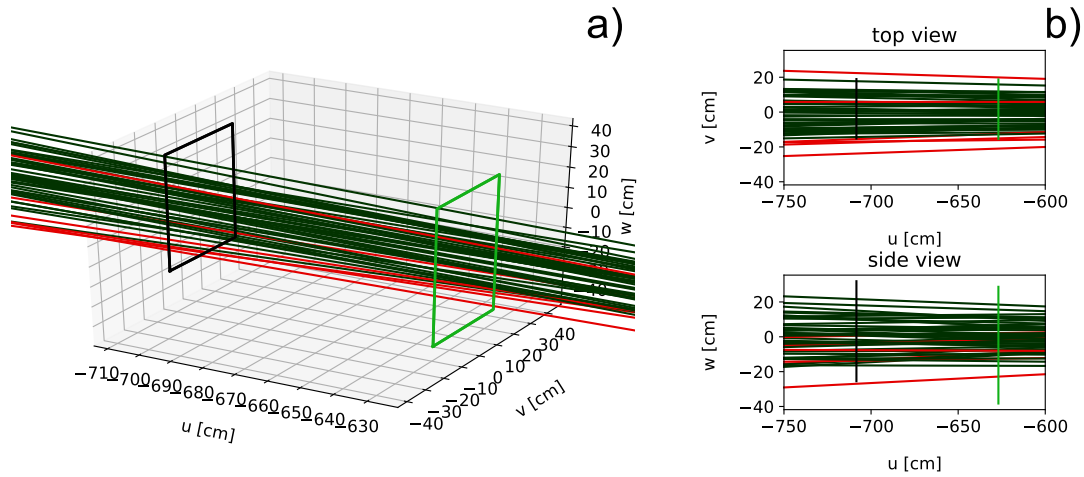


Figure 4.5: a) Simulation of 50 beam particle paths in FIDASIM in 3D, showing how two apertures (light green and black rectangles) scrape source S7. Markers travelling towards the plasma might have an initial position and direction which does not go through these openings (red lines). Passing markers are marked dark green. b) shows the top- and side view of the beam source simulation.

beam such that they limit the beam's horizontal extent to 40 cm, with a sharp fall off, while keeping its vertical shape intact. The above discussed parameters, ion source size,

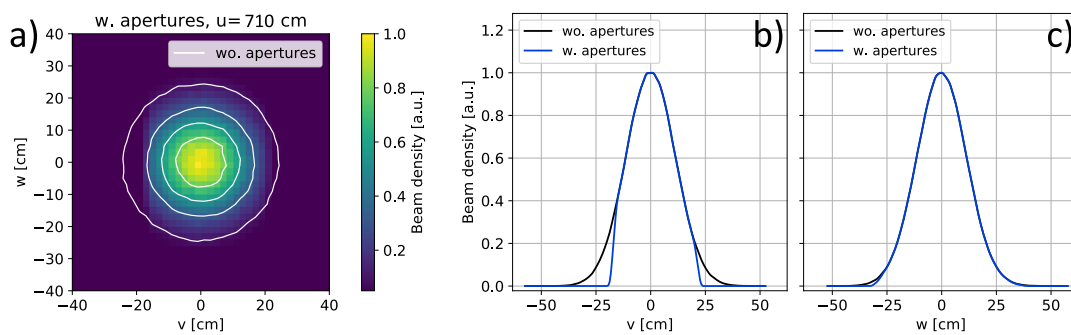


Figure 4.6: a) beam density footprint in the v - w plane with apertures for S7 $u = 710$ cm from the ion source (after passing through both apertures). The white contours mark how the beam footprint would look like in the same location without apertures. b) shows the marginal beam shapes in the v and w direction with (blue line) and without (black line) apertures.

divergence, focal length, aperture positions, sizes and offsets are collected in table 4.2

		D [cm]	δ [°]	f [cm]	$L_{1,2}$ [cm]	$\Delta_{1,2}$ [cm]	$d_{1,2}$ [cm]
S7	v	22.8	0.8	650.0	626.9 / 708.4	1.7 / 1.9	34.1 / 34.1
	w	50.6	0.8	700.0		-4.8 / 3.2	67.0 / 57.4
S8	v	22.8	0.8	650.0	626.9 / 708.4	5.6 / -5.9	34.1 / 34.1
	w	50.6	0.8	700.0		-4.8 / 3.2	67.0 / 57.4

Table 4.2: Beamline parameters of sources S7 and S8, as used in FIDASIM. FIDASIM differentiates between horizontal and vertical parameters (with respect to the specific injection line's direction). D - size of the ion-source, where NBI markers are initialized; δ - beamlet divergence; f- focal length; L - distance of the first- and second aperture (beam blocking element) from the source; Δ - offset of the apertures' middle from the beam line; d - physical size of the apertures.

4.4.2 Beam- attenuation and emission

Each initialized NBI particle MC super marker (representing multiple real particles) gets, in addition to the propagation direction, kinetic energy assigned, depending on the injection voltage and the beam species composition (fraction of full, half and third energy component). The weight of the markers, i.e. the number of real particles being represented, can be calculated by dividing the injection power with the average energy per super marker and by the number of markers. Moreover, it is assumed that all the injected neutrals are initially in the ground state. Along the marker's path through the 3D simulation grid, the CR model is then applied and the local beam density is estimated in the relevant cells of the simulation grid.

The predicted neutral density is used then to predict the Blamer-alpha beam emission for each energy component, as depicted in figure 4.10 with different shades of blue, for a 2 source operation case. The figure shows that the different energy components have different characteristic Doppler-shifts. Note here that the beam emission is shifted significantly away from the unshifted Balmer-alpha line, marked with a black dashed line. Within one energy component, we can see the multiple peaks corresponding to the slightly different observation angle of S7 and S8 and the further splitting due to the Stark-effect.

4.4.3 Halo- neutrals and emission

The simulation of halo neutrals is divided into two parts. Using the previously calculated local neutral beam densities, the local ion density and the cross-section for charge exchange, the rate of born direct charge-exchange (DCX) neutrals can be calculated in each grid cell. Super markers representing DCX neutrals can then be started with randomized velocity

vectors that represent a local Maxwellian distribution (similarly as it was done for the beam markers). The markers are then followed through the simulation grid and the CR model is applied. Then the halo generation process is repeated, where the (n-1)th generation provides the donor neutrals for the n-th generation until the n-th generation's halo neutral density reaches less than 1% of the initial DCX halo density. As the halo formation can be considered as a random walk its spatial extent will be wider (dependent on the velocity of the local ions) than for the NBI. This is depicted in figure 4.7, where we can see that the predicted halo density is in the same order of magnitude as the beam density (both integrated in charge state and along the z axis). We can observe, that the halo density is slightly wider than the beam density as expected too.

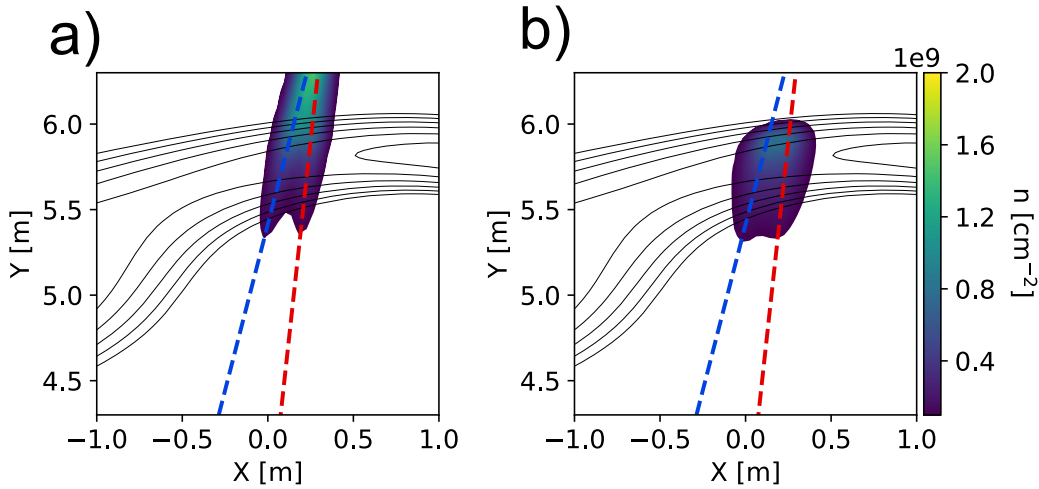


Figure 4.7: Integrated (along the z direction) a) beam- and b) halo density produced by S7 and S8 with identical colorscale.

The halo emission, as its source is thermal particles, is characterised by low Doppler-shift and is depicted with red color in figure 4.10. We can see that, due to the assumed zero rotation, the peak of the halo emission coincides with the unshifted Balmer-alpha line.

4.4.4 FIDA emission predictions

The neutrals introduced by NBI injection, as well as the halo neutrals surrounding the NBI provide donors for charge-exchange reactions with fast-ions, producing active FIDA light. Moreover, passive FIDA light arises from charge exchange reactions with the population

of background neutrals, discussed earlier in section 2.3. Background neutrals are mainly located in the plasma periphery and provide a source of non-localized FIDA radiation. The process of fast-ions being neutralized by charge exchange with NBI and halo neutrals and with background neutrals, is plotted in figures 4.8 a) and 4.8 b), respectively.

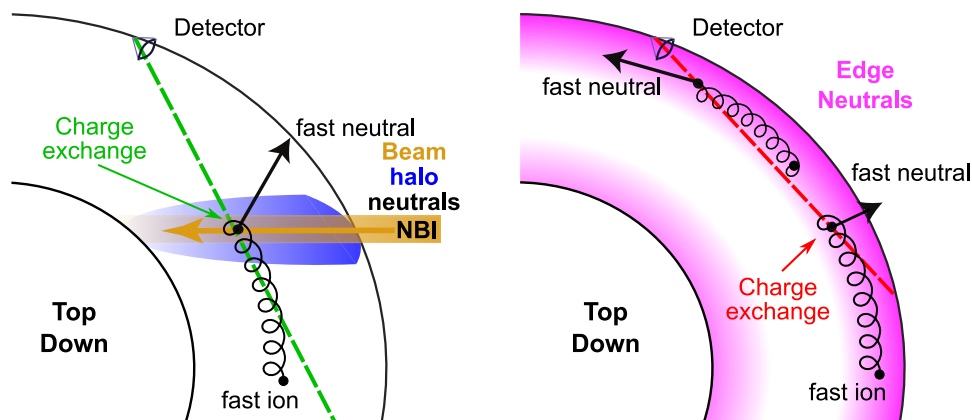


Figure 4.8: Toroidal cross-section of a stellarator, a top-down view. In figure a) the active- and figure b) the passive FIDA emission schematic is depicted. While the active FIDA is produced as the interaction of the active source of neutrals (NBI and halo) and fast ions, the passive emission is the result of the background neutral population and fast-ions.

To predict the shape and intensity of the FIDA emission, the shape of the underlying fast-ion distribution function is required. In the scope of this thesis 5D, $(R, Z, \varphi, \Lambda, E)$ dependent distribution functions are provided by the ASCOT4 code introduced in section 2.2.2. A representative distribution function with a centrally peaked fast ion density is depicted in figure 4.9.

In FIDASIM the simulation of FIDA emission starts with the calculation of the CX reactions of fast ions per cell, which is proportional to the local fast ion density times the local neutral density. Based on the input fast-ion distribution function, representative velocity vectors are sampled in a given grid cell and their start positions are corrected for the fast particles Larmor radius. Then the CR model is applied for the fast neutrals and the FIDA neutral density is calculated. The predicted emission is depicted in figure 4.10 with green. We can see a wide spectral feature, with a 2 orders of magnitude lower radiance than any other active component.

The $n = 3 \rightarrow 2$ transition has a finite natural lifetime in the order of few ns, being enhanced by collisional deexcitation (see figure 4.11). Hence, particles can travel a few centimeters between the charge exchange and the emission locations. This means that the

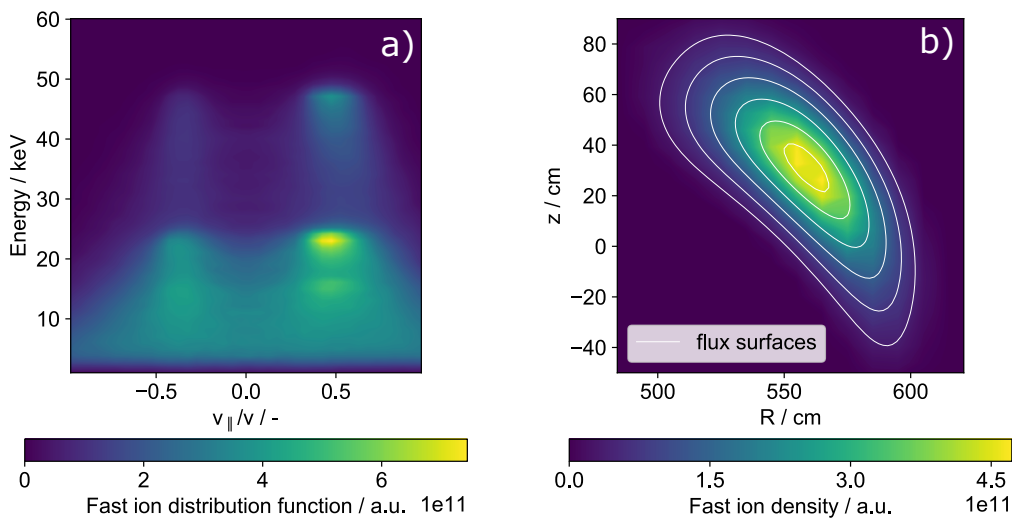


Figure 4.9: ASCOT predicted fast-ions. a) Distribution function in the beam-injection plane, averaged over the injection poloidal cross-section, and b) total fast-ion density in the poloidal cross-section.

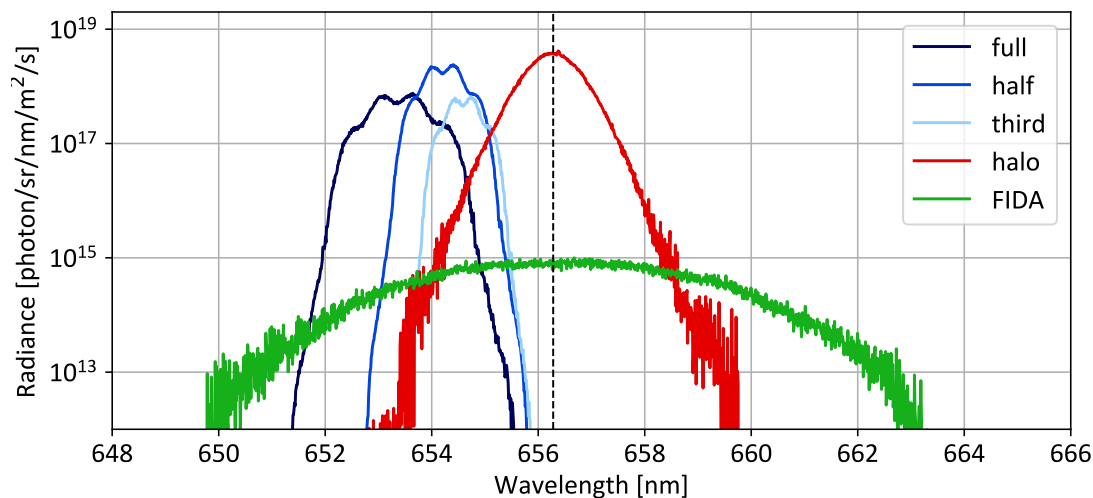


Figure 4.10: Typical active Balmer-alpha spectrum predicted by FIDASIM. Different colors mark different characteristic spectral components from the above described neutral populations.

origin of FIDA light is slightly smeared out compared to the beam emission [57] or the halo emission. This effect is usually smaller than smearing due to the line integration, which is due to the finite diameter of the beam around 20 cm.

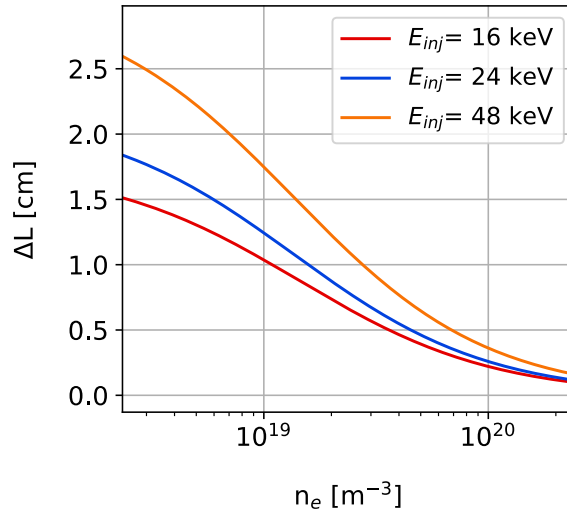


Figure 4.11: Fast neutral travelling distance in a slab geometry with constant plasma profiles (assuming $T_e = T_i$) to estimate spatial smearing of the $n = 3$ state.

4.5 FIDA weight function calculations

To characterise the fast-ion phase space sensitivity of different lines of sight, weight function calculations can be applied [16, 66, 67]. For a given LOS the observed $I(\lambda)$ FIDA emission can be expressed as a weighted integral of the $f(E, \Lambda)$ fast ion distribution function:

$$I(\lambda) = \iint W_\lambda(E, \Lambda) \circ \hat{f}(E, \Lambda) dE d\Lambda \quad (4.8)$$

Here, $W_\lambda(E, \Lambda)$ is the so-called velocity space weight function. A weight function can be considered as the probability of a single fast-ion with energy E and pitch Λ to become neutralized and subsequently emit a photon, observed at a given wavelength λ . To calculate weight functions, one can therefore sample through the velocity space of fast ions and calculate the wavelength at which a given fast ion would emit. By this method, one can construct a map of energy and pitch values that would provide emission at a given wavelength range, i.e. the velocity space weight function.

Note that this approach assumes that the FIDA light is localized at the intersection between NBI and a given line of sight. To take into account line integration effects, beam density weighted average quantities $\bar{\alpha}$ of all relevant parameters α , such as density,

temperature and the fast-ion distribution function are used:

$$\bar{\alpha} = \frac{\int \alpha (n_{beam} + n_{halo}) dl}{\int (n_{beam} + n_{halo}) dl} \quad (4.9)$$

The shape of the obtained weight functions mainly defined by relative alignment of the line of sight geometry and the magnetic field structure and as such, lines of sights from the same port have similar weight functions. They are often used to characterise the part of the velocity space addressable by the useful wavelength ranges available of a given set of lines of sight.

In the following the weight functions of the three different observation directions used at W7-X are presented and discussed. The weight functions were calculated for discharge 20180823.037 which was performed in the high mirror configuration and where kinetic profiles were presented earlier. They were prepared with 1 nm wide wavelength bins, using typical wavelength ranges where FIDA emission was observed in experiments. From each of the three ports, a core channel has been selected for illustrating the corresponding weight functions.

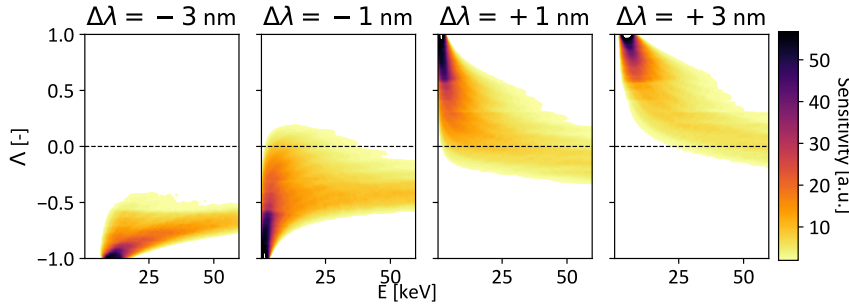


Figure 4.12: A21 port weight function for the blue- ($\Delta\lambda=-3$ nm and -1 nm) and red ($\Delta\lambda=+1$ nm and +3 nm) Doppler shifted side of the H_α line.

Figures 4.12-4.14 show weight functions for red-shifted (+3 nm) and blue shifted (-3 nm) FIDA radiation. As can be seen, the weight functions indicate highest sensitivities at energies between 15 keV and 30 keV which is close to half and third of the NBI injection energy (28 keV and 19 keV). Note that sensitivity to the full energy would require looking at higher Doppler shifts. From the weight functions, it also becomes clear that all three observation directions are sensitive to both co- ($v_{||} > 0$) and counter ($v_{||} < 0$) injection direction propagating fast-ions when looking at red and blue shifted radiation. However, it

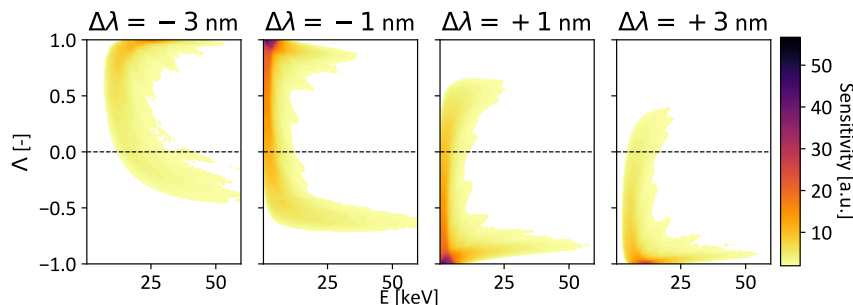


Figure 4.13: M21 port weight function for the blue- ($\Delta\lambda=-3$ nm and -1 nm) and red ($\Delta\lambda=+1$ nm and $+3$ nm) Doppler shifted side of the H_α line.

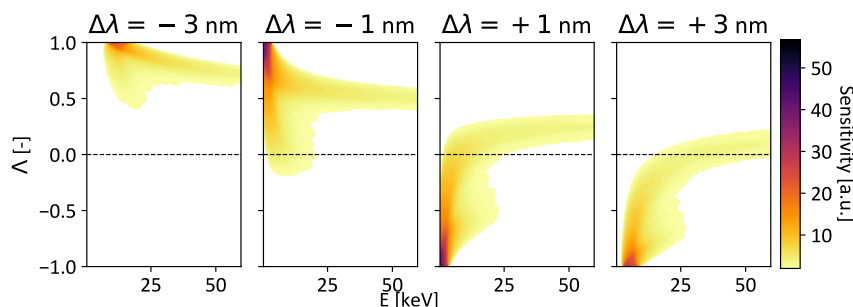


Figure 4.14: T21 port weight function for the blue- ($\Delta\lambda=-3$ nm and -1 nm) and red ($\Delta\lambda=+1$ nm and $+3$ nm) Doppler shifted side of the H_α line.

is noteworthy that only the T21 and M21 ports are sensitive to the deeply trapped particles with pitch values around 0. When studying the weight functions, it is important to consider the wavelength range accessible to study the FIDA radiation. In certain wavelength ranges (depending on the observation geometry), the beam emission might be superimposed which makes FIDA studies virtually impossible in these parts.

The W7-X active spectroscopy system was designed for good beam emission capabilities and to resolve the emission peaks coming from different beam energy components, high Doppler shifts for BES were preferred. With the current lines of sight available, different ports observe beam emission on either the blue- ($\Delta\lambda < 0$) or red shifted $\Delta\lambda > 0$ side of the spectra, where the observation of FIDA emission is strongly limited. From the point of FIDA emission it means that, one side of the spectrum will be always available for the observation of the fast-neutral's emission while the other, occupied by the BES will have only limited capabilities, these considerations combined with the weight functions' properties are summarized in the following table.

port	I_{BES}	$\partial_R(\Delta\lambda_{BES})$	$I_{FIDA}^{\Lambda < 0}$	$I_{FIDA}^{\Lambda > 0}$
A21	red	-	blue	red
M21	blue	+	red	blue
T21	red	-	blue	red

Table 4.3: Doppler-shifts of observed BES and FIDA emission from co- ($\Lambda > 0$) and counter ($\Lambda < 0$) beam injection direction particles. Red corresponds to positive and blue to negative Doppler-shift.

For completeness it is useful to note that in a few marginal cases, when the line of sight is close to perpendicular to the beam injection direction, resulting in low BES Doppler-shift, high Doppler-shift parts of the spectrum can still contain useful information on the fast-ion distribution. This happens in the plasma edge for A21 and T21 port, and in the plasma core for port M21.

Chapter 5

Validation of active beam-, halo- and FIDA emission modeling

As the adaptation of FIDASIM to 3D geometry and the W7-X stellarator was novel, carried out in the framework of this thesis, validation of the modeling was required. This chapter provides a direct comparison of the FIDASIM-predicted active beam-, halo- and FIDA emissions with the experimentally measured ILS-Red data which serves as validation in this context.

5.1 Prediction of active neutral populations

To validate FIDASIM, the predicted beam- and halo emission has been compared to the absolutely intensity calibrated measurements of the ILS-Red spectrometer. Moreover, the predicted injected power has been compared with beam power calorimetry measurements [52]. For this purpose, a representative discharge (#20180823.037), with both NBI sources operational was selected. This discharge was run in the high-mirror configuration, with 5 MW of continuous ECRH heating. Both NBI sources were turned on at 4.5 s and were operated for 1 s continuously. The beam injection power was 1.35 MW per source (as measured by the beam line calorimetry) and the acceleration voltage was 48 keV with neutral particle flux fractions of 0.32/0.61/0.07 (full/half/third) identical for both sources. The core plasma temperature was 2.5 keV for electrons and 1.5 keV for ions, with a core electron density of $6.2 \cdot 10^{19} \text{ m}^{-3}$. Fit to the measured kinetic profiles can be seen in figure 5.1 on the following page at 4.6 s. For the edge region ($\rho > 1$), profiles were

extrapolated assuming an exponential decay from the values at $\rho = 1$ point with a scale length of $\Delta L = 5$ cm which corresponds to $\Delta\rho \approx 0.1$ in units of the normalized minor radius. Radial electric field and toroidal rotation was assumed to be zero. Considering

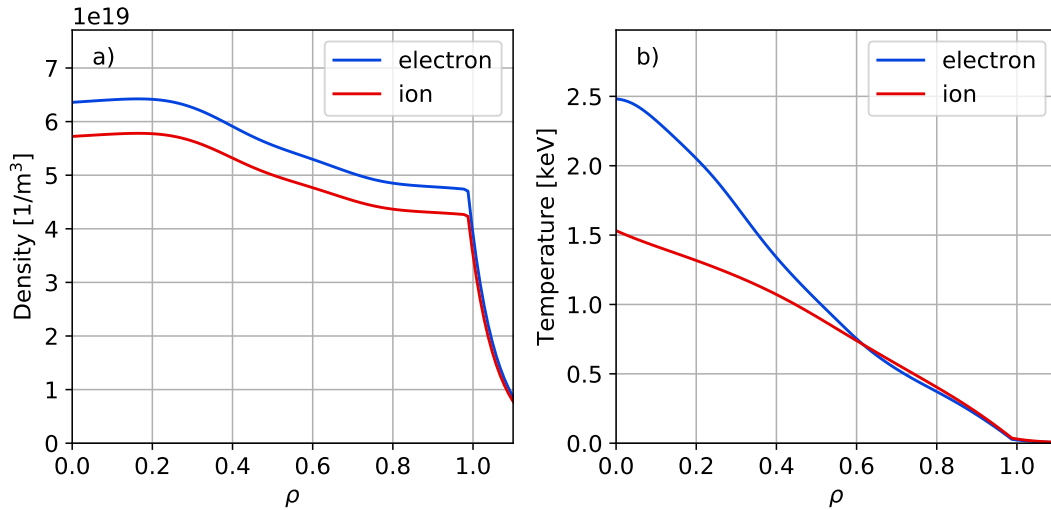


Figure 5.1: Kinetic profiles for discharge #20180823.037 at 4.6 s. a) density profiles, b) temperature profiles.

them would only change the Doppler shift of the different peaks, but not the intensity. Later we did not find any significant discrepancy of the peak positions confirming our assumption. The main impurity species was assumed to be carbon, with a flat $Z_{eff} = 1.5$ profile.

5.1.1 Beam modelling validation

With these inputs, the beam emission spectra were predicted for all of the available lines of sight from the three ports. Representative measured and predicted beam emission spectra for an edge and a core channel of each observation port are shown in figure 5.2. The blue lines represent the FIDASIM predictions of the beam emission, the measured active spectra after background subtraction and removal of the fitted Bremsstrahlung emission are given in black. The rows show the M21, A21 and T21 ports accordingly. The first column shows an edge channel, closer to the NBI source, and the second shows a core channel. Note that in the case of the T21 port there are no edge observations available. We can see that the observed emission decreases from the edge (first column) to the core

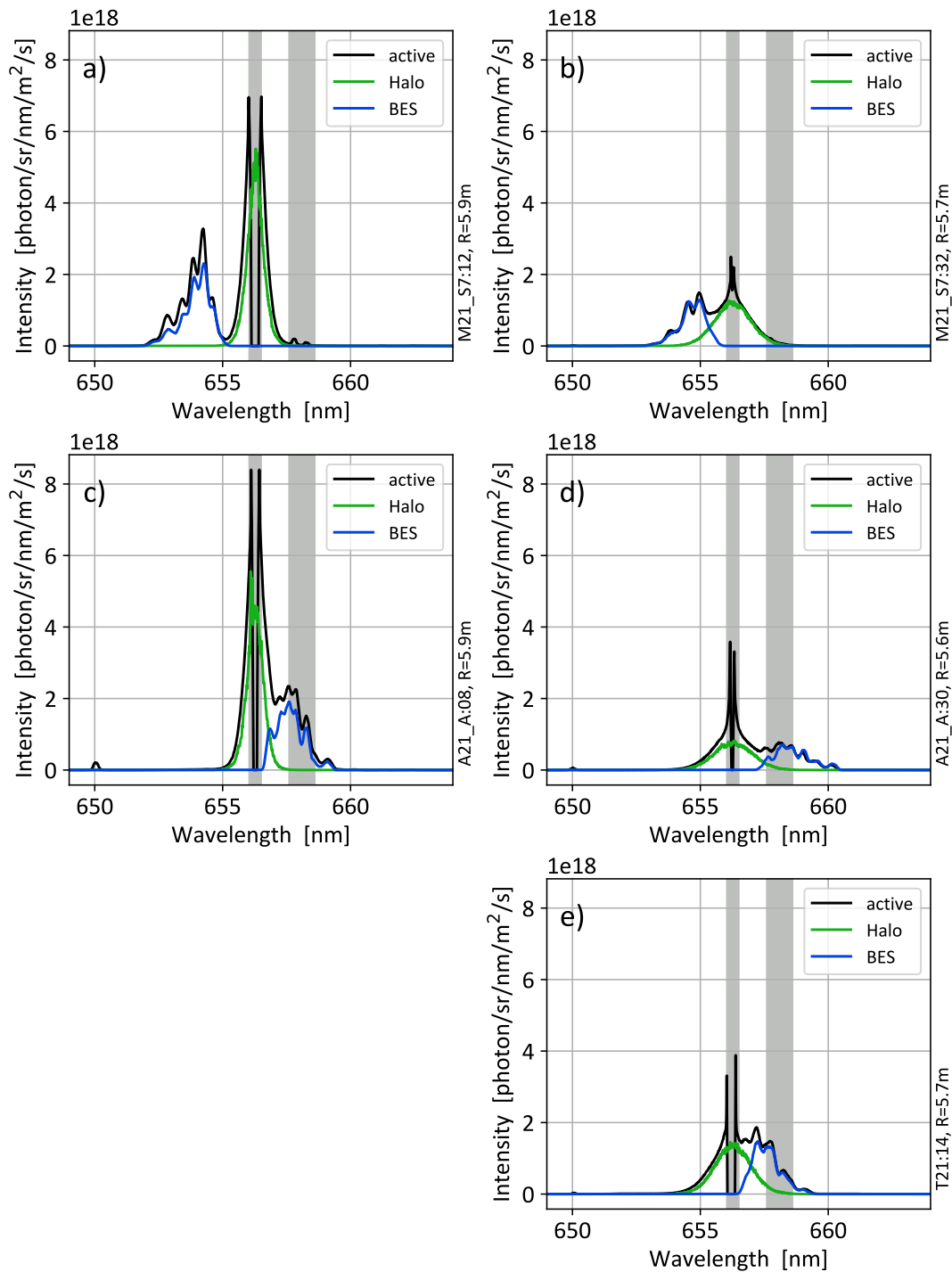


Figure 5.2: Typical active CXRS Balmer-alpha spectra and prediction in discharge #20180823.037 for each observation port, with solid black line the measured spectra, grey the cold-Balmer alpha and carbon emission affected area, not included in the fitting, shown. Blue color marks the BES while green the halo emissions.

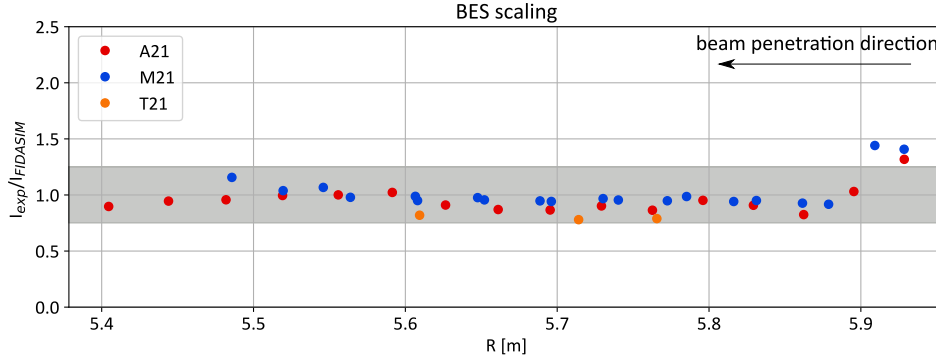


Figure 5.3: BES scaling factors obtained by fitting the FIDASIM predicted beam emission to the measured intensities. Different colors mark different observation ports.

(second column), well explained by a decrease of the beam density as it penetrates the plasma. Moreover, the beam emission is blue-shifted in the case of the M21 port, while the A21 and T21 ports observe the beam emission at red-shifted wavelengths. We can also see that the beam emission prediction by FIDASIM is in good agreement with the measurements, particularly in the plasma core. The spectral shapes and intensities of the various channels are well reproduced by FIDASIM. This is particularly noteworthy as the comparison between the simulation and the absolutely calibrated measurement does not consider a scaling factor and therefore proves the validity of the model and input data. Nevertheless, slight differences between the calibrated measurement and prediction remain.

To address these differences, the FIDASIM-predicted total BES intensity (sum of all energy components) was fitted to the active measurement using a channel-dependent scaling factor. For the spatial location of the measurement, the major radius of the closest point on the given line of sight to the neutral beam axis was chosen, denoted with R . This scaling provides a measure of any global discrepancy between the experiment and simulation, as shown in figure 5.3. If the ratio of the measured and predicted emission is higher than one, it means that more light is observed than predicted, while if the ratio is lower than one then FIDASIM over predicted the observed light. Matching the intensities means that the ratio of these two is unity which is the goal of the validation process. In the edge plasma, at $R > 5.9$ m range we can see that at the first few channels FIDASIM underpredicts the measured BES emission, this is due to the plasma edge induced electron impact excitation providing additional BES light not considered accurately enough in the simulation. Besides this, the FIDASIM-predicted total beam emission is in good

agreement with the measurement, observing no significant trend over the whole plasma cross-section from the low-field side to the high-field side, staying within a $\pm 25\%$ error. The overall good agreement demonstrates that FIDASIM can incorporate kinetic plasma profiles and beam parameters accurately and so it can be used to provide a measurement of the beam power to the torus value if needed. This method has been further validated against calorimetry measurements of the beam power to torus value, published in [52].

In addition, it should be noted that the minor discrepancies, seen between the measurement and the simulation might provide insight into the shape of the beam. For example, we can see in figure 5.3 that the scaling factors for port A21 (red dots) are systematically lower than unity while for the M21 port (blue dots) are close to one. This suggests that the measured A21 intensities are lower than what FIDASIM would predict while the M21 prediction is in agreement with the data. As port A21 is looking toroidally at the beams, this suggests that the vertical width of the beam could be wider, implying a slightly higher divergence in this direction. Note here that changing the vertical width would not significantly affect the M21 view as this one is intersection NBI at 45 degrees.

5.1.2 Halo modeling validation

In the next step, state resolved halo neutral densities were predicted and the corresponding emission pattern was calculated. A typical beam- and halo density is shown in figure 5.4. We can see in the cuts, figure 5.4 b) and c), that as the temperature is fairly low, the shape of the halo is not significantly wider than the beam itself while having the same order of magnitude density.

Based on the predicted halo density, the halo emission was calculated, the corresponding halo spectra is shown in green in figure 5.2. We can see that the predicted halo spectral shapes match well both the core and edge measurements of the A21, M21 and T21 ports. As the ion temperature is lower in the plasma edge than in the core the first column (the edge channels) show narrower halo emission than the second. Similarly to the beam emission, the halo density is higher closer to the neutral beam source, than in the plasma core.

Following a similar approach as for the investigation of the beam emission, figure 5.5 compares the ratio of the observed and FIDASIM-predicted halo emission total intensities. The ratio is close to unity in the plasma core ($5.5 \text{ m} < R < 5.9 \text{ m}$), while the measured halo

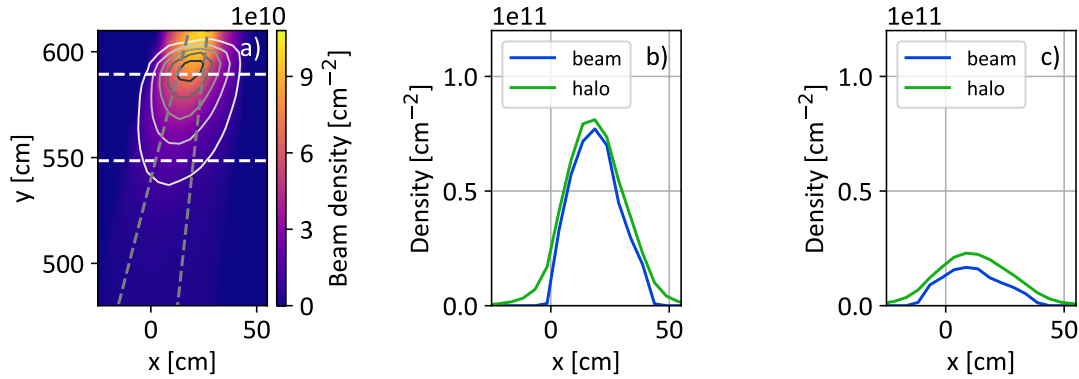


Figure 5.4: Vertically integrated beam density with the contours of the vertically integrated halo density in the midplane. The grey dashed lines mark the NBI injection directions. The two white dashed lines mark the positions, along which the integrated beam- and halo density is plotted at $y_1 = 5.9$ m and $y_2 = 5.5$ m.

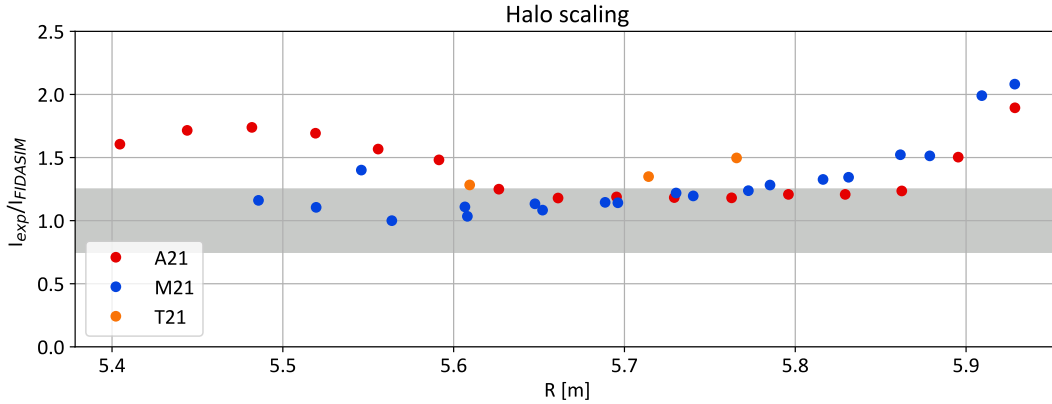


Figure 5.5: Beam halo scaling factors obtained from fitting the FIDASIM-predicted halo emission to the measured intensities. Different colors mark different ports for observation.

emission becomes higher than the FIDASIM prediction (with a factor of 2) towards the edge region, and in the inboard side for the A21 port at $R < 5.6$ m. The good agreement between the prediction and the measurements in the plasma core further solidifies the reliability of FIDASIM as a synthetic diagnostic, and we can say that the active neutral population is well reproducible with FIDASIM. Although we have to keep in mind, that discrepancy we observe at the plasma edge might be an indication of the interaction of the edge cold population with the thermal ions as it was investigated in [68], and we will discuss it in later chapters.

5.1.3 FIDA emission modeling

With the beam and halo densities calculated, FIDASIM can calculate the FIDA emission based on an ASCOT predicted fast-ion distribution functions, shown earlier in 4.9.

Typical measured and FIDASIM predicted spectra are shown in figure 5.6 on a logarithmic y scale. Here it should be noted that the intensity of the FIDA emission is typically significantly lower than the experimentally observed one. Therefore, the prediction shown in figure 5.6 is also shown scaled to fit the data in order to better compare the spectral shape.

For this fitting, a suitable wavelength range was determined following three considerations. First, as the dominant spectral features with high intensities are the halo- and beam emissions, beneath which the FIDA signal is lost in the noise level, a wavelength range far from these are required. This means that typically wavelengths where $|\Delta\lambda| > 3$ nm considered. Second, not modelled impurity lines, as shown in figure 3.15 for the reference Balmer-alpha spectrum measured by the ILS-red, should be avoided too. As we saw there, on the blue shifted side is mainly limited by an OII line at 650 nm. On the red-shifted side of the spectrum line emission of carbon lines and molecular hydrogen limits the observation. The third limitation is the natural decay of the observed FIDA emission. As we saw in the prediction part in figure 4.10 the FIDA emission typically has an intensity cut-off close to the Doppler-shift produced by the maximal injection energy particles, which restricts the observable wavelength range to $|\Delta\lambda| < 6$ nm. Taking all these considerations into account, the following wavelength ranges were selected for fitting the FIDA emission, shown as dark red bands in 5.6:

port	$\Delta\lambda < 0$ [nm]	$\Delta\lambda > 0$ [nm]
A21	651.0 - 653.0	-
M21	650.5 - 651.7	660.3 - 660.8
T21	650.4 - 651.2	660.3 - 660.8

Table 5.1: Wavelength selection for fitting blue- and red-shifted FIDA emission for different ports.

As there was no usable wavelength range available for port A21 red-shifted side, which is sensitive to particles with positive pitch values (injection direction propagating particles), the negative pitch sensitive parts of the spectra of the different ports were compared (red shifted emission from both M21 and T21 port, blue shifted emission for A21 port).

The wavelength ranges used for the fitting are highlighted in red in figure 5.6. Moreover,

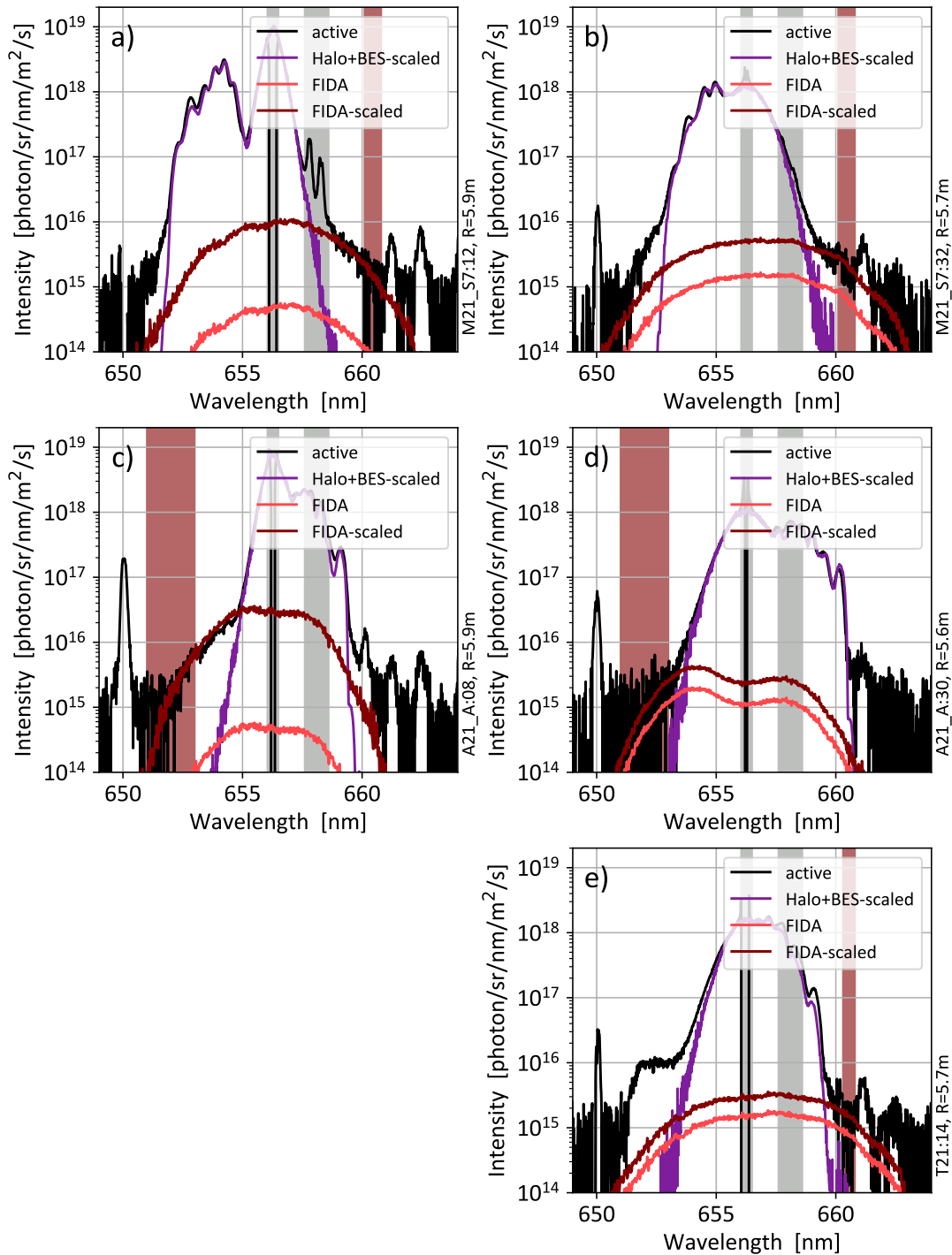


Figure 5.6: Typical active CXRS Balmer-alpha spectra and prediction in discharge #20180823.037 for each observation port, with solid black line the measured spectra, grey the cold-Balmer alpha and carbon emission affected area, not included in the fitting, shown. FIDASIM predicted FIDA emissions depicted with light red, while the scaled one, fitted to the counter-propagating particle sensitive part of the spectrum is colored dark red.

the measured active spectra for all the ports are given black and the FIDASIM-predicted active FIDA emission, scaled to the measurement is plotted in dark red (the not scaled FIDA prediction is plotted with light red color). Finally, the sum of the fitted halo and beam emission is plotted with purple. This helps separating the regions, where the beam and halo emission is dominant from those, where FIDA emission could be expected. The predicted active FIDA emission matches the shape of the measurement at the fitted region, although significant discrepancies can be observed at the non-fitted side, this observation will be further discussed later. The scaling factors, required to best-fit the measured spectra of all available channels are given in figure 5.7.

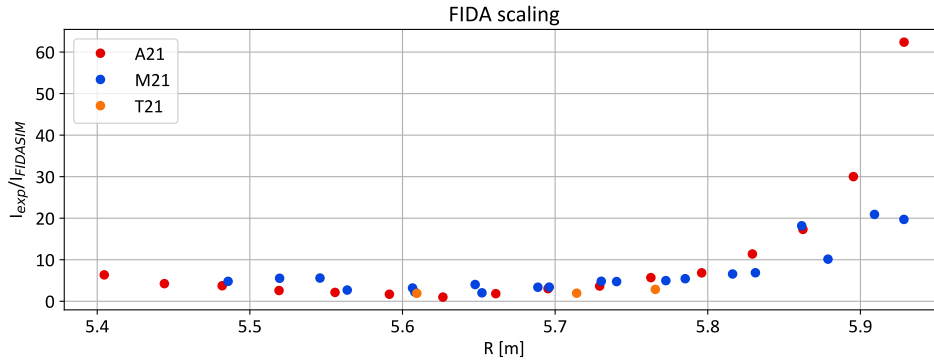


Figure 5.7: Active FIDA emission scaling factors obtained from matching the FIDASIM-predicted FIDA emission to the CXRS system measured absolute intensities for the counter injection direction propagating particles ($\Lambda < 0$). Different colors mark different ports for observation.

Large scaling factors are obtained, indicating an underestimation of the observed FIDA intensities for all observation directions. While the core channels at about $R \approx 5.6$ m, exhibit scaling factors $I_{exp}/I_{FIDASIM}$ approaching unity (about three), the scaling factors increase significantly towards the edge of the plasma, up to 60 times more radiation observed than is predicted by FIDASIM.

As the observed FIDA light is proportional to the line-integrated product of the local donor neutral density and the fast-ion density, at least one of these two contributions must have strong discrepancies to the modelling activity presented, here. Given that the predicted active neutral donor population, the beam and halo densities have been validated by comparisons between the measured spectra and FIDASIM predictions, either a discrepancy with the assumed fast-ion densities or additional sources of donor neutrals could explain the mismatch. Since the mismatch increases towards the plasma edge, a

significant contribution of passive FIDA radiation might be a likely explanation. Passive FIDA radiation has not been considered in our simulations and is expected to be stronger for edge channels as these are more tangential to the edge region and therefore have longer intersection lengths with the region of large neutral densities.

Chapter 6

Investigation of passive FIDA emission

As demonstrated in the previous chapter, the implementation of FIDASIM at W7-X can well reproduce the active beam- and halo emissions. This shows that the neutral beam injection parameters, the observation geometry, kinetic profiles and the plasma equilibrium have been implemented and adapted properly for W7-X. Moreover, the good agreement between the measured and predicted spectral emissions show that FIDASIM reliably predicts the active neutral population. However, it was observed that fitting the measured FIDA emissions with the FIDASIM predictions revealed an ever-increasing discrepancy towards channels that are more tangential to the plasma edge. This suggests that the cold neutral produced passive emission significantly contributes to the total FIDA signals which has not yet been considered. In the following, a detailed study of the passive emission will be provided which demonstrates that the FIDA radiation at W7-X is often dominated by emission arising from the scrape off layer.

6.1 Modeling of the passive emission with confined fast-ions

Passive FIDA radiation arises from charge exchange reactions between fast ions and neutrals present in the edge region of fusion plasmas. The cold neutrals typically originate from the machine walls and divertors due to recycling particle fluxes and from gas fuelling

valves.

6.1.1 Cold neutrals simulation with KN1D

To incorporate this additional donor population, FIDASIM has been supplied with 1D neutral H^0 density profiles from the KN1D code, introduced in section 2.3.1. The KN1D simulation has been supplied with kinetic profiles measured by the diagnostics introduced in section 3.4. Since these diagnostics do not properly cover the SOL region, exponential decay of the kinetic profiles, with a radial scale-length of 2.5 cm has been considered for $\rho > 1$. The radial scale-length was chosen to mimic the extent of the islands of W7-X. The temperature of the incoming neutrals was set to 3 eV at the wall, positioned 10 cm distant to the last closed flux surface. Figure 6.1 shows a representative neutral density profile from KN1D on a semi-log scale. Note that the 1D KN1D code can not cover the complex

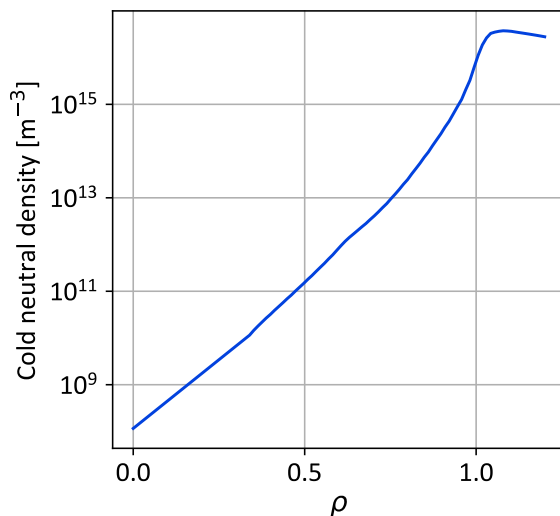


Figure 6.1: Neutral density profile predicted by KN1D.

3D nature of the W7-X edge region and thus only provides a rough approximation of the neutral density profile. A more detailed analysis, including 3D neutral density profiles from a high fidelity code EMC3-EIRINE [40] is a topic of future interest, but out of the scope of this thesis. In addition, KN1D needs to be supplied with H_2 pressure at the wall which is currently unknown at W7-X. Thus an arbitrary scaling factor is considered when comparing synthetic passive FIDA spectra with the measurements. Because of this, our

analysis focuses only on the qualitative shape of the neutral density profile and not on its absolute values.

6.1.2 Passive FIDA emission prediction using ASCOT4

With the simulated neutral density profile and the ASCOT4 predicted fast-ion distribution, passive FIDA emission can be calculated in a similar manner as previously done in [20] in the confined plasma region. Figure 6.2 shows example spectra for edge (1st column) and core (2nd column) channels of the three ports available at W7-X. The experimental data is shown in black, the dark red lines show the sum of the scaled passive FIDA emission and the active contribution is shown in light red. As we assumed, that the previously shown active FIDA prediction might be correct only the predicted passive radiation has been scaled in order to get the best possible match of the sum of the unscaled active emission plus the passive emission with the measured data. The scaling is performed to match the total emission only in the spectral regions shown in dark red. As can be seen, the total emission's spectral shape is similar to that of the active spectrum and cannot explain the full spectral shape of the experimental data. When matching the simulation and data on only one side of the cold Balmer alpha line, the other side is strongly underrepresented or over-predicted.

This observation of discrepancy is the most prevalent for the T21 port (3rd row) where a clear emission shoulder forms on the blue-shifted side ($651 < \lambda < 652$ nm). This spectral feature is completely missing from the prediction. This suggests that the fast-ion distribution predicted by ASCOT4 is missing a certain population of fast-ions responsible for the additional FIDA radiation. In fact, ASCOT4 predicted fast-ion densities are limited to the $\rho < 1$ region (henceforth referred to as ASCOT4 fast-ions) and, thus it only allows to predict the emission from the confined plasma.

As illustrated in figure 6.3, a significant passive FIDA contribution could be originated from the scrape off layer (so far we could only consider emission from the $\rho < 1$ region), currently neglected, as the passive FIDA signal is proportional to the product of the fast-ion density and the cold-neutral density. As can be seen in the edge plasma the fast-ion density is still finite and the neutral density reaches high values. Figure 6.3, hence, demonstrates that knowledge on the edge fast-ion density is very important to understand the FIDA spectral shape observed at W7-X. This is why detailed modelling of the edge fast-ion

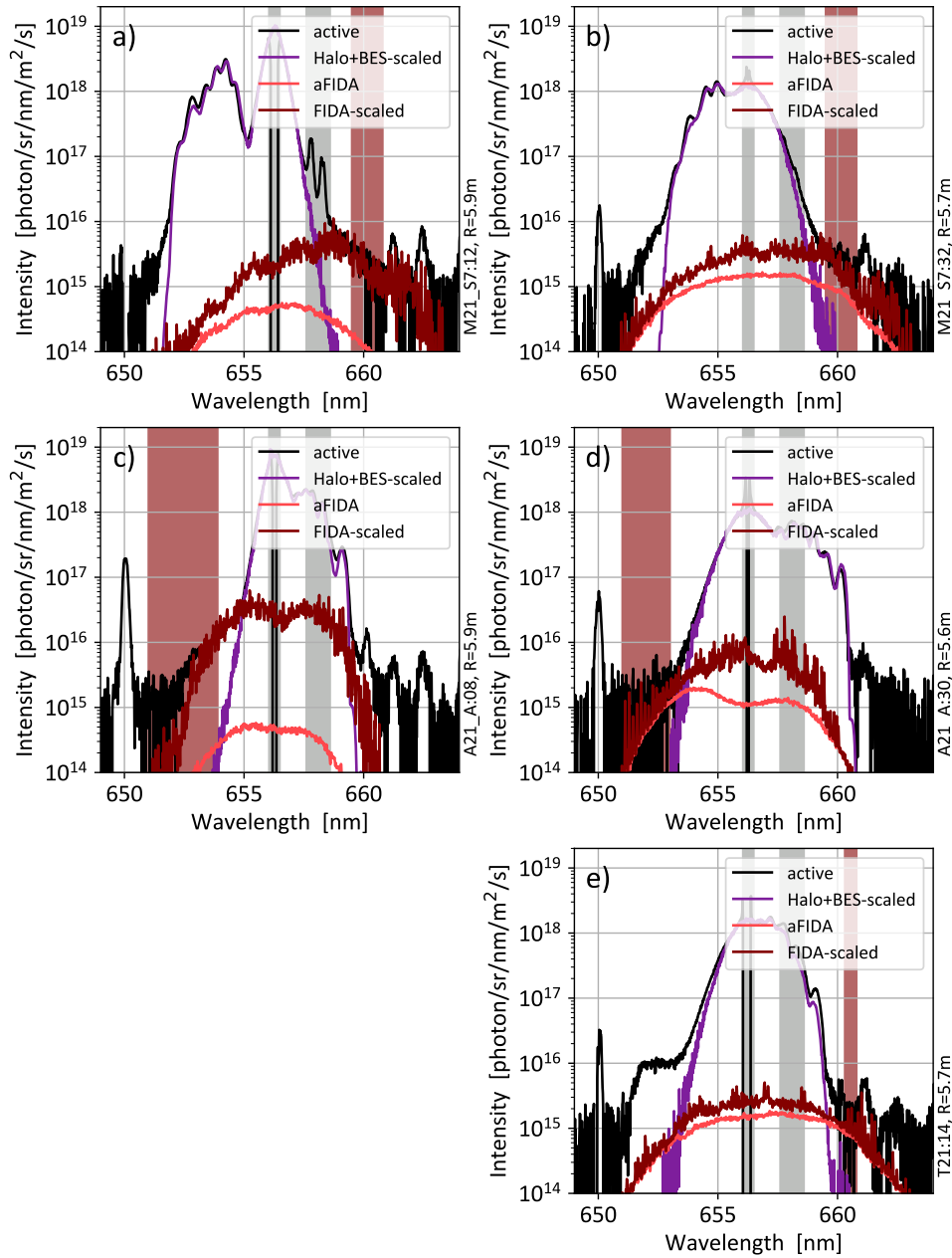


Figure 6.2: Passive FIDA spectra prediction by FIDASIM using ASCOT fast-ion distribution function. Different rows correspond to different ports, M21, A21 and T21 in order. The first column marks an edge, while the second a core observation.

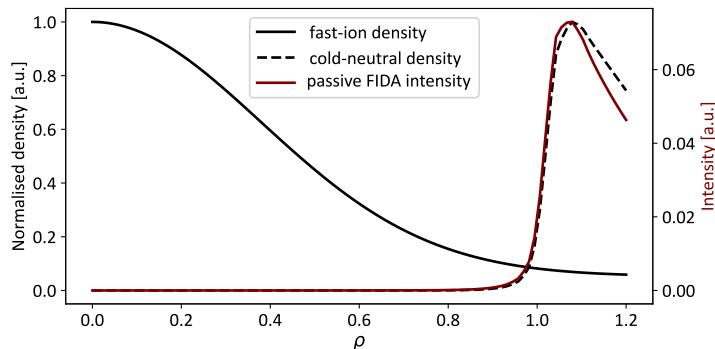


Figure 6.3: Schematic ingredients and spatial distribution of the passive FIDA emission.

distribution function has been performed in the framework of this thesis.

6.1.3 Extended VMEC boundaries

First, an extended equilibrium reconstruction is required to provide a simulation volume that covers the edge region. This can be obtained from the VMEC code by artificially inflating the last closed flux surface, as shown in figure 6.4 for the investigated case. This procedure leaves the plasma core region unaffected (position of flux surfaces, and magnetic field structure), while extending the flux labeling upto $\rho \leq 1.2$. Figure 6.4 a) shows the 88° poloidal cross-section, and b) the horizontal cross-section at the midplane of the flux surfaces around the NBI injection volume. The bold black lines show the last closed flux surface ($\rho = 1$), while the dashed lines represent the extended VMEC boundary. For reference, the operational beams, S7 and S8, are depicted with red and blue. Note that this extended VMEC equilibrium provides a simplified picture as the island structure of W7-X in the SOL region is not considered.

Edge fast-ion distribution function prediction

To model the edge fast-ion distribution, a two steps process was implemented in FIDASIM. First, fast-ion birth positions are determined in the range of $0.9 < \rho < 1.2$ using FIDASIM's NBI injection module by following a total of 500000 NBI neutral markers for each beam until they ionize in the plasma or hit the wall on the opposite side of the device. The ionization positions and velocities of the, hereby, born fast ions are then stored. Figure 6.5 shows a histogram of the number of ionized marker as function of major radius colored

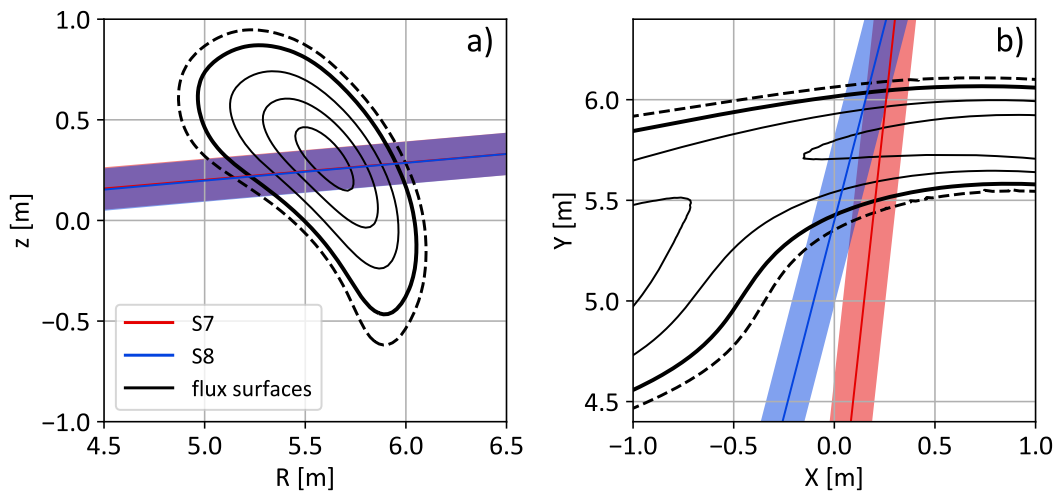


Figure 6.4: Flux surfaces with the extended VMEC equilibrium. The last close flux surface is marked with bold line, while the boundary of the extended equilibrium is marked with dashed line. For reference the lines of sight of the two NBI sources (S7, S8) are shown as well in red and blue color.

as blue bars. The data in black represents markers born in the edge region that will now

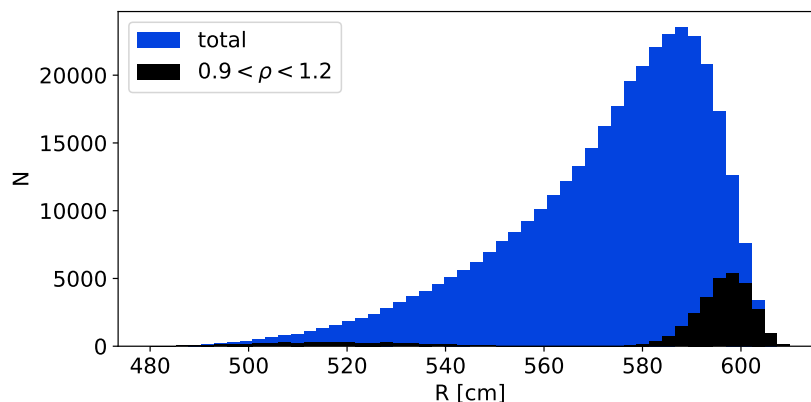


Figure 6.5: FIDASIM predicted distribution of ionized particles as a function of major radius, marked with blue bars. Particles born in the plasma edge, selected for further simulation are depicted with black bars.

be considered in the orbit following, as they are neglected by ASCOT4 and therefore were not included in the prediction in figure 6.2.

Based on the birth positions and velocities, full-orbit particle tracing with Boris in-

tegration scheme [69] is applied, considering a time step of 10^{-9} s (well resolving their gyro-motion) and using the extended VMEC equilibrium for the background magnetic field. The particles are followed for $50 \mu\text{s}$ which is much lower than time needed for fast particles to eventually hit the plasma vessel or divertor elements in the plasma edge (taking an average parallel distance to the wall of 275 m [70], and particle energy of 50 keV, with pitch of 0.5 the wall-collision time is $200 \mu\text{s}$), which are not considered in the simulation. Due to the short simulation time, it is not necessary to consider the slowing down process either which is on the order of a few ms, considering the edge plasma parameters. A 3D plot containing representative particle trajectories is depicted in figure 6.6. The last closed flux surface is depicted with black, similarly as before. The solid purple lines represent the fast ion orbits, and NBI sources S7 and S8 are shown in black. Furthermore, central lines of sight of the A21, M21 and T21 ports are shown with blue, red and orange solid lines, respectively. As can be seen, the injected particles are mainly passing and move away from the birth location in the counter-clockwise direction, following field lines. At

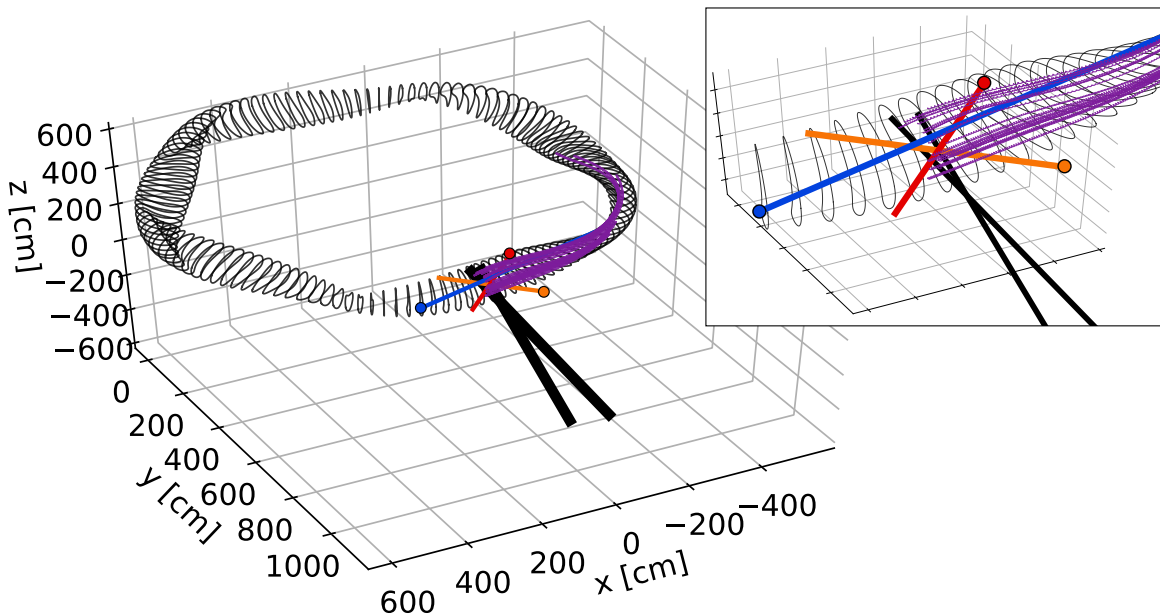


Figure 6.6: Edge fast-ion trajectories in W7-X, colored purple. The last closed flux surface is depicted with black solid line, the NBI injection directions with bold black line. Observation ports are colored red, blue and orange.

this point a couple of remarks can be made. The M21 and T21 ports lines of sight cross the same particle ensemble, right in front of the NBI injection port (later referenced as

prompt fast-ions, due to the fact as they are born on open field lines they are getting lost on short time-scales), while the case of A21 port is more complex. Edge channels from the A21 port might cross the same cloud, but others will see particles further away from this injection location, i.e. particles that have already travelled some distance away from the NBI.

The flux of each marker is used to store fast-ion densities on a cylindrical grid with $\Delta r = \Delta z = 6$ cm resolution in each poloidal plane at $\Delta\varphi = 3.6^\circ$ increments. In addition to their position, their local pitch and energy values are stored such that an edge fast ion distribution function is obtained. Note here that the radial extent of the fast-ion distribution is slightly widened compared to the initial birth profile due to the finite Larmor-radius and radial drifts of fast ions. Typically, 50000 markers are followed, resulting in a fast-ion distribution function with reasonable statistics. Figure 6.7 shows resulting fast-ion densities at two different toroidal locations corresponding to the toroidal angle with the highest fast-ion density along the given line of sight. Flux surfaces are depicted with solid black lines and the last closed flux surface is indicated with a thicker line. Moreover, the plasma limiting structures are added in grey. As can be seen, there are finite fast ion densities on both the inboard and outboard sides of the plasma which are explained by the ionization or injected neutrals at these two positions. As the NBI fires from the outboard side (high R), the outboard fast-ion density is higher than the one on the inboard side where NBI is strongly attenuated. Figure a) and c) shows the poloidal cross-sections at which the fast-ion density is highest for the selected M21 edge, and T21 core line of sight. The positions where the lines of sight cross the R-Z plane are marked with dots. Clearly, the lines of sight encounter large fast-ion densities in the outboard SOL region. The poloidal cross-section averaged fast-ion velocity-space distributions are plotted for the two toroidal angles in figures b) and d). We can observe the three energy contributions from the different energy fractions of the NBI at 48, 24 and 16 keV. Regarding the pitch, four smaller groups can be differentiated with different intensities at given energy. The two intense ones with $0.25 < \Lambda < 0.45$ correspond to fast particle populations originating from the two operational beams on the outboard side, and the other two populations at higher pitches $0.5 < \Lambda$ represent fast particles on the inboard side.

To additionally illustrate the edge fast-ion density present along the lines of sight, other than just showing the poloidal plane with the maximum density, the simulated fast-ion density has been plotted in two different planes along a given line of sight: a horizontal

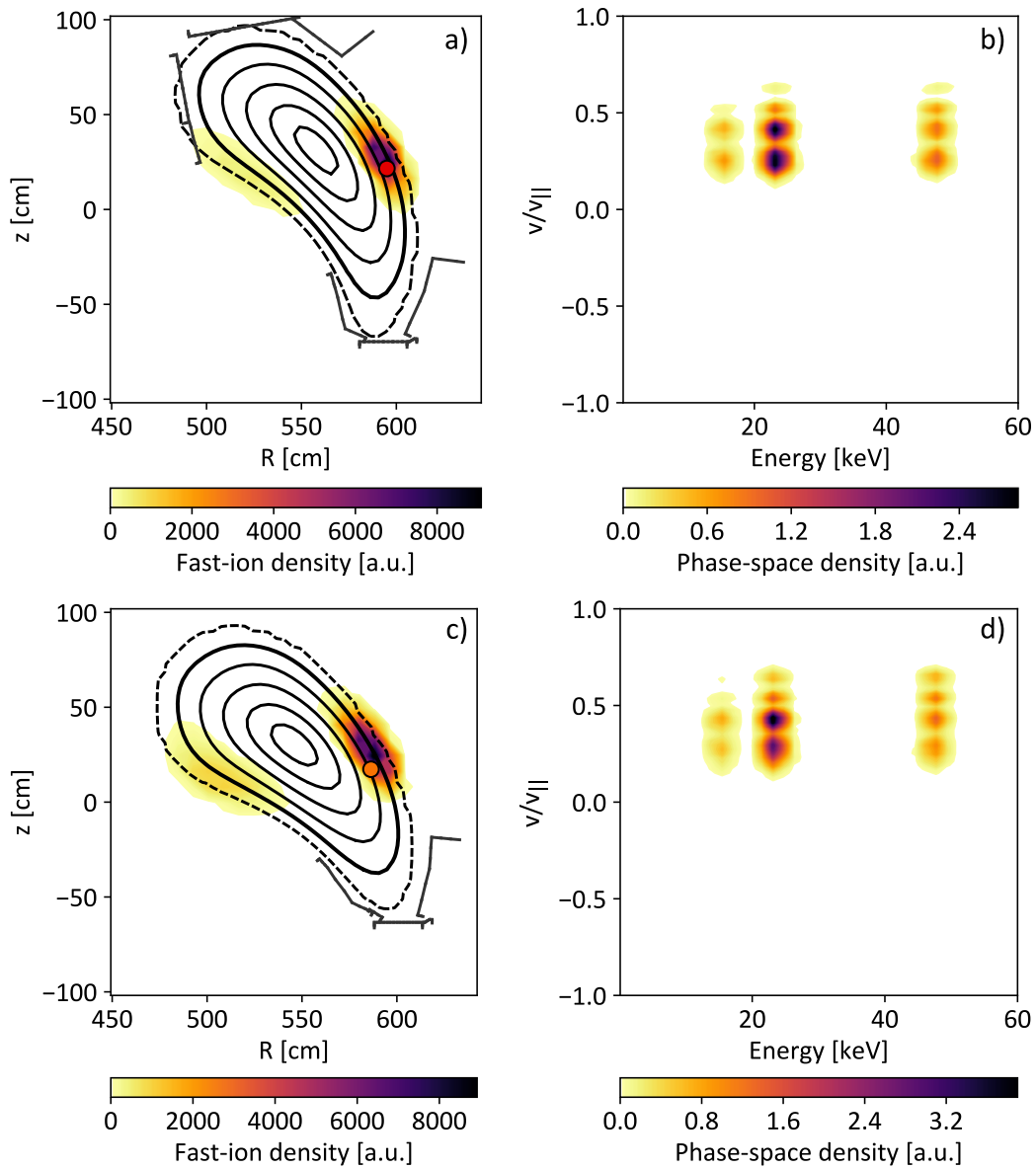


Figure 6.7: Edge fast ion densities at the toroidal angle of the highest fast-ion density locations for an M21 and T21 port line of sight and the corresponding poloidal cross-section averaged fast-ion distribution functions.

one and one in a normal direction, as illustrated in figure 6.8.

Example plots are shown for an edge channel of the M21 port in figure 6.9 and for an edge channel of the A21 port in figure 6.10. As T21 port did not have edge observation available, a core channel is shown in figure 6.11. Each figure shows the horizontal and normal plane relative to the presented line of sight. The points of crossing of the NBI

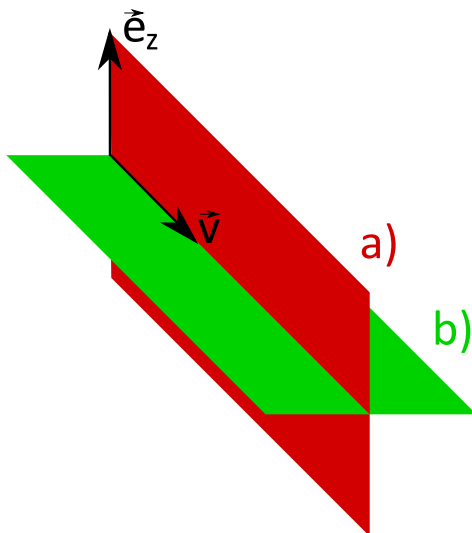


Figure 6.8: \vec{e}_z is the Cartesian z-axis, while \vec{v} is the direction vector of a given line of sight. The red vertical plane and the second green both includes the line of sight and chosen to later describe the spatial extent of the prompt fast-ions.

injection lines of sight are marked with two "X"-s along the solid line marking the line of sight, marking the region of active emission. Flux surfaces are shown with solid line, while the inflated boundary is shown with dashed line, as before. By studying these plots it becomes clear that all the channels, crossing the NBI injection in the edge, will inevitably see the prompt particle cloud. The main difference between the relevant M21 and A21 port lines of sight and the T21 port lines of sight is that in the case of the latter the NBI intersections are spatially separated from regions of high prompt fast particle density while in the case of the A21 and M21 ports the active and prompt emission overlaps.

It should be noted that in the case of the T21 port the observation of the prompt FIDA emission is inevitable, while for the A21 and M21 port, core lines of sight can be selected such that their relevant FIDA signal minimizes the contribution of the prompt particle population as shown in figure 6.12 and figure 6.13. This possibility of selecting lines of sight that avoid the prompt passive FIDA radiation will be discussed in more detail in the discussion chapter.

6.1.4 Prompt-fast-ion passive FIDA prediction

Using the full 5D fast-ion distribution described earlier and the 1D cold neutral density shape predicted by KN1D, passive FIDASIM simulations have been run.

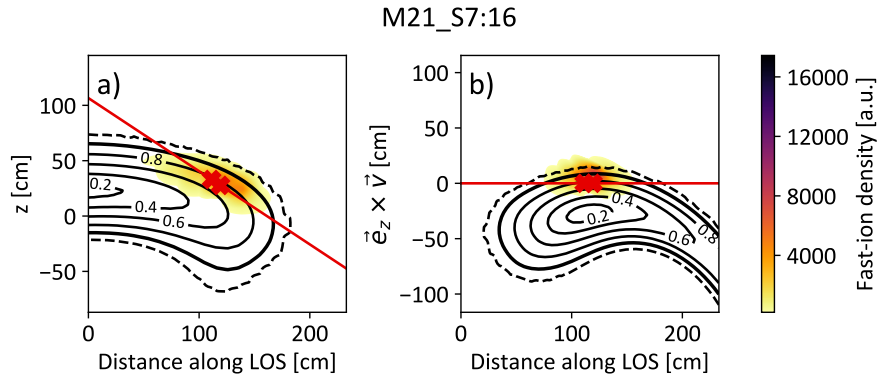


Figure 6.9: Fast ion density for an M21 edge line of sight in the a) horizontal plane, including the line of sight and b) the binormal plane. Crossing points with the NBI sources are marked with "X"-s.

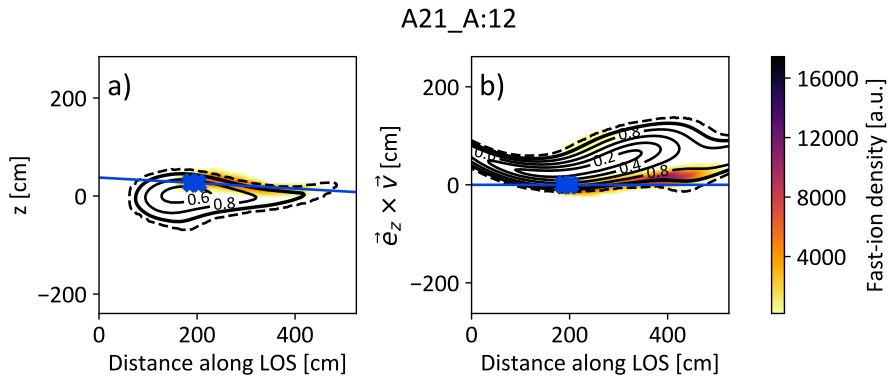


Figure 6.10: Fast ion density for an A21 edge line of sight in the a) horizontal plane, including the line of sight and b) the binormal plane. Crossing points with the NBI sources are marked with "X"-s.

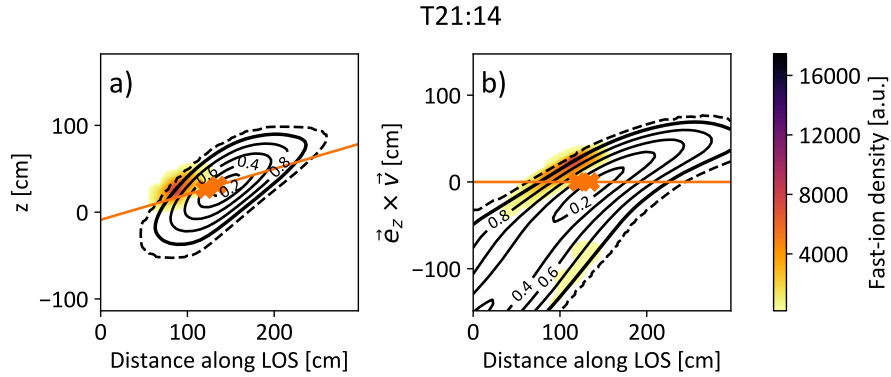


Figure 6.11: Fast ion density for an T21 line of sight in the a) horizontal plane, including the line of sight and b) the binormal plane. Crossing points with the NBI sources are marked with "X"-s.

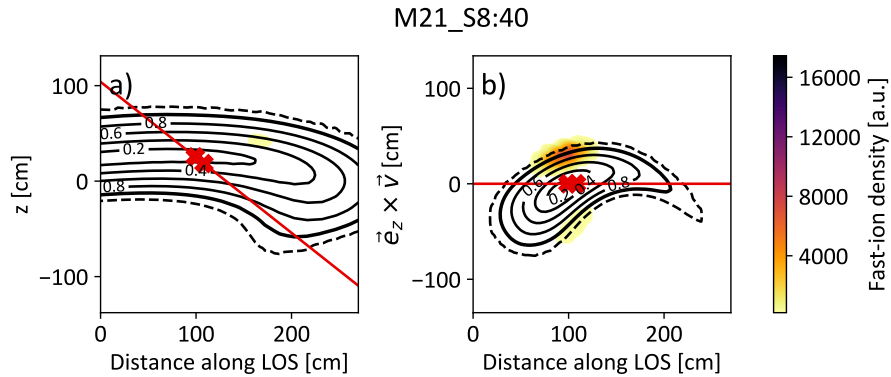


Figure 6.12: Fast ion density for an M21 edge line of sight in the a) horizontal plane, including the line of sight and b) the binormal plane. Crossing points with the NBI sources are marked with "X"-s.

Examples of the predicted prompt spectral shape are shown in figure 6.14 for M21 and T21 port lines of sight. The first row shows M21 port edge- and core line of sight measurements, while the second row shows two T21 port spectra. In the case of the A21 port the prompt FIDA emission is located beneath the red shifted beam emission, separation of the two contributions was not possible given uncertainties in the forward modeling of synthetic BES spectra thus results from it not presented here. The scaled FIDA emission based on the ASCOT-predicted fast-ion distribution function is depicted in dark red, while the halo and BES predictions are shown in purple color. The scaled prompt passive FIDA emission, predicted by using the edge fast-ion distribution function is shown in dark blue. The wavelength ranges used for scaling the passive prompt and ASCOT FIDA spectra are indicated with blue and red shaded regions respectively.

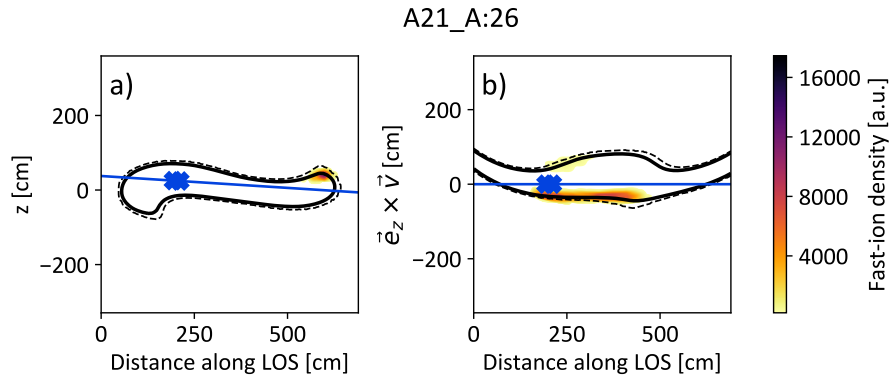


Figure 6.13: Fast ion density for an A21 edge line of sight in the a) horizontal plane, including the line of sight and b) the binormal plane. Crossing points with the NBI sources are marked with "X"-s.

Note here that scaling of the passive radiation is still necessary as absolute values of the neutral density – responsible for the passive emission – are currently not available. Hence, our analysis is restricted to studying the spectral shape of emission produced by the prompt edge fast-ion population.

The total predicted passive emission’s spectral shape, composed of the ASCOT and prompt fast-ion’s contribution, fits the observation very well. The passive FIDA radiation is dominant on the blue Doppler-shifted side and is more pronounced for the T21 port lines of sight, where it is not superimposed by the beam emission. Here, it is important to note that the passive prompt FIDA light is well distinguishable from that of the ASCOT-predicted passive FIDA spectrum, explained by significantly differing fast-ion phase-space distributions (compare figures 4.9 and 6.7). The very good agreement between the combined prompt and ASCOT predicted FIDA spectra and observation clearly demonstrates that passive radiation often dominates the measured FIDA spectra at W7-X. This important result will need to be considered when analyzing the fast-ion confinement properties based on FIDA spectroscopy.

6.2 Characterisation of the passive emission with weight functions

Similarly to the active radiation, weight functions can be used to characterise the velocity-space sensitivity of a given line of sight to the edge region’s radiation. However, passive

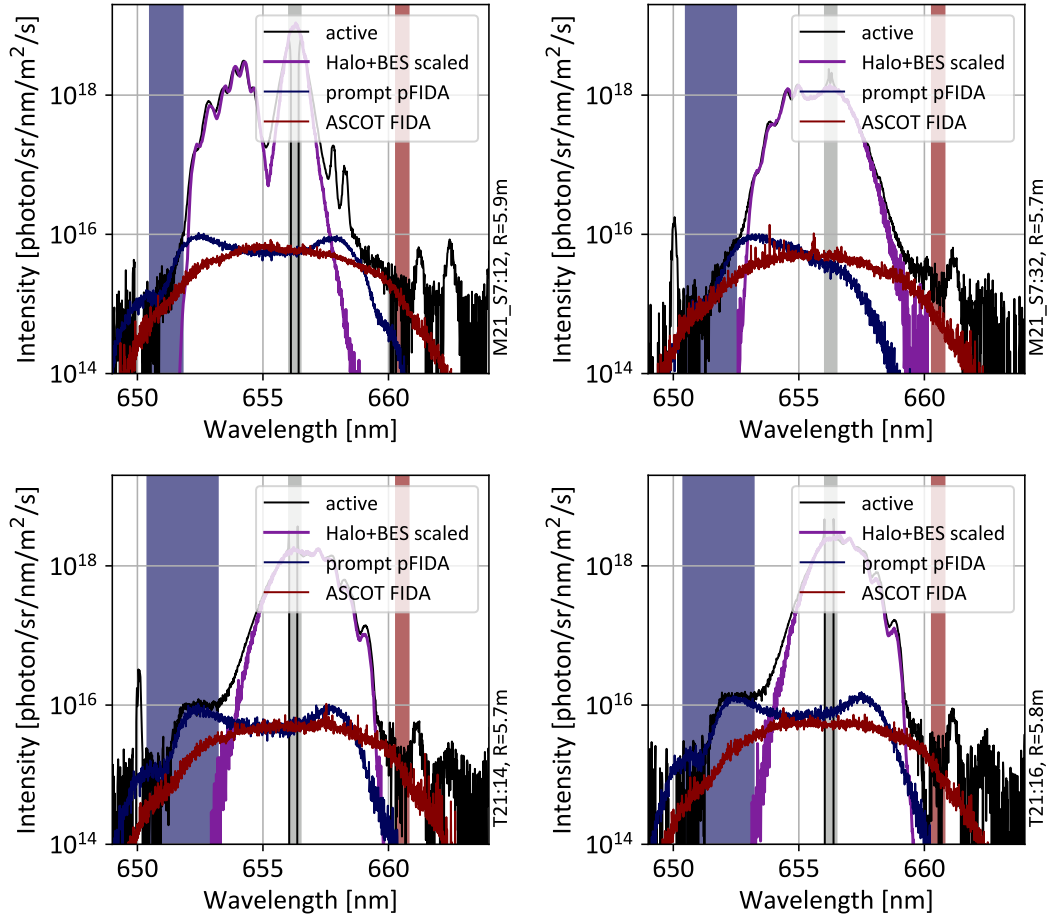


Figure 6.14: FIDASIM's prediction of edge passive FIDA emission for different M21 and T21 port channels. The first row corresponds to M21 while the second to T21 port channels. Shaded areas are used to scale the passive emission contributions from the two different fast particle population.

measurements are line of sight integrated which requires additional assumptions to estimate LOS-averaged passive weight functions. First, we assume a uniform, average neutral density in the edge region between $1 < \rho < 1.2$, and zero everywhere else, thus radiation arises only from this region. This means that all the points in the edge along a line of sight can have an identical contribution to the measured spectra. Secondly, we average the weight functions along the line of sight in the regions of finite background neutral densities. Note here that a more detailed point-by-point weight function calculation would be needed to incorporate the realistic 3D neutral density shape.

A Python code has been implemented which starts the calculation by stepping along

the line of sight with 2 cm increments. At each step, the magnetic field structure, strength and ρ value is determined using the VMEC provided equilibrium. At each position the photon emission is calculated that would originate from particles with different energies, pitches and gyro angles in the range of $0 < E < 60$ keV, $-1 < \Lambda < 1$ and $0 < \theta < 2\pi$. The Doppler-shifted and Stark split spectral contribution is determined for each pitch, energy and gyro angle values. Then the code checks whether the emission manifold (15 Stark emission lines) overlaps with a specified wavelength range. If so, the normalized intensity of the subset of the 15 lines that overlap is added to the corresponding bins on a pitch and energy grid. This provides the line of sight's observed light response to a uniform fast-ion distribution function.

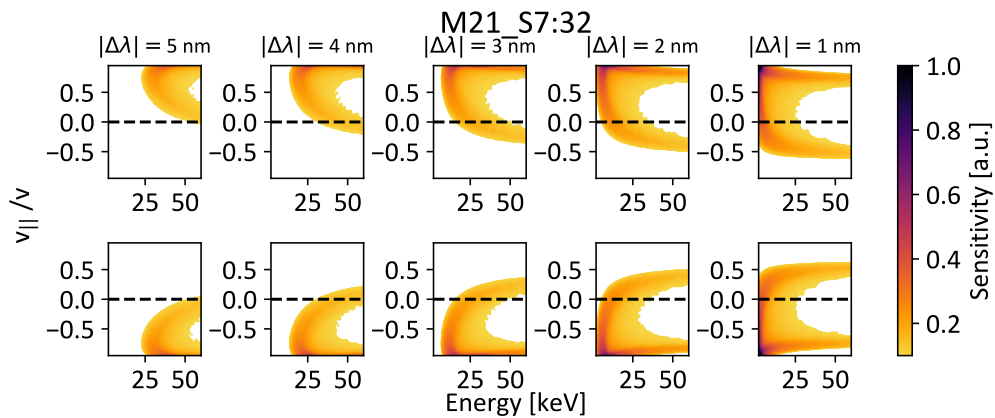


Figure 6.15: M21 port channel characteristic weight function for the passive FIDA measurements at different Doppler shifts.

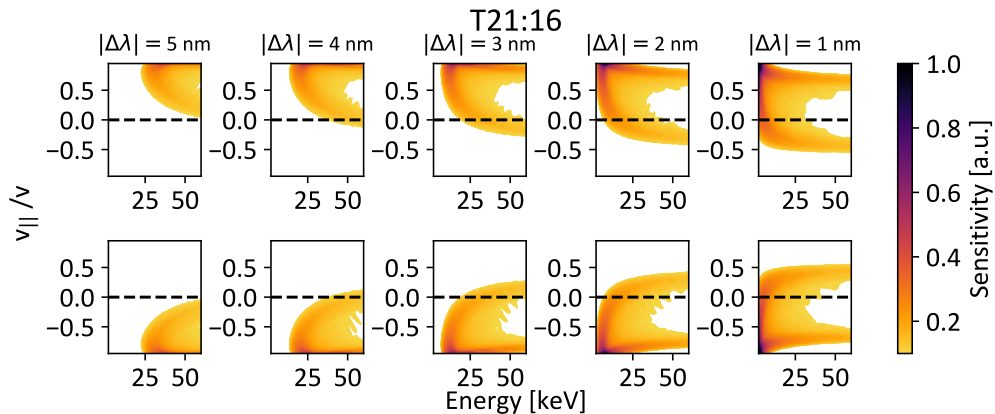


Figure 6.16: T21 port channel characteristic weight function for the passive FIDA measurements at different Doppler shifts.

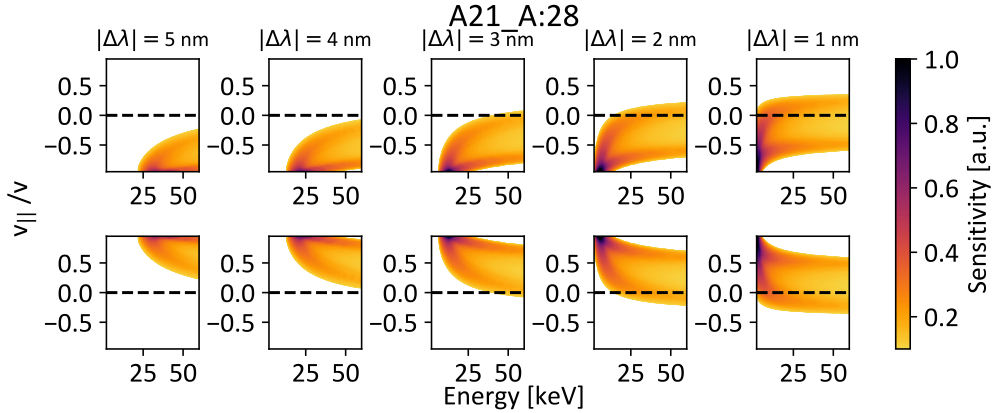


Figure 6.17: A21 port channel characteristic weight function for the passive FIDA measurements at different Doppler shifts.

Figures 6.15, 6.16 and 6.17 show corresponding weight functions of the three observation ports of the W7-X spectroscopy system. The weight functions are plotted for different central Doppler shifts (marked at the top of each column) with a 1 nm wide wavelength range chosen for binning. The first row represents negative Doppler shifts, while the second row corresponds to positive ones.

As we can see in figure 6.15 and 6.16 the M21 and T21 port lines of sight have similar sensitivity to the fast-ion distribution function, as their alignment towards the magnetic field structure is similar. We can observe that due to particle gyration a given fast particle can contribute to both positive and negative Doppler shift.

Note here that when scanning all possible wavelength, a given line of sight would theoretically be able to cover the whole phase-space space. However, most wavelength regions are not accessible due to the beam- and halo emissions or impurity lines.

In the case of the A21 port line of sight, seen in figure 6.17, the weight function is well localised at most wavelengths regarding its pitch to either positive or negative pitches. This means that having a non pitch-symmetric distribution function, as the investigated prompt particle population, it will only appear in one side of the spectrum, making a truly red-shifted prompt passive emission contribution. As in the case of the A21 port the BES is red-shifted too, thus recovery of this prompt emission is unlikely to be possible.

Chapter 7

Boundaries of the fast-ion confinement in W7-X

The presence of strong and difficult to characterise passive radiation makes the detailed study of the fast-ion confinement via FIDA spectroscopy challenging. However, as shown in the previous chapter, it is possible to select lines of sight and spectral regions in which the impact of passive radiation is reduced. Moreover, by applying estimates of the upper and lower boundaries of the background neutral density, restriction of the passive contribution and consequently the total radiation is possible. Based on this knowledge of possible neutral density values, the FIDASIM FIDA emission predictions with ASCOT4 provided fast-ion distribution function can be compared to experimental FIDA measurements and fast ion confinement can be addressed.

7.1 Boundaries of the neutral density

Boundaries of the neutral density profile can be calculated by considering a lower recombination limit and an upper constant neutral pressure limit. For the recombination limit, we assume that the recombination rate of electrons with ions balances the ionisation rate of neutrals at every spatial location:

$$\frac{dn_0(\rho)}{dt} = -R_{ion}(n_e, T_e)n_0(\rho) + R_{rec}(n_e, T_e)n_i(\rho) \quad (7.1)$$

Here R_{ion} marks the effective ionisation rate coefficient of hydrogen neutrals and R_{rec} marks the effective recombination rate coefficient for hydrogen ions. The rate coefficients are taken from the ADAS database [71] and they depend on both the electron density n_e and the electron temperature T_e . Moreover, n_0 is the background neutral density and n_i is the ion density. Here, the latter is calculated from the electron density profile assuming $Z_{eff} = 1.5$. These kinetic plasma profiles are the same as used before for FIDASIM simulations. By assuming an equilibrium state, the time derivative of the neutral density vanishes and we arrive at the following expression for the neutral density:

$$n_0(\rho) = \frac{R_{rec}(n_e, T_e)}{R_{ion}(n_e, T_e)} n_i(\rho) \quad (7.2)$$

This density describes a lower limit of the expected neutral density since recombination processes will always be present in fusion plasmas and hence this provides a baseline under any additional inward transport of neutrals from the plasma edge.

For the upper limit, we assume that the partial neutral hydrogen pressure is constant through the whole plasma volume and that the neutrals are penetrating the plasma through consecutive CX reactions. Due to the CX reactions the neutrals will always have identical temperatures to the background plasma, neutral temperature can be described with the measured ion temperature. Hence, the neutral density can be expressed as:

$$n_0(\rho) = \frac{p_0}{k_B T_i(\rho)} \quad (7.3)$$

Here, p_0 is the constant neutral pressure that can be obtained at W7-X analyzing measurements of pressure gauges that are located close to the walls. Since this approach neglects the ionization of neutrals, thus no loss mechanism is available for them, it provides an upper limit.

A comparison of the resulting upper and lower boundaries of the neutral density profile is shown in figure 7.1.

The hydrogen pressure at the wall was assumed to be 10^{-3} mbar, taken from publication [72] as an upper limit for neutral pressure, and it exhibited a maximal edge neutral density of $\mathcal{O}(10^{16}) \text{ m}^{-3}$ while the recombination limit was 3 orders of magnitude lower with a maximal density of $\mathcal{O}(10^{13}) \text{ m}^{-3}$.

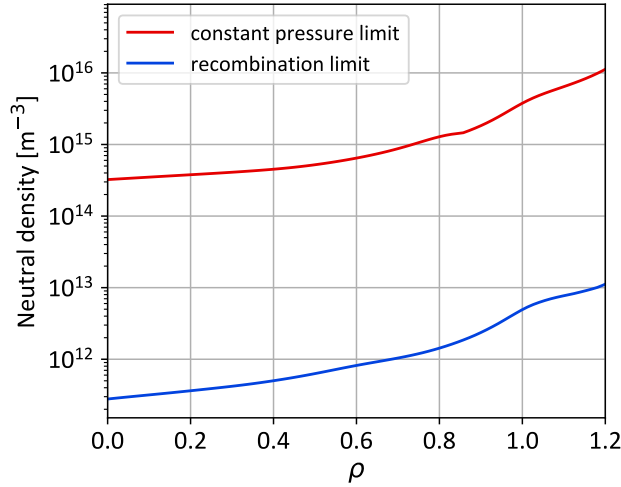


Figure 7.1: Upper and lower neutral density limits obtained from the constant pressure- (red) and recombination (blue) assumptions.

7.2 Estimation of fast-ion density

To assess the fast ion density in W7-X, the observed FIDA light can be compared to the sum of active and passive FIDASIM estimates which is proportional to the ASCOT predicted fast ion densities. The total amount of line-integrated FIDA light observed at a given wavelength can be expressed as follows:

$$I(\lambda) = \int_{LOS} n_{fi}(\mathbf{x})n_0(\mathbf{x})\epsilon(\mathbf{x}, \lambda)d\mathbf{x} \quad (7.4)$$

Here, n_{fi} is the fast ion density, n_0 is the donor neutral density and ϵ is the emissivity of the observed transition, which depends on the velocity vector of the emitting neutralized fast ion and on the observation direction. The donor neutral density n_0 consists of the well predicted and validated active contribution from the NBI operation, n_0^A , and the passive background neutral density, n_0^P .

$$n_0 = n_0^A + n_0^P \quad (7.5)$$

Taking the upper and lower boundaries of the background neutral density n_0^P , as derived in the previous section, it can be assumed that total experimental donor neutral density is bounded in between:

$$n_0^A + \min(n_0^P) \leq n_0 \leq n_0^A + \max(n_0^P) \quad (7.6)$$

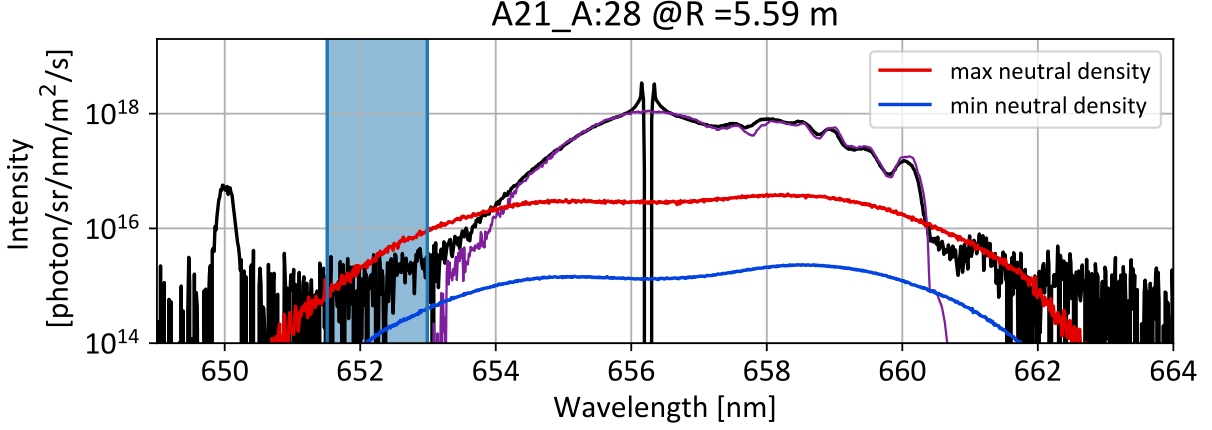


Figure 7.2: Example Balmer-alpha spectrum, with predicted total FIDA emissions with the lowest and highest neutral density values shown in blue and red. The fitted wavelength region to obtain the counter-propagating scaling factor is marked with blue transparent color.

Considering the upper and lower limits of n_0^P background neutral densities in FIDASIM, it is possible to predict the minimal and maximal levels of FIDA light expected from a given fast-ion distribution function (later denoted as I_{FS}^{min} and I_{FS}^{max} accordingly).

An example spectrum prediction with minimal and maximal passive contribution for an A21 port channel is shown in figure 7.2. For reference, the sum of the previously fitted halo and BES emission is shown in purple color. The FIDA emission prediction with the minimal neutral density is shown in blue while the case with the upper boundary is shown in red color. The lower boundary underestimates the measured FIDA radiation, while the upper boundary provides a slight overestimation.

Scaling factors α and β can be determined by fitting the observed intensity I with the FIDASIM predictions I_{FS} at a selected wavelength range:

$$\alpha I_{FS}^{min}(\lambda, n_{fi}^*, n_0^{min}) \approx I(\lambda, n_{fi}, n_0) \approx \beta I_{FS}^{max}(\lambda, n_{fi}^*, n_0^{max}) \quad (7.7)$$

The obtained scaling factors in principle scale the product of the assumed fast-ion density n_{fi}^* and donor neutral density ambiguously, but as they were obtained by utilizing the extreme neutral density cases (thus we already consider all of its possible variation), their value can be attributed exclusively to the fast-ion density itself. The simulation with the minimal neutral density provides an upper limit while the case considering the maximal neutral density provides a lower boundary for the measured n_{fi} fast-ion density compared

to the ASCOT4 prediction n_{fi}^* :

$$\beta n_{fi}^*(\mathbf{x}) \leq n_{fi}(\mathbf{x}) \leq \alpha n_{fi}^*(\mathbf{x}) \quad (7.8)$$

Figure 7.3 shows α and β fast-ion density scaling parameters as function of major radius (at the point of line of sight NBI intersection). The triangles correspond to the lower boundary (α) while the circles represent the upper neutral density boundary (β). The different colors mark different observation ports, similarly as before. Subplot a) shows the scaling factors obtained when analyzing the emission of fast ions propagating in the counter-injection direction (blue shifted radiation for the A21 port views, red shifted for T21 and M21) and subplot b) shows scaling factors for fast ions that move parallel to the NBI-injection direction (red shifted radiation for the A21 port views, blue shifted for T21 and M21). Also note that scaling factors that correspond to channels which are affected by strong prompt fast-ion passive radiation are indicated by open, transparent symbols in subplot b). In subplot a) different observation directions (different colors) show a similar

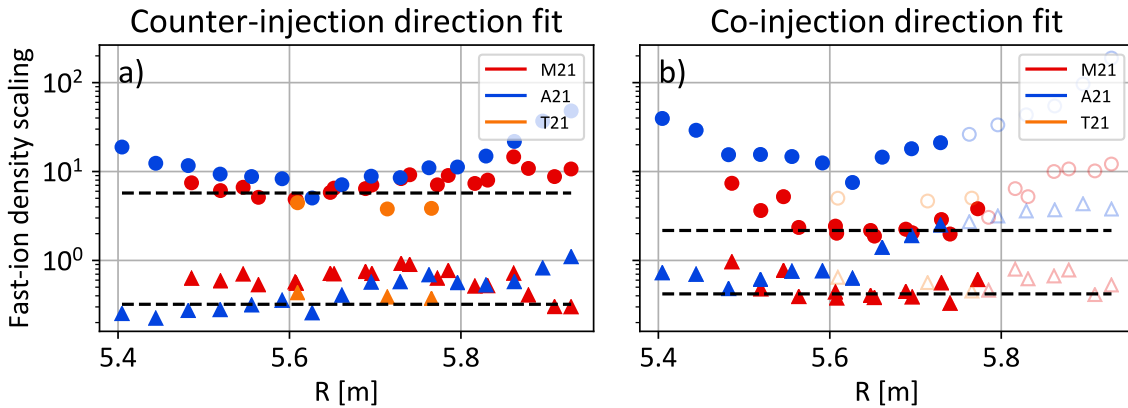


Figure 7.3: Fast-ion density scaling factors obtained by matching limiting cold neutral density simulations to the experimentally observed spectra. Different colors mark different observation ports' measurements.

trend with an increasing upper scaling factor towards the lowest and highest major radius values, a flat lower scaling factor profile while having its narrowest part in the plasma core at 5.6 m. In the case of subplot b), although the same trends can be observed and the scaling factors are in the same order of magnitude as in subplot a), but the upper limit shows a wider spread, suggesting larger uncertainties there. This can be explained, as the

co-injection direction side of the spectra is already occupied by the beam emission, thus only limited, highly Doppler-shifted wavelength regions with high noise levels are available for the fitting analysis, where the FIDA intensity is already strongly decayed.

To obtain a global lower- and upper scaling factor, limits for the observed fast-ion density, their corresponding values have been averaged, taking their variance as weights. It is shown in figure 7.3 with black dashed lines. This fit suggests the following boundaries of the fast-ion density in the counter- and co-injection direction respectively:

$$0.32 \cdot n_{fi}^*(\mathbf{x}) \leq n_{fi}(\mathbf{x}) \leq 5.73 \cdot n_{fi}^*(\mathbf{x})$$

$$0.42 \cdot n_{fi}^*(\mathbf{x}) \leq n_{fi}(\mathbf{x}) \leq 2.17 \cdot n_{fi}^*(\mathbf{x})$$

The similar fast-ion density scaling factors in the different directions suggests that there is no significant difference between co- and counter direction propagating particle confinement. Overall, the result shows that the fast-ion density in the investigated discharge is within the same order of magnitude as the neoclassical slowing down prediction by ASCOT4 and thus the fast-ion confinement in W7-X is not strongly influenced by anomalous transport at present.

Chapter 8

Summary and Outlook

Good fast-ion confinement is one of the fundamental requirements for the successful operation of future fusion power plants. In W7-X, a stellarator that aims to provide the experimental basis for the next-step fusion reactor design, investigation of fast-ion confinement is a core objective. Well-confined fast ions are generated at W7-X with two newly installed neutral beam injection (NBI) sources that inject 50-55 keV neutral hydrogen, that ionizes as it passes through the plasma. In order to diagnose fast ion confinement, this thesis work studies the Balmer-alpha emission of fast ions that undergo charge exchange reactions with donor neutrals, referred to as FIDA emission.

8.1 Summary

The Balmer-alpha light is collected by 3 spatially separated observation optics (located in the A21, M21, T21 ports) that are part of an existing charge-exchange recombination spectroscopy (CXRS) system at W7-X. The three optics define in total 51 lines of sight whose radiation is analyzed by a high throughput spectrometer which well covers the spectral range of the Balmer alpha emission. The spectra consist of the active beam- and halo emissions, FIDA emission, and other passive contributions. High quality FIDA signals were observed by performing measurements with a sCMOS camera, operated with an exposure time of 50 ms. This exposure time is possible in W7-X as fast magneto-hydrodynamic modes, such as sawtooth crashes or ELMs, are typically absent which otherwise rapidly change the fast-ion distribution in tokamaks. The measurements were intensity and wavelength calibrated, and careful data curation was necessary by binning the raw measurements, min-

imizing cross-talk between consecutive channels. The three separated observation optics provide complementary information on the fast-ion phase-space in the observed module. While wavelength ranges available for FIDA analysis of data from the core M21 and T21 port views provide information on fast ions with both positive and negative pitch angles, the A21 port views provide only well accessible FIDA radiation from fast ions with negative pitch angles.

To provide a link between the measured convoluted Balmer-alpha spectra and theoretical predictions of the fast-ion distribution function by ASCOT4, the spectra modeling tool FIDASIM was used. The code was adapted to the W7-X stellarator taking specifics of its 3D geometry into account. As a part of this process, a simplistic model of the beam duct has been considered, which shapes the source of active neutrals. The predicted active beam- and halo emissions were compared to the calibrated measurements and reasonable agreement within 30% was found throughout all the measured spectra. This demonstrates that FIDASIM code was adapted well to the 3D magnetic field geometry of W7-X, the neutral beam injection geometry, observation geometry and plasma parameters. In addition the good agreement shows that the intensity calibration, and its evaluation, has been carried out properly. When comparing the FIDASIM predictions of the active FIDA emission to measurements it was identified that the observed FIDA signals at W7-X contain a strong passive contribution. This passive emission originates from charge exchange reactions between fast ions and cold neutrals, is dependent on the observation geometry and often dominates the measured signal. Passive FIDA emissions were predicted in FIDASIM by implementing background neutral profiles but still showed a clear deviation from the observed spectral shape. In particular, the observation of flat emission shoulders at the blue-shifted wavelengths (651-653 nm) of the T-port views could not be reproduced. It was found that an edge particle population with a narrow pitch and energy distribution has to be added to the ASCOT provided fast-ion distribution in order to explain the observation. This prompt fast ion distribution was modelled by predicting the fast-ion birth profile in the edge region using FIDASIM and then applying 3D orbit following to them. Using the newly implemented prompt fast-ion distribution function in FIDASIM, excellent agreement between the predicted and observed emission shoulder was found on the T21 port lines of sight. In addition it became evident that several views from other ports are also affected by the passive prompt emission.

Understanding details of the prompt passive FIDA contribution enabled the assessment

of the fast-ion confinement in W7-X since viewing geometries and wavelength ranges could be selected that avoids this emission. It should be noted that these viewing geometries and wavelength ranges will still be subject to passive FIDA radiation based on the overlap of the background neutral density and the confined fast ion population. Finally, a range of fast-ion densities possible given the measured FIDA emission was determined. For this purpose, lower- and upper limits of the neutral density were estimated and used as inputs for FIDASIM simulations to predict limits of possible passive emissions. These are added to the well-modeled active FIDA light with a fast-ion density that is scaled to match the observed emission for each of the two limiting cases. It was found that the observed fast-ion density is within the same order of magnitude as ASCOT4 predictions, it is at least 0.4 times- and at most 5 times more than ASCOT4 predicted. Thus it was shown that the ASCOT4 predictions are consistent with the observed FIDA measurements, given what is known about the neutral density. The large range shows that the passive contribution and influence of the prompt fast-ions is critical in the interpretation of the FIDA measurements at W7-X and can not be neglected in future studies. Nevertheless, this work is the first demonstration that extraction of useful physics quantities from the W7-X FIDA data is possible and provides new methods sophisticated enough to do this. The results strongly motivate future systematic studies using the methods developed here.

8.2 Outlook

The work performed during this thesis project provides a basis for future fast-ion transport studies at W7-X. Experiments during the next experimental campaigns will benefit from the detailed understanding of FIDA spectra but also from additional experimental possibilities that will become available and are detailed in the following.

The installation of the second beam box (referred to as NI20) in the next operational campaign, consisting of two additional NBI sources, opens up the possibility to extract the active FIDA contribution via background subtraction. For this, NI20 will be used in continuous operation to generate fast ions, while NI21 will be operated with short beam blips for CXRS and FIDA measurements. This will allow accurate background subtraction by measuring in both the on and off NBI phases of NI21. The difference of the two signals will contain the active FIDA emission (with fast-ions from NI20) and the prompt passive emission from the modulated source (with fast-ion from NI21). However, by selecting

lines of sight that avoid the prompt emission, clear active spectra can be obtained. It makes direct comparison active FIDA predictions based on ASCOT4 distribution functions and measurements possible, offering insight into fast-ion confinement properties of the given experiment as the passive radiation will no longer need to be addressed with its uncertainties. We propose investigating the properties of fast-ion confinement of different magnetic configurations with operating the NBIs in each configuration with the similar kinetic profiles. This would produce similar birth profiles of fast-ions, but as the fast-ion slowing down process is different, it would induce different equilibrium fast-ion distribution. Consequently, changes in the FIDA emission could be expected due to changes of fast ion physics in the different magnetic configurations.

The absence of passive radiation is essential for the application of the method of velocity-space tomography [16]. This method requires a point-like measurement volume at the intersection between NBI and multiple lines of sight, from which the active FIDA light originates. The method uses weight functions, the sensitivity of a given line of sight to the fast-ion phase-space to observe FIDA light, in order to establish connection between local, energy and pitch dependent fast-ion distribution $f(E, \Lambda)$, and the observed FIDA light $I(\lambda)$:

$$I(\lambda) = \iint W_\lambda(E, \Lambda) \circ f(E, \Lambda) dE d\Lambda \quad (8.1)$$

By having multiple lines of sight with different weight function crossing the same volume, inference of local fast-ion distribution $f(E, \Lambda)$ is possible by inversion from the measured FIDA signals.

Generally, the high signal quality suggests that shorter integration times would be feasible (lower than the characteristic timescales for fast-ion slowing down), 5-10 ms, opening up possibilities for so called beam modulation experiments with NI20. Turning the source of fast-ions on-and-off repetitively would produce a measurable time dependence of the passive FIDA intensities. By choosing the on-phase duration long enough to build up an equilibrium fast-ion distribution, around 100 ms, the off-phase FIDA intensity change due to the depletion of fast-ions could be observed in the passive intensity.

Similarly to the modulation experiments, MHD events can redistribute the fast-ions and will be used to study their transport. In particular, driving strong localised currents with electron cyclotron current drive leads to periodic, sawtooth like crashes of kinetic plasma profiles. This is a phenomena investigated in detail in the case of tokamaks, showing

redistribution of fast-ions in the time scale of 100 ms [73, 74], but an unexplored topic in the case of stellarators. By probing the active FIDA emission through these crash cycles, modulation of the FIDA light could be observed and redistribution of the fast-ions can be inferred based on the affected wavelength regions.

Last but not least possibilities with the passive emission needs to be discussed. As the observed passive emission is the result of fast-ions and donor cold neutrals it could provide information on either of those, given that we could predict the other. In this thesis, the detailed analysis of the prompt particle population was investigated, and in the future it would be possible to predict absolute fast-ion densities too. Given its good spatial localisation, inference of the donor neutral density would be possible in the edge region by utilizing the knowledge on the prompt particle population. Alternatively, with more detailed modeling of the neutral population with EMC3-EIRINE, assessment of the properties of edge fast-ions would become possible.

Bibliography

- [1] H Ritchie. Fossil Fuels. *Our World in Data*, 2017. <https://ourworldindata.org/fossil-fuels>.
- [2] AS Eddington. *The internal constitution of the stars*. Cambridge University Press, 1988.
- [3] J Wesson and DJ Campbell. *Tokamaks*, volume 149. Oxford university press, 2011.
- [4] HS Bosch. Review of data and formulas for fusion cross-sections. Technical report, Max-Planck-Institut für Plasmaphysik, 1990.
- [5] FF Chen et al. *Introduction to Plasma Physics and Controlled Fusion*, volume 1. Springer, 1984.
- [6] JD Lawson. Some criteria for a power producing thermonuclear reactor. *Proceedings of the physical society. Section B*, 70(1):6, 1957.
- [7] RS Craxton, KS Anderson, TR Boehly, VN Goncharov, DR Harding, JP Knauer, RL McCrory, PW McKenty, DD Meyerhofer, JF Myatt, et al. Direct-drive inertial confinement fusion: A review. *Physics of Plasmas*, 22(11):110501, 2015.
- [8] MD Kruskal and RM Kulsrud. Equilibrium of a magnetically confined plasma in a toroid. *The Physics of Fluids*, 1(4):265–274, 1958.
- [9] T Klinger, T Andreeva, S Bozhenkov, C Brandt, R Burhenn, B Buttenschön, G Fuchert, B Geiger, O Grulke, HP Laqua, et al. Overview of first Wendelstein 7-X high-performance operation. *Nuclear Fusion*, 59(11):112004, 2019.
- [10] E Viezzer, T Pütterich, R Dux, RM McDermott, and ASDEX Upgrade Team. High-resolution charge exchange measurements at ASDEX Upgrade. *Review of scientific Instruments*, 83(10):103501, 2012.
- [11] RM Churchill, C Theiler, B Lipschultz, R Dux, T Pütterich, E Viezzer, Alcator C-Mod Team, and ASDEX Upgrade Team. Development of the gas puff charge exchange recombination spectroscopy (GP-CXRS) technique for ion measurements in the plasma edge. *Review of Scientific Instruments*, 49(9):104014, 2013.

- [12] RJ Fonck, DS Darrow, and KP Jaehnig. Determination of plasma-ion velocity distribution via charge-exchange recombination spectroscopy. *Physical Review A*, 29(6):3288, 1984.
- [13] JM Faustin, WA Cooper, JP Graves, David Pfefferlé, and Joachim Geiger. Fast particle loss channels in Wendelstein 7-X. *Nuclear Fusion*, 56(9):092006, 2016.
- [14] WW Heidbrink, D Liu, Y Luo, E Ruskov, and Benedikt Geiger. A code that simulates fast-ion $D\alpha$ and neutral particle measurements. *Communications in Computational Physics*, 10(3):716–741, 2011.
- [15] B Geiger, L Stagner, WW Heidbrink, R Dux, R Fischer, Y Fujiwara, AV Garcia, AS Jacobsen, A Jansen van Vuuren, AN Karpushov, et al. Progress in modelling fast-ion D-alpha spectra and neutral particle analyzer fluxes using FIDASIM. *Plasma Physics and Controlled Fusion*, 62(10):105008, 2020.
- [16] M Weiland, B Geiger, Asger Schou Jacobsen, M Reich, Mirko Salewski, T Odstrčil, et al. Enhancement of the FIDA diagnostic at ASDEX Upgrade for velocity space tomography. *Plasma Physics and Controlled Fusion*, 58(2):025012, 2016.
- [17] B Geiger, M Weiland, Asger Schou Jacobsen, D Rittich, R Dux, R Fischer, C Hopf, M Maraschek, RM McDermott, Stefan Kragh Nielsen, et al. Fast-ion transport and neutral beam current drive in ASDEX Upgrade. *Nuclear Fusion*, 55(8):083001, 2015.
- [18] CA Michael, N Conway, B Crowley, O Jones, WW Heidbrink, S Pinches, E Braeken, R Akers, C Challis, M Turnyanskiy, et al. Dual view FIDA measurements on MAST. *Plasma Physics and Controlled Fusion*, 55(9):095007, 2013.
- [19] CM Muscatello, WW Heidbrink, D Taussig, and KH Burrell. Extended fast-ion D-alpha diagnostic on DIII-D. *Review of Scientific Instruments*, 81(10):10D316, 2010.
- [20] B Geiger, AN Karpushov, BP Duval, C Marini, O Sauter, Y Andrebe, D Testa, M Maraschek, Mirko Salewski, PA Schneider, et al. Fast-ion transport in low density L-mode plasmas at TCV using FIDA spectroscopy and the TRANSP code. *Plasma Physics and Controlled Fusion*, 59(11):115002, 2017.
- [21] M Landreman and PJ Catto. Omnigenity as generalized quasisymmetry. *Physics of Plasmas*, 19(5):056103, 2012.
- [22] A Dinklage, T Klinger, G Marx, and L Schweikhard. *Plasma physics: confinement, transport and collective effects*, volume 670. Springer Science & Business Media, 2005.
- [23] WD D’haeseleer, WNG Hitchon, JD Callen, and JL Shohet. *Flux coordinates and magnetic field structure: a guide to a fundamental tool of plasma theory*. Springer Science & Business Media, 2012.

- [24] JR Cary and SG Shasharina. Omnigenity and quasihelicity in helical plasma confinement systems. *Physics of Plasmas*, 4(9):3323–3333, 1997.
- [25] RJ Goldston and PH Rutherford. *Introduction to Plasma Physics*. Institute of Physics Publishing, London, 1995.
- [26] J Nührenberg. Development of quasi-isodynamic stellarators. *Plasma Physics and Controlled Fusion*, 52(12):124003, 2010.
- [27] VD Shafranov. Equilibrium of a toroidal pinch in a magnetic field. *Soviet Atomic Energy*, 13(6):1149–1158, 1963.
- [28] T Kobuchi, K Ida, H Yamada, M Yokoyama, KY Watanabe, S Sakakibara, M Yoshinuma, LHD Experimental Group, et al. Magnetic configuration dependence of the Shafranov shift in the Large Helical Device. *Plasma physics and controlled fusion*, 48(6):789, 2006.
- [29] M Drevlak, J Geiger, P Helander, and Yu Turkin. Fast particle confinement with optimized coil currents in the W7-X stellarator. *Nuclear Fusion*, 54(7):073002, 2014.
- [30] P Helander and DJ Sigmar. *Collisional transport in magnetized plasmas*, volume 4. Cambridge university press, 2005.
- [31] RJ Goldston, DC McCune, HH Towner, SL Davis, RJ Hawryluk, and GL Schmidt. New techniques for calculating heat and particle source rates due to neutral beam injection in axisymmetric tokamaks. *Journal of computational physics*, 43(1):61–78, 1981.
- [32] TH Stix. Heating of toroidal plasmas by neutral injection. *Plasma Physics*, 14(4):367, 1972.
- [33] W Ott, E Speth, and A Stäbler. Slowing-down of fast ions in a plasma: Energy transfer, charge exchange losses and wall sputtering. 1977.
- [34] RJ Hawryluk. An empirical approach to tokamak transport. In *Physics of plasmas close to thermonuclear conditions*, pages 19–46. Elsevier, 1981.
- [35] D Pfefferlé, WA Cooper, JP Graves, and C Misev. VENUS-LEVIS and its spline-fourier interpolation of 3D toroidal magnetic field representation for guiding-centre and full-orbit simulations of charged energetic particles. *Computer Physics Communications*, 185(12):3127–3140, 2014.
- [36] M Weiland, R Bilato, R Dux, B Geiger, A Lebschy, F Felici, R Fischer, D Rittich, M Van Zeeland, Eurofusion MST1 Team, et al. RABBIT: Real-time simulation of the NBI fast-ion distribution. *Nuclear Fusion*, 58(8):082032, 2018.

- [37] E Hirvijoki, O Asunta, T Koskela, T Kurki-Suonio, J Miettunen, S Sipilä, A Snicker, and S Äkäslompolo. ASCOT: Solving the kinetic equation of minority particle species in tokamak plasmas. *Computer Physics Communications*, 185(4):1310–1321, 2014.
- [38] O Asunta, J Govenius, R Budny, M Gorelenkova, G Tardini, T Kurki-Suonio, A Salmi, S Sipilä, et al. Modelling neutral beams in fusion devices: Beamlet-based model for fast particle simulations. *Computer Physics Communications*, 188:33–46, 2015.
- [39] B Bombard. KN1D: A 1-D space, 2-D velocity, kinetic transport algorithm for atomic and molecular hydrogen in an ionizing plasma. 2001.
- [40] VR Winters, F Reimold, R König, M Krychowiak, T Romba, C Biedermann, S Bozhenkov, P Drewelow, M Endler, Y Feng, et al. EMC3-EIRENE simulation of first wall recycling fluxes in W7-X with relation to h-alpha measurements. *Plasma Physics and Controlled Fusion*, 63(4):045016, 2021.
- [41] J Nührenberg and R Zille. Stable stellarators with medium β and aspect ratio. *Physics Letters A*, 114(3):129–132, 1986.
- [42] C Beidler, G Grieger, F Herrnegger, E Harmeyer, J Kisslinger, W Lotz, H Maassberg, P Merkel, J Nührenberg, F Rau, et al. Physics and engineering design for Wendelstein VII-X. *Fusion Technology*, 17(1):148–168, 1990.
- [43] T Klinger, C Baylard, CD Beidler, J Boscary, HS Bosch, A Dinklage, D Hartmann, P Helander, H Maßberg, A Peacock, et al. Towards assembly completion and preparation of experimental campaigns of Wendelstein 7-X in the perspective of a path to a stellarator fusion power plant. *Fusion Engineering and Design*, 88(6-8):461–465, 2013.
- [44] SP Hirshman and JC Whitson. Steepest-descent moment method for three-dimensional magnetohydrodynamic equilibria. *The Physics of fluids*, 26(12):3553–3568, 1983.
- [45] RL Dewar and SR Hudson. Stellarator symmetry. *Physica D: Nonlinear Phenomena*, 112(1-2):275–280, 1998.
- [46] C Nührenberg, AH Boozer, and SR Hudson. Magnetic-surface quality in nonaxisymmetric plasma equilibria. *Physical review letters*, 102(23):235001, 2009.
- [47] TS Pedersen, R König, M Krychowiak, M Jakubowski, J Baldzuhn, S Bozhenkov, G Fuchert, A Langenberg, H Niemann, D Zhang, et al. First results from divertor operation in Wendelstein 7-X. *Plasma Physics and Controlled Fusion*, 61(1):014035, 2018.
- [48] RC Wolf, S Bozhenkov, A Dinklage, G Fuchert, YO Kazakov, HP Laqua, S Marsen, NB Marushchenko, T Stange, M Zanini, et al. Electron-cyclotron-resonance heating in Wendelstein 7-X: A versatile heating and current-drive method and a tool for in-depth physics studies. *Plasma Physics and Controlled Fusion*, 61(1):014037, 2018.

- [49] HP Laqua, J Baldzuhn, H Braune, S Bozhenkov, K Brunner, M Hirsch, U Hoefel, J Knauer, A Langenberg, S Marsen, et al. High-performance ECRH at W7-X: experience and perspectives. *Nuclear Fusion*, 61(10):106005, 2021.
- [50] N Rust, B Heinemann, B Mendelevitch, A Peacock, and M Smirnow. W7-X neutral-beam-injection: Selection of the NBI source positions for experiment start-up. *Fusion Engineering and Design*, 86(6-8):728–731, 2011.
- [51] P McNeely, M Barlak, J Baldzuhn, S Bozhenkov, M Drevlak, G Gawlik, B Heinemann, D Holtum, J Jagielski, R Kairys, et al. Current status of the neutral beam heating system of W7-X. *Fusion Engineering and Design*, 88(6-8):1034–1037, 2013.
- [52] A Spanier, D Hartmann, S Äkäslompolo, O Ford, N den Harder, B Heinemann, C Hopf, R Kairys, P McNeely, PZs Poloskei, et al. Performance of the first neutral beam injector at the Wendelstein 7-X stellarator. *Fusion Engineering and Design*, 163:112115, 2021.
- [53] E Pasch, MNA Beurskens, Sergey A Bozhenkov, G Fuchert, J Knauer, Robert C Wolf, and W7-X Team. The Thomson scattering system at Wendelstein 7-X. *Review of Scientific Instruments*, 87(11):11E729, 2016.
- [54] S A Bozhenkov, M Beurskens, A Dal Molin, G Fuchert, E Pasch, MR Stoneking, M Hirsch, U Höfel, J Knauer, J Svensson, et al. The Thomson scattering diagnostic at Wendelstein 7-X and its performance in the first operation phase. *Journal of Instrumentation*, 12(10):P10004, 2017.
- [55] KJ Brunner, T Akiyama, M Hirsch, J Knauer, P Kornejew, B Kursinski, H Laqua, J Meineke, H Trimino Mora, and RC Wolf. Real-time dispersion interferometry for density feedback in fusion devices. *Journal of Instrumentation*, 13(09):P09002, 2018.
- [56] H Weisen, M Von Hellermann, A Boileau, LD Horton, W Mandl, and HP Summers. Charge exchange spectroscopy measurements of ion temperature and toroidal rotation in JET. *Nuclear fusion*, 29(12):2187, 1989.
- [57] OP Ford, L Vanó, JA Alonso, J Baldzuhn, MNA Beurskens, C Biedermann, SA Bozhenkov, G Fuchert, B Geiger, D Hartmann, et al. Charge exchange recombination spectroscopy at Wendelstein 7-X. *Review of Scientific Instruments*, 91(2):023507, 2020.
- [58] RJE Jaspers, M Scheffer, A Kappatou, NCJ van der Valk, M Durkut, Bart Snijders, O Marchuk, Wolfgang Biel, GI Pokol, G Erdei, et al. A high etendue spectrometer suitable for core charge exchange recombination spectroscopy on ITER. *Review of scientific instruments*, 83(10):10D515, 2012.
- [59] A Kappatou. Investigations of helium transport in ASDEX upgrade plasmas with charge exchange recombination spectroscopy. 2015.

- [60] A Kappatou, RM McDermott, T Pütterich, R Dux, B Geiger, RJE Jaspers, AJH Donné, Eleonora Viezzer, M Cavedon, et al. A forward model for the helium plume effect and the interpretation of helium charge exchange measurements at ASDEX Upgrade. *Plasma Physics and Controlled Fusion*, 60(5):055006, 2018.
- [61] A Kappatou, E Delabie, RJE Jaspers, and MG Von Hellermann. Feasibility of non-thermal helium measurements with charge exchange spectroscopy on ITER. *Nuclear Fusion*, 52(4):043007, 2012.
- [62] A Alonso, O Ford, L Vano, S Äkäslompolo, D Carralero, I Calvo, A Dinklage, T Estrada, A Langenberg, S Lazerson, et al. Net parallel carbon rotation in the core of the Wendelstein 7-X stellarator: A deviation from neoclassical predictions? In *28th IAEA Fusion Energy Conference (FEC 2020)*, 2020.
- [63] MNA Beurskens, SA Bozhenkov, O Ford, P Xanthopoulos, A Zocco, Y Turkin, A Alonso, C Beidler, I Calvo, D Carralero, et al. Ion temperature clamping in Wendelstein 7-X electron cyclotron heated plasmas. *Nuclear Fusion*, 61(11):116072, 2021.
- [64] RK Janev, WD Langer, E Douglass Jr, et al. Elementary processes in hydrogen-helium plasmas: cross sections and reaction rate coefficients. 2012.
- [65] E Schrödinger. Quantisierung als eigenwertproblem. *Annalen der physik*, 385(13):437–490, 1926.
- [66] M Salewski, B Geiger, SK Nielsen, H Bindslev, M García-Muñoz, WW Heidbrink, SB Korsholm, F Leipold, J Madsen, F Meo, et al. Combination of fast-ion diagnostics in velocity-space tomographies. *Nuclear Fusion*, 53(6):063019, 2013.
- [67] M Salewski, B Geiger, AS Jacobsen, M García-Muñoz, WW Heidbrink, SB Korsholm, F Leipold, J Madsen, D Moseev, SK Nielsen, et al. Measurement of a 2D fast-ion velocity distribution function by tomographic inversion of fast-ion D-alpha spectra. *Nuclear fusion*, 54(2):023005, 2014.
- [68] K Fujii, M Goto, S Morita, LHD Experiment Group, et al. Study of neutral hydrogen transport in LHD core plasmas based on high dynamic-range Balmer- α spectroscopy. *Nuclear Fusion*, 55(6):063029, 2015.
- [69] H Qin, S Zhang, J Xiao, J Liu, Y Sun, and WM Tang. Why is Boris algorithm so good? *Physics of Plasmas*, 20(8):084503, 2013.
- [70] P Sinha, H Hölbe, TS Pedersen, S Bozhenkov, et al. Numerical studies of scrape-off layer connection length in Wendelstein 7-X. *Nuclear Fusion*, 58(1):016027, 2017.
- [71] HP Summers. The ADAS user manual, version 2.6. <http://www.adas.ac.uk/>, 2004.

-
- [72] U Wenzel, G Schlisio, M Mulsow, TS Pedersen, M Singer, M Marquardt, D Pilopp, and N Rüter. Performance of new crystal cathode pressure gauges for long-pulse operation in the Wendelstein 7-X stellarator. *Review of Scientific Instruments*, 90(12):123507, 2019.
- [73] B Geiger, M Garcia-Munoz, R Dux, F Ryter, G Tardini, L Barrera Orte, IGJ Classen, E Fable, R Fischer, V Igochine, et al. Fast-ion transport in the presence of magnetic reconnection induced by sawtooth oscillations in ASDEX Upgrade. *Nuclear Fusion*, 54(2):022005, 2014.
- [74] SK Nielsen, H Bindslev, M Salewski, A Bürger, E Delabie, V Furtula, M Kantor, SB Korsholm, F Leipold, F Meo, et al. Fast-ion redistribution due to sawtooth crash in the TEXTOR tokamak measured by collective Thomson scattering. *Plasma Physics and Controlled Fusion*, 52(9):092001, 2010.

Acknowledgement

”We will go to Greifswald just for the 6 months of the campaign” they said. Then after some contemplation on actual complicated events back then, I decided to stay here for another 3 years completing my PhD. I have had no regrets ever since.

I would like to thank those without whom this work would not have been possible. I would like to thank professor Hartmut Zohm and professor Thomas Klinger for offering me a PhD position at IPP. In addition, I would like to thank Benedikt Geiger for his supervision and more, spending his mornings on Zoom calls with answering my questions, explaining all the whereabouts of fast-ions and spectroscopy. Special thanks to Oliver Ford for adopting me as his step-PhD-student at Wendelstein 7-X, that he was almost always happy to explain about the CXRS system, general optics or whatever silly questions I might have had. I’m grateful that he learnt that even if my family name starts with /Polos/ I’m not Polish. I hope that I could teach him a bit about fast-ions and his diagnostic system too. I’m thankful for him as he encouraged me whenever I felt self-doubt whether I’m any good fit here. I would like to thank Simppa Äkäslompolo, who helped me with the ASCOT4 code, providing details of his fast-ion simulations.

Furthermore, I would like to express my gratitude to my rather friends than just colleagues, who helped me endure long days of work with having a cupcake together, or just a nice espresso ever once in a while, thank you Klára and Anton from my Garching days, Vale, Beto, JP, Andrea and all the lunch group from Greifswald. In addition, I would like to thank my dear friends from back home as well, who always gave me a good time whenever we had the opportunity to see each other somewhere in the pandemic restricted subspace of the space-time continuum, thank you.

I will be ever in debt for the support and understanding of my family, who endured my absence in recent years. Finally, I’m even more grateful for You, Gabi who kept encouraging me on difficult days and for being the most reliable partner I could have ever asked for.